National Aeronautics and
Space Administration

George C. Marshall Space Flight Center
Marshall Space Flight Center, Alabama 35812

PD-B-77-141

RANGE SAFETY SIGNAL PROPAGATION THROUGH THE SRM EXHAUST PLUME OF THE SPACE SHUTTLE

by

Frederick P. Boynton
Alan R. Davies
P.S. Rajasekhar
J. Alex Thomson

Physical Dynamics, Inc.
P.O. Box 1069
Berkeley, California 94701

Final Report on
NASA Contract NAS8-32120

May 1977

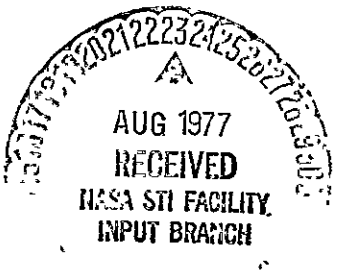

ACKNOWLEDGMENTS

We wish to thank several people for useful and stimulating discussions: Era N. Mann, Lee Malone, Ray Lowrey, H.G. Burke, Terry Greenwood, and R.M. Huffaker,* NASA/MSFC; Frank Mann, USAFETR; A.C. Victor, Naval Weapons Center; Horst A. Poehler** and Robert Pickett, Federal Electric Co.; Harold S. Pergament,** Aeronautical Research Association of Princeton; L. Douglas Smoot,** Brigham Young University; Ralph H. Kummler, Wayne State University and Physical Dynamics, Inc.; and Alan Ratliff, Morris Penney, Shelby Kurzius, and S.D. Smith, Lockheed Missiles and Space Company.

*Currently at NOAA, Wave Propagation Laboratory, Boulder, Colorado 80302.

**Consultant to Physical Dynamics, Inc.

ABSTRACT

This report is concerned with theoretical predictions of plume interference (signal attenuation) for the Space Shuttle Range Safety system by the Solid Rocket Booster (SRB) exhaust plumes. The signal propagation is calculated using a split operator technique based upon the Fresnel-Kirchoff integral, using fast Fourier transforms (FFT's) to evaluate the convolution and treating the plume as a series of absorbing and phase-changing screens. Talanov's lens transformation is applied to reduce aliasing problems caused by ray divergence.

Single-plume flow fields supplied by Lockheed Missile and Space Company were used as inputs. Three-dimensional effects at low altitudes were simulated by superposing the electron density and collision frequency of two independent plumes; at higher altitude the plumes are treated as merged plumes from an equivalent nozzle. Simulated plume turublence was included by constructing realizations of the displacement field in which possible correlations with axial distance were taken into account.

Comparisons of calculations of the mean flow plume-induced loss with field data from Project See-Thru show that the predicted signal loss for Titan III-C agrees fairly well with observations. The effects of simulated turbulence upon the

mean attenuation are small. Calculations for the Space Shuttle SRB plume predict attenuation levels exceeding 60 db at tail aspect at altitudes above about 20 km. The attenuation pattern becomes broader and deeper at higher altitudes, with maximum signal loss at the highest altitude.

TABLE OF CONTENTS

1.0 INTRODUCTION

In its capacity as the operating agency for the Eastern Test Range (ETR), the United States Air Force requires that launch vehicles and missiles fired from Cape Canaveral be equipped with a Range Safety System. This system should be capable of destroying the vehicle in flight on command from the ground when, in the judgment of the Range Safety Officer, life or property adjacent to the test range is threatened by malfunction or course deviations by the test vehicle. The Space Shuttle, whose first launch is scheduled for 1979, will carry a Range Safety system, and the George C. Marshall Space Flight Center, NASA, has been charged with the design and qualification of the system.

The SRM's burn a high-performance aluminized composite propellant. Previous experience with other large vehicles of this type (Minuteman, Polaris/Poseidon, Titan III) indicates that substantial signal loss and plume-induced noise are experienced when the line-of-sight signal passes through the exhaust plume. The Shuttle SRM's are the largest solid-fuel motors ever to be carried by a U.S. launch vehicle, and the exhaust gas is expected to be highly ionized in relation to most liquid-propellant plumes. A potentially serious signal transmission problem could be present when the plume intercepts the signal path.

The study reported here was undertaken to predict plume effects on the Range Safety signal. The last time that a similar problem was addressed for large rockets was about ten years ago when the Saturn and Titan III were under development.* In the meantime, computational procedures both for exhaust plume flow fields and chemistry and for forward electromagnetic wave propagation in lossy media have undergone considerable advances. These new procedures have been applied to our predictions. This study can therefore be considered both as an engineering study of an operational problem and as an advance in the state of the art of plume signal interference analysis.

*Development and analysis has continued for tactical missile systems, much of it at the Naval Weapons Center.

2.0 THE SPACE SHUTTLE RANGE SAFETY SYSTEM*

The Space Shuttle Range Safety System is similar in concept and operation to that previously employed on the Saturn V in the Apollo program. The command signal is a frequency modulated, frequency-shift keyed (FM-FSK) signal with a nominal central frequency of 416.5 MHz. The signal consists of a series of 11 tone pairs. The first 9 tone pairs alert the system, and the last 2 carry the signal itself. The tone pattern is shown schematically in Figure 1. The frequencies used range from 7.35 KHz to 13.65 KHz at intervals of 1.05 KHz. These frequencies are well outside the bandwidth of previously determined plume noise, so that plume noise should not have a significant effect on the signal.**

Mounting of the Range Safety antenna is shown in Figure 2. Each SRM carries two antennas mounted 180° apart and as far forward as possible (about 40 meters forward of the engine exit plane). Two additional antennas are mounted

*Most of the information in this section was furnished by Lee Malone, NASA/MSFC.

**Plume noise can have an effect on the S-band communications link over which some of the information required to make a range safety decision is transmitted. We have not addressed this problem in any depth in this study, although similar procedures should be applicable. H.A. Poehler has pointed out that flame noise can broaden the Range Safety Signal spectrum, possibly to the point where the spectrum could overlap with the result of erroneous detection.

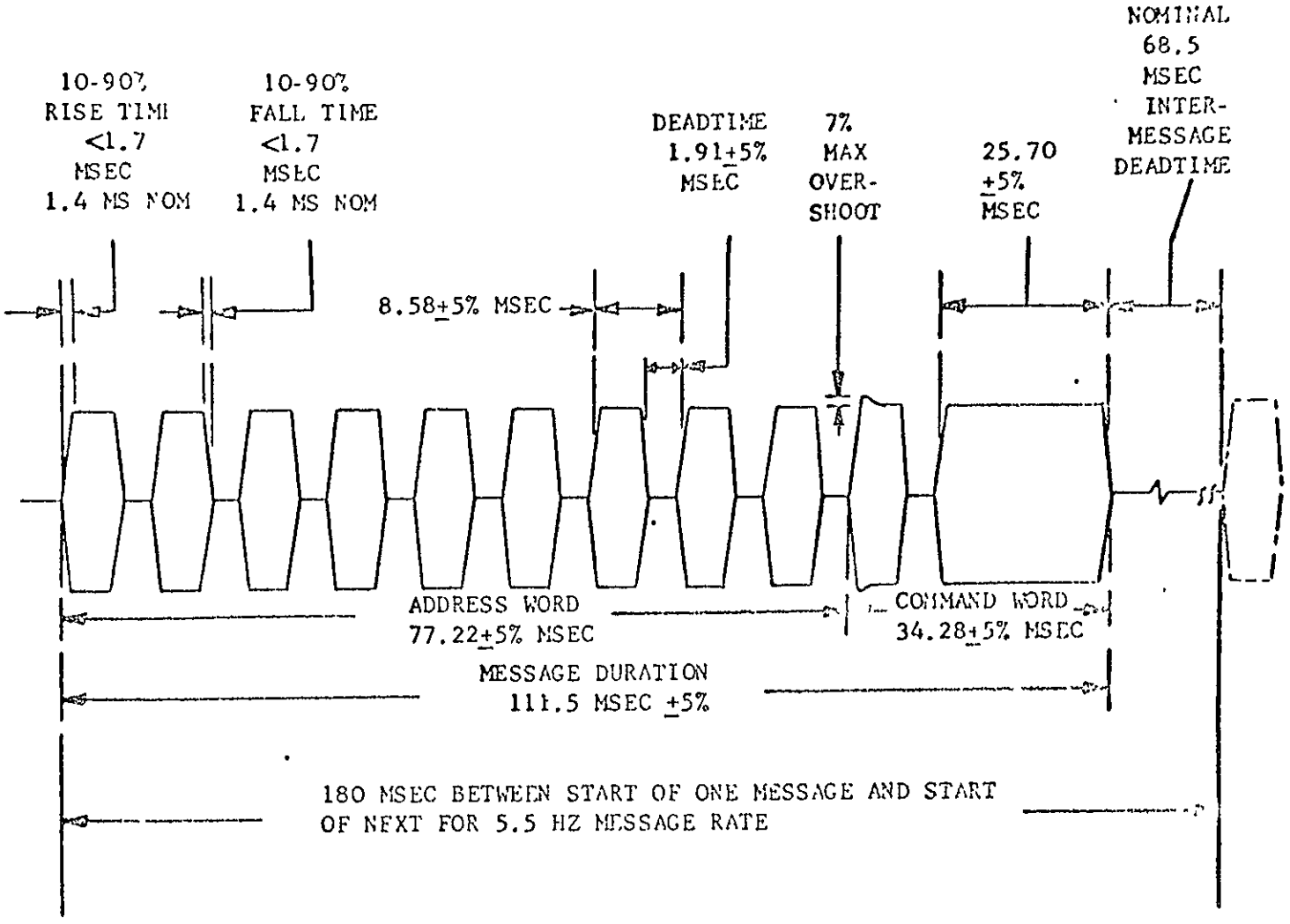

Figure 1. Space Shuttle Range Safety Signal Modulation Envelope

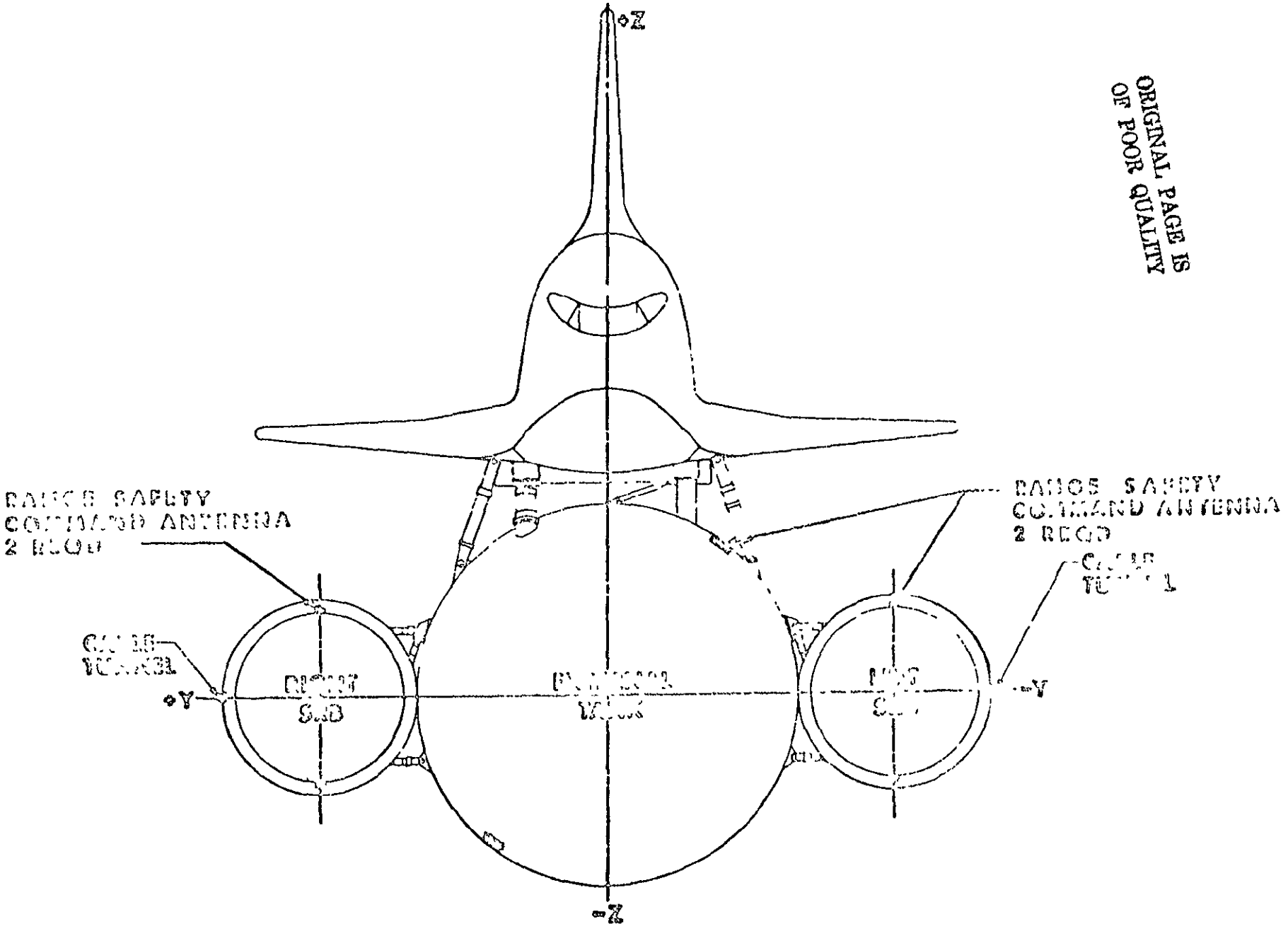

Figure 2. Space Shuttle launch configuation (forward aspect) showing location of range safety command antennas.

on the external tank, also well forward. Coupling with vehicle skin currents is not known, but is probably fairly strong for this complicated configuration. The near field antenna pattern has not been measured, although far field patterns are known. In this work we have assumed the antenna pattern to be isotropic.

3.0 PLUME-SIGNAL INTERFERENCE PHENOMENOLOGY

In this section we address the signal interference problem from two different points of view. We first adopt an empirical approach in which we review selected portions of the available data base, looking for trends (or lack of trends) with altitude and signal frequency. We then switch to an analytic approach, considering factors affecting RF propagation in a non-uniform, lossy dielectric medium, the relation of plume properties to propellant properties and operating conditions, and determine those effects which are theoretically expected to determine the observed signal levels. These considerations determine the computational approach adopted in the following section.

3.1 The Empirical Data Base

Because of the importance of plume interference to communications and telemetry, considerable attention has been given to it and a substantial body of data exists. Data for large vehicles are available from both Eastern and Western test ranges (ETR and WTR). Victor (1975) has summarized the results of many model tests and small vehicle flight tests. Poehler (1969 a, b, c) has summarized the best available ETR measurements, covering studies performed over the period 1963-1967. Because many of the older data contain unknown signal loss contributions from antenna

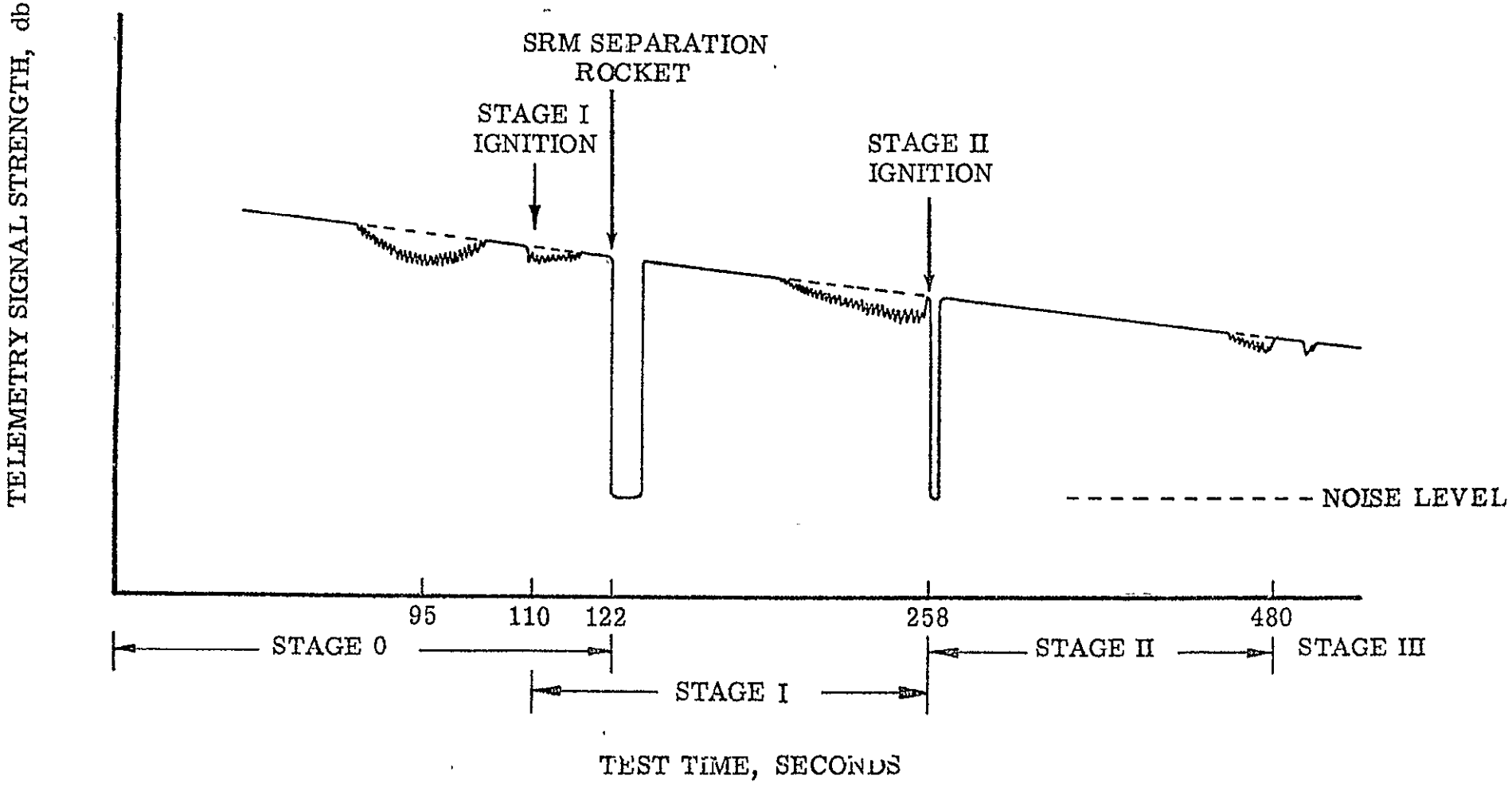

Figure 3. Composite representation of variations of P-band signal strength for Titan III-C launch in Project See-Thru.

pattern "holes" and pointing errors, they are generally less reliable than the later data.

The most complete body of data for a single vehicle is that associated with Project See-Thru (Poehler, 1966, 1967, 1968), a study of plume-signal interference effects associated with Titan III-C launches. These data cover several aspect angles with respect to the vehicle roll axis as well as several signal frequencies. In addition, the morphology of the Titan III-C 0^{th} stage plume is somewhat similar to that of the Space Shuttle SRM plumes, since in each case the two solid motors are parallel-staged with the upper stage. The effects found in these measurements are representative of those shown by plumes from other large solid-fueled vehicles, and the quoted attenuation levels are probably more quantitative.

Figure 3 is a composite representation (Poehler, 1966) of the sequence of events observed at P-band (250 MHz), in which observations from several fixed ground locations have been combined. (Few of the actual data plots are of this quality, and none will show all the effects shown in this composite.) No signal effects attributable to plume interference are observed during 0^{th} stage burn until about 75-90 seconds after liftoff. The aspect angle is high during this period, so that the line of sight does not intersect

the plume. At different times for each ground site, the line of sight intersects the plume and the signal becomes noisy and attenuated. Plume noise and plume attenuation are coupled; a noise-free signal loss is due to antenna pattern, pointing errors, or other phenomena. The aspect angle at a given ground site may either increase or decrease during the period from 80-110 seconds. The attenuation level typically increases with decreasing aspect, suggesting that the longer the signal path through the plume, the more greatly it is attenuated. First stage ignition (110 seconds) causes increased attenuation and SRM separation (122 seconds) produces a drastic drop in signal level. Additional periods of attenuation are observed during 1st and 2nd stage burn and at 2nd stage ignition.

Data were obtained at S-band (2.22 GHz), C-band (5 GHz) and X-band (9.1 GHz), as well as at P-band (250 MHz). Because the polarization characteristics of the X-band antenna were not determined, the X-band data are reported as "signal loss" rather than as "plume attenuation". When one attempts to interpret these data in terms of dependencies on various parameters (aspect, altitude, signal frequency) several complicating factors arise. Because measurements were taken at fixed ground locations, variation in signal characteristics at any given site contain the combined effects of aspect angle and altitude. Only by comparing

results from different sites is it possible (in principle) to infer aspect angle dependence at a given altitude. In addition, measurement problems at times intrude: for example, some stations show unexplained decreases in signal levels below the predicted free-space curve, and rapid fluctuations of up to 20 db in signal level occur during periods of plume interference. For these reasons Poehler has reported many of his data in the form of upper or lower bounds to the actual signal level.

Summaries of the attenuation measurements from Project See-Thru are given in Tables 3-1 and 3-2. The results in Table 3-1 are Poehler's summary of data from ETR Test 8275/2250; Table 3-2 is our interpretation of the P-band data from Tests 3656/6025 and 6020/6546, and could be in error by more than 5 db.

These data have been examined for trends in altitude and signal frequency. In Figures 4 and 5 the data obtained near 80 seconds and 110 seconds after liftoff (altitudes near 20 and 36 km, respectively) are plotted as attenuation versus aspect angle. All frequencies are shown. While at each altitude a trend with aspect angle is evident, there is no clear separation of data in terms of signal frequency (except at X-band, where the calibration contains an unknown correction for antenna polarization losses).

Table 3-1

X-Band Signal Loss**, Zero Stage

Aspect Angles*		Signal Loss	Test Time	Site
$\alpha = 180 - \theta$	ϕ			
> 16	70-150	0 db	0-110 sec	UC-2
16	339	> 10	+ 65	19.1
10-8	245-223	< 30	95-110	UC-11
9	186	30	108-110	19.1
4-5	199-188	40	100-110	UC-13

TABLE VI

C-Band Attenuation, Zero Stage

		Attenuation	Test Time	Site
> 15°	50-150	0 db	0-110 sec	CIF
11	346	> 10	+ 74	UC-13
6	188	> 20	+110	UC-13

TABLE VII

S-Band Attenuation, Zero Stage

> 25°	100-137	0 db	0-110 sec	STS
> 16	70-150	0	0-110	UC-2
> 15	50-150	0	0-110	CIF
15	306	> 8	+ 75	UC-11
10	346	> 12	+ 74	UC-13
8	223	> 10	+110	UC-11
5	188	> 20	+110	UC-13

TABLE VIII

P-Band Flame Attenuation, Zero Stage

> 15°	329-306	0 db	0- 75 sec	UC-11 (and UC-13)
8	223	15	+110	UC-11
5	191	15	+105	UC-13
2	281	20	+ 90	UC-13

Table 3-2

P-Band Telemetry Data, Titan III-C, AFETR

Vehicle	Time	Atten.	Aspect	Site
3656/6025	0-110	none	>18°	Tel 2
	105	10	15°	UC-12
	80	18	4°	UC-18
	95	~10	9°	UC-18
	110	15	11.5°	UC-18
6020/6546	110	~5	14°	Tel 2
	80	~5	13°	UC-7
	95	~10	13°	UC-7
	110	>18	11.5°	UC-7
	80	<16	7°	UC-18
	95	<18	8°	UC-18
	110	<22	8°	UC-18

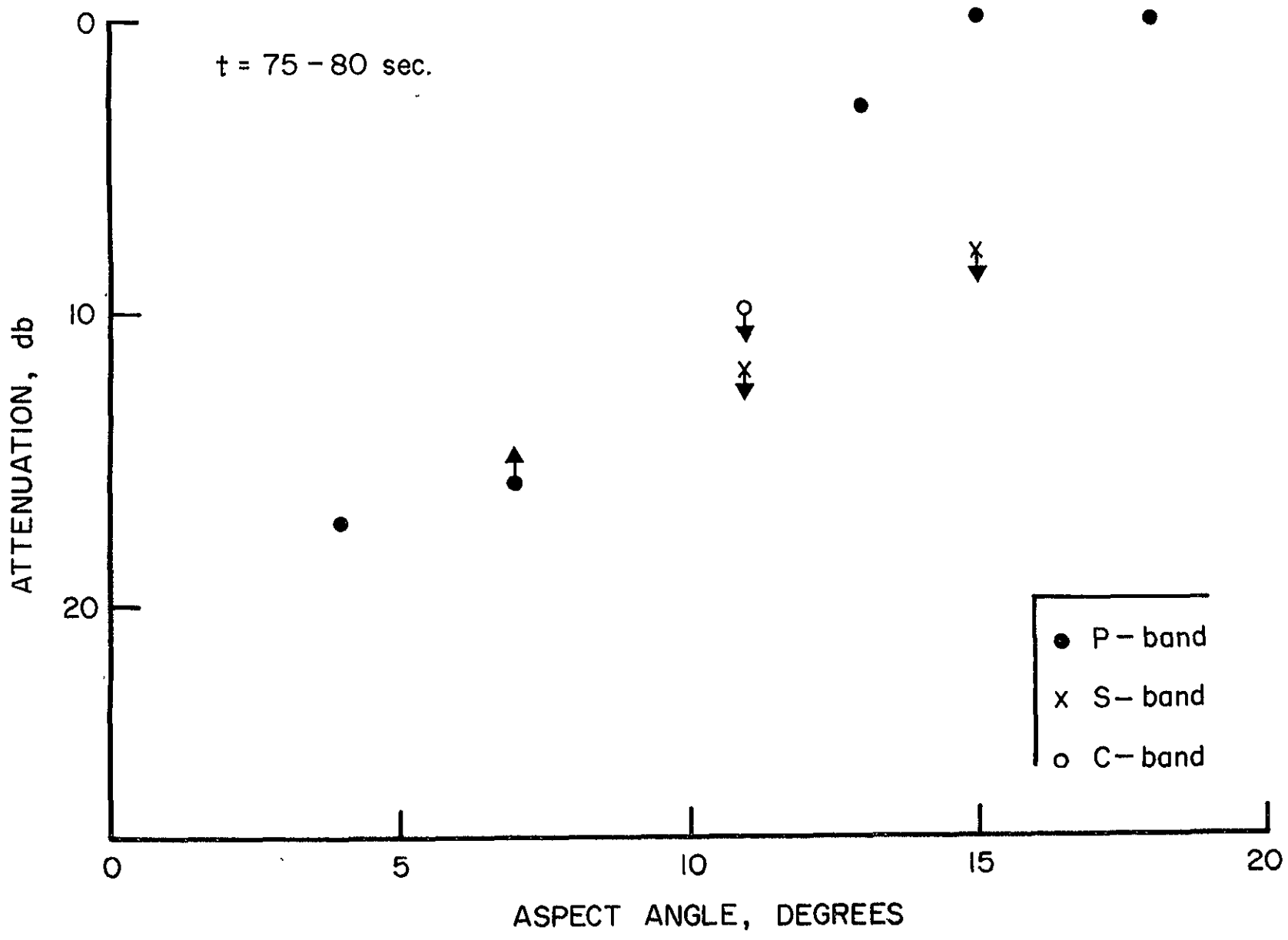

Figure 4. Attenuation levels as a function of polar aspect angle for Titan III-C near 80 sec. TALO

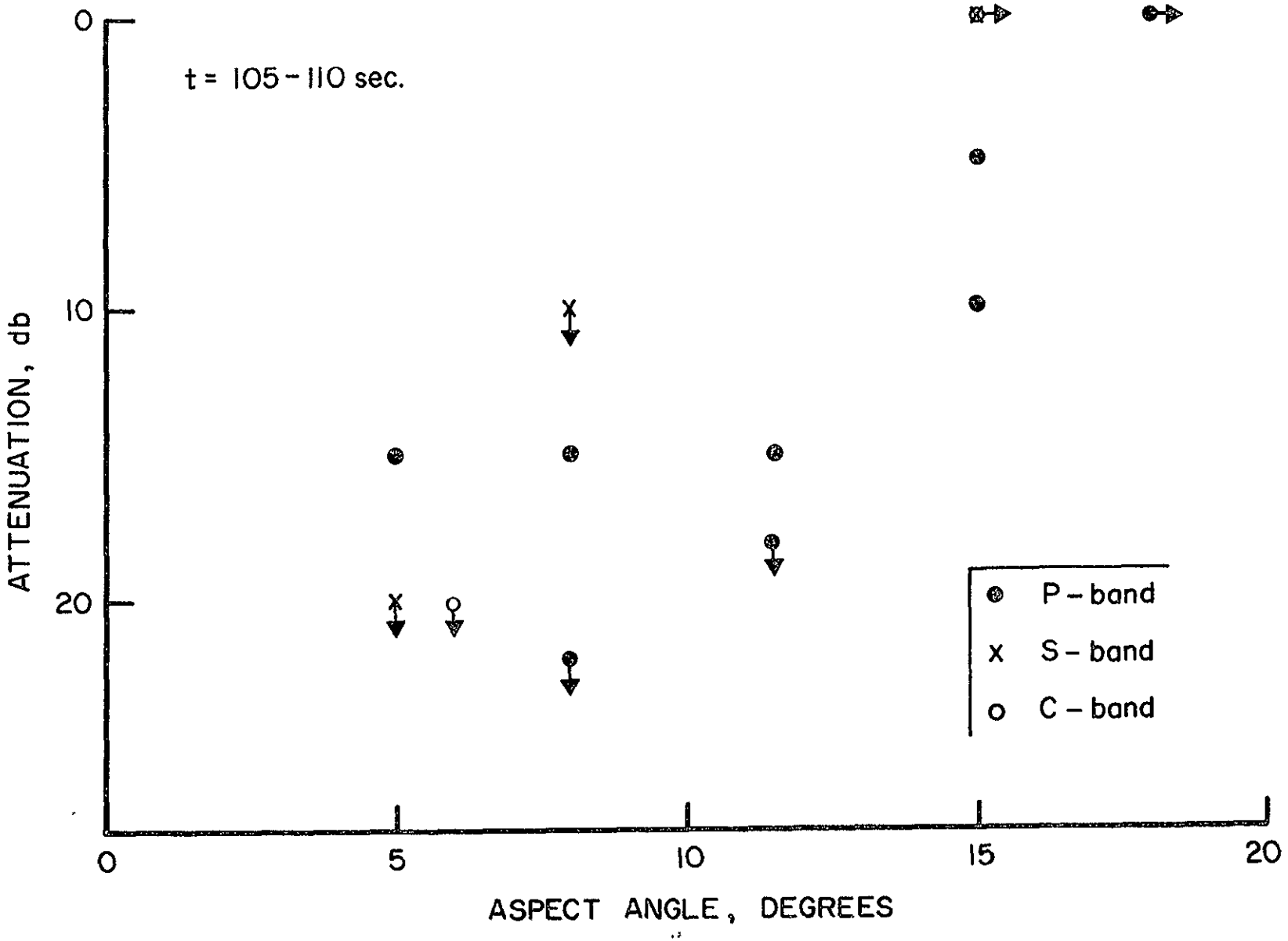

Figure 5. Attenuation levels as a function of aspect angle for Titan III-C near 110 sec. TALO.

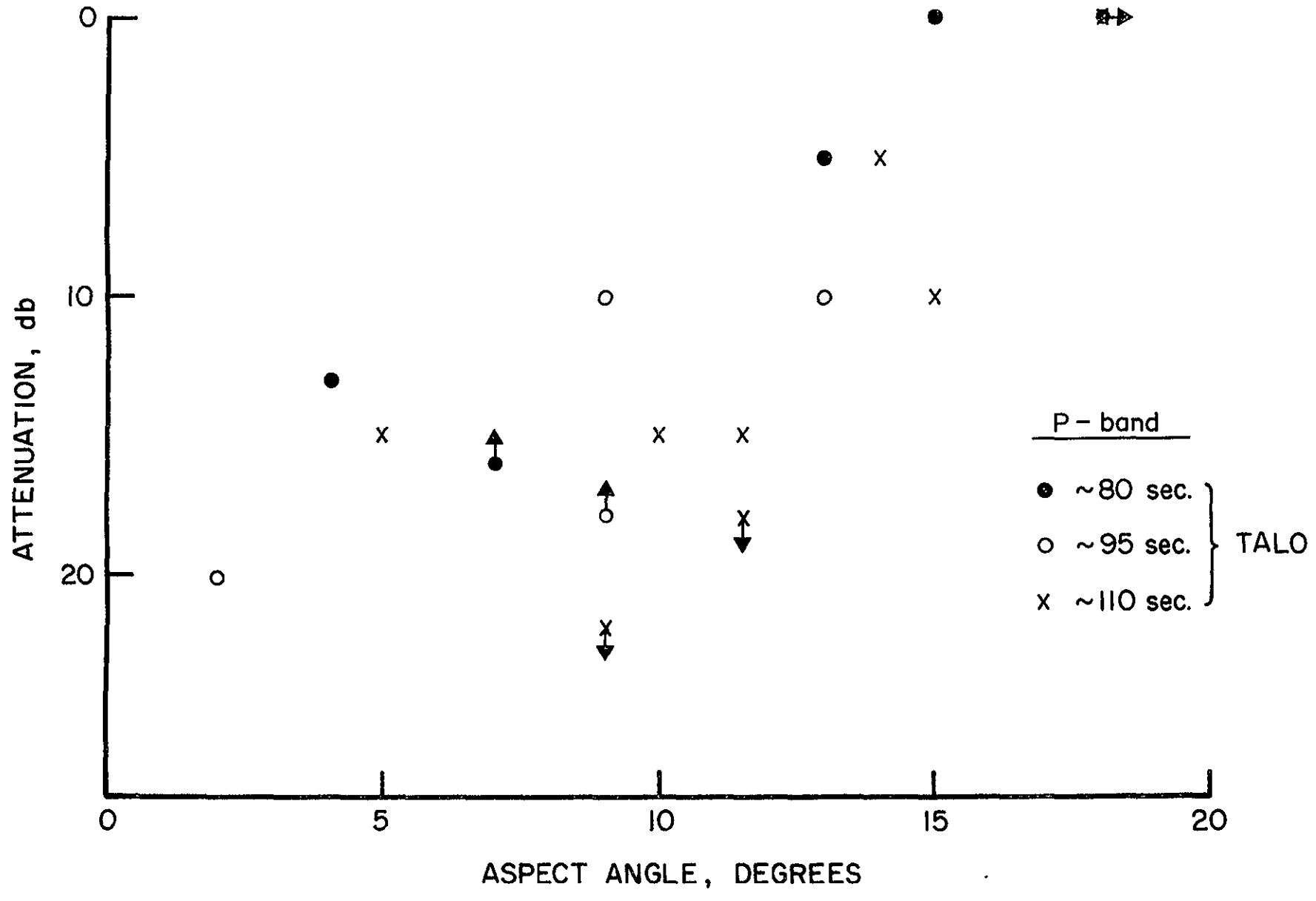

Figure 6. Attenuation levels at P-band (~250 MHz) as a function of polar aspect angle for Titan III-C at various altitudes.

Figure 6 shows the P-band data grouped into three altitude regimes; the attentuation here appears to be marginally greater at higher altitudes at a given aspect, but again no clear trend is evident.

At this point we shall anticipate the results of the following section and state that in general we expect, on theoretical grounds, an effect of both altitude and signal frequency upon the observed signal level. That there is no clear-cut dependence in the best available data is on its face somewhat perplexing. We conclude that a careful accounting of the various factors at work is required, since opposing trends and subtle interplays among them may be at work.

3.2 Theoretical Considerations

Signal transmission through an exhaust plume is an example of electromagnetic wave propagation through a lossy dielectric medium. It is convenient to divide the discussion into separate sections on the properties of the medium (the plume) and its effects upon a propagating wave.

The plume interferes with an RF signal because it contains free electrons and ions. These are produced by thermal ionization of alkali metal impurities in the propellant. These levels tend to be high (50-100 ppm) in

composite propellants because of the chemical similarity between sodium and potassium and the ammonium group present in the oxidizer (ammonium perchlorate), which makes purification difficult. Ionization occurs both in the combustion chamber and in the hot portions of the external flow. Once produced, electrons are removed by recombination with ions and by attachment to neutral atoms (principally oxygen and chlorine). The dielectric constant ε depends upon the propagation frequency determined by the electron number density N_e and their collision frequency with the neutral species (the fractional ionization level is always small, as is usually the ion contribution to ε). An explicit relation is

$$\varepsilon = 1 - \frac{\omega_p^2}{\omega^2 + \nu^2} + i \frac{\omega_p^2 \nu/\omega}{\omega^2 + \nu^2} \qquad (3\text{-}1)$$

where ω_p is the plasma frequency

$$\omega_p^2 = \frac{4\pi e^2 N_e}{m_o} = 3.2\times10^9 N_e \quad (\text{sec}^{-2} \text{ if } N_e \text{ in cm}^{-3}) \qquad (3\text{-}2)$$

(e is the electron's charge, and m_o its mass), and ω is the circular frequency of the transmitted radiation.

A more directly useful quantity is the refractive index, $n = \sqrt{\varepsilon}$. Suppose that a wave travels a small

distance δs in a medium whose refractive index is n. The ratio of the electric field at the end of this path to its value for free-space propagation over the same distance is

$$E_n/E_o = \exp\{i\, k(n-1)\ \delta s\} \tag{3-3}$$

where $k = \omega/c$ is the wavenumber. Because ε and thus n is complex, the exponent contains a real and an imaginary part:

$$E_n/E_o = \exp\ \{i\ k\ (n_r-1)\ \delta s - k\ n_i\ \delta s\} \tag{3-4}$$

The imaginary part of the exponent represents a phase shift of the field which results from the change in wave phase velocity as the refractive index varies from unity. The real part is negative and represents an attenuation of the wave, or in other words, a transfer of energy from the field to the medium. Both the real and imaginary parts of the refractive index increase with increasing electron density and decrease with increasing signal frequency. The dependence on collision frequency is more complicated. Explicit expressions for the real and imaginary parts of n are

$$n_r = \left\{ \frac{1 - X + Z^2}{2(1 + Z^2)} + \left[\frac{(1-X)^2 + Z^2}{4(1 + Z^2)} \right]^{\frac{1}{2}} \right\}^{\frac{1}{2}} \tag{3-5}$$

and

$$n_i = \frac{1}{2n_r} \left(\frac{XZ}{1 + Z^2} \right) \tag{3-6}$$

where

$$X = \omega_p^2/\omega^2 \tag{3-7}$$

and

$$Z = \nu/\omega \quad . \tag{3-8}$$

The parametric variation of n_r and n_i are shown in Figure 7 (Kelso, 1964).

The electron density and collision frequency, and thus the refractive index, vary with position and time within the exhaust plume. This variation is determined by the gas dynamics of the exhaust gases as they expand to ambient pressure, mixing of the exhaust with the atmosphere, and chemical reactions. The basic structure near the vehicle is determined by inertial and pressure forces as the exhaust expands on leaving the rocket nozzle, and for a single plume takes the form of a core expansion surrounded by a shock layer. Superimposed on this structure is a region where turbulent mixing of the exhaust and the ambient atmosphere takes place. This mixing region grows as the gases move away from the vehicle, while the pressure forces

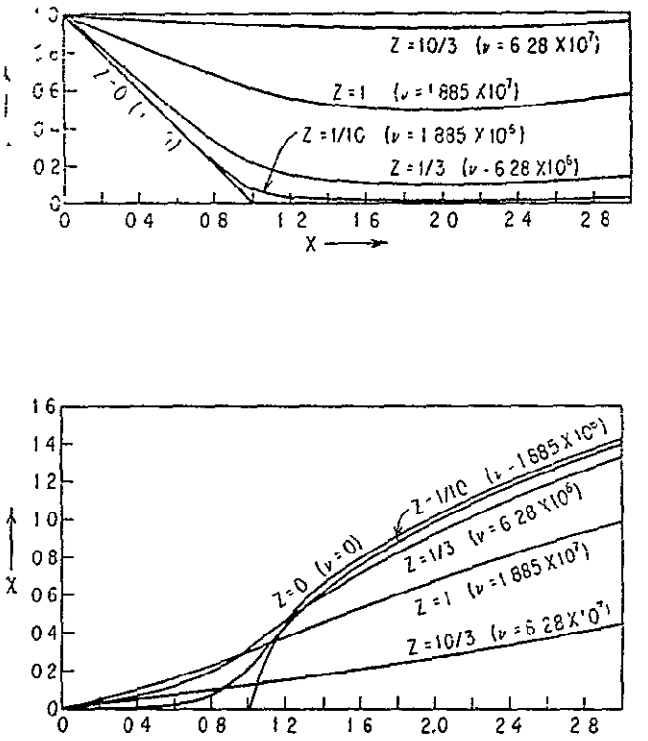

Figure 7. Real part μ and imaginary part X of the complex index of refraction as a function of the parameter $X = \omega_p^2/\omega^2$ for several values of the parameter $Z = \nu/\omega$. (Figures from Kelso, Radio Ray Propagation in the Ionosphere.)

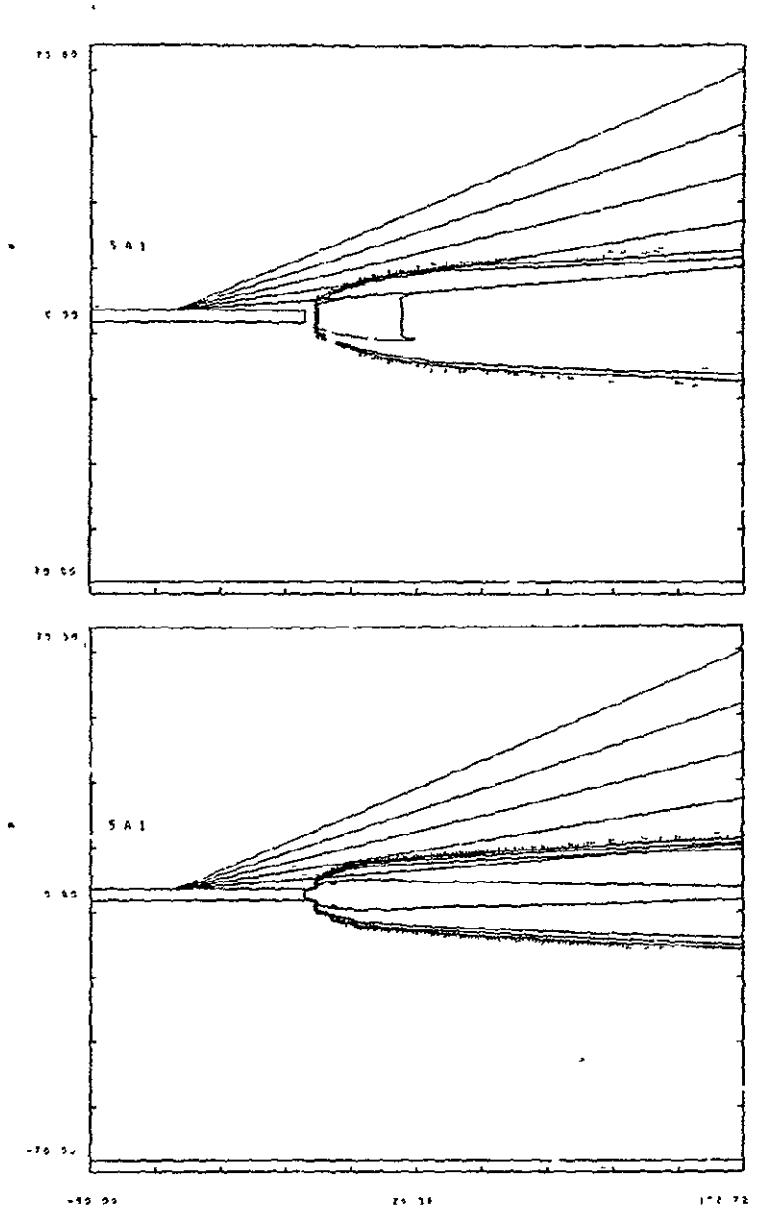

Figure 8. Calculated electron density contours (10^7, 10^8, 10^9, 10^{10}, and 10^{11} cm^{-3}) in exhaust plumes of a Titan III-C solid motor at 36 (top) and 20 km (bottom) altitude. Also shown are antenna lines of sight at 5, 10, 15, 20, and 25° aspect.

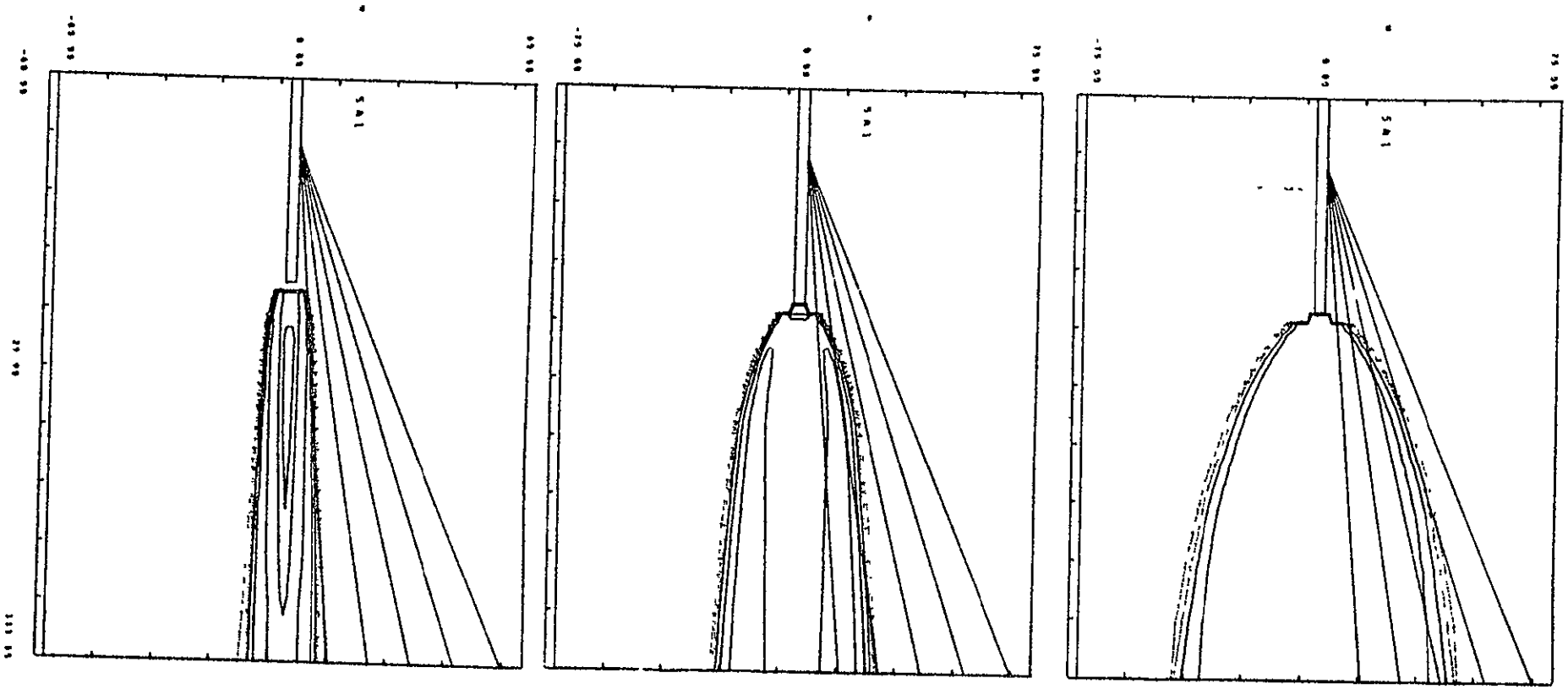

Figure 9. Calculated electron density contours (10^7, 10^8, 10^9, 10^{10}, 10^{11} cm^{-3}) in exhaust plumes of a Space Shuttle SRB at 38, 25, and 10 km (top to bottom) altitude. Also shown are antenna lines of sight at 5, 10, 15, 20, and 25° aspect.

diminish. Far downstream the exhaust gases are at the same pressure as the ambient atmosphere, and the further development of the flow is controlled by turbulent mixing.

Within the mixing region chemical reactions can occur which release heat to the flow field and cause additional ionization. Because the exhaust gases are generally fuel-rich, for reasons associated with motor performance, secondary combustion or afterburning can occur as they mix with air. The chemistry is fairly complex, but reasonably well understood. The reactions are generally out of equilibrium, so that ionization levels are determined by a complex set of rate processes.

Computer codes have been developed which treat the combined effects of expansion gas dynamics, mixing, and finite-rate chemistry to evaluate time-averaged electron density and collision frequency as a function of position in the plume. Some results of calculations performed at Lockheed Missiles and Space Company in support of this study are shown in Figures 9 and 10. At higher altitude, the plume is broader, longer, and less dense. For typical antenna locations the aspect angle at which the plume first intercepts a ray from the antenna increases with altitude. At the same time the difference of the refractive index from unity tends to decrease. Qualitatively, we expect the plume to be large but more transparent at higher altitude. Which

effect predominates will depend upon vehicle size, propellant, trajectory, and signal frequency.

Detailed calculations (e.g., Thomson, 1962) indicate that in the case of large and relatively highly ionized plumes, such as those from the SRM's for Titan III and the Space Shuttle, rays which enter the plume are both strongly absorbed and appreciably refracted. As a result, the plume casts a very dark shadow on the transmitted signal. Diffraction of rays which pass a short distance outside the shadowed region, though generally a weak effect because of the large value of the ratio of a characteristic plume radius to the signal wavelength, can produce signal levels in the shadowed regions which are several orders of magnitude greater than those associated with direct rays (Figure 10).

The interpretation of the signal near tail aspect, deep within the plume shadow, as a diffracted signal, has several implications as to the processes in the plume which determine the signal level. At any given signal frequency low enough that the plume is essentially opaque, the signal in the shadowed region is a sensitive function of the effective plume diameter and of conditions near the edge of the plume. The edge region is one of high mean electron density gradient, a consequence of diffusion and of the chemical processes which remove electrons from the flow.

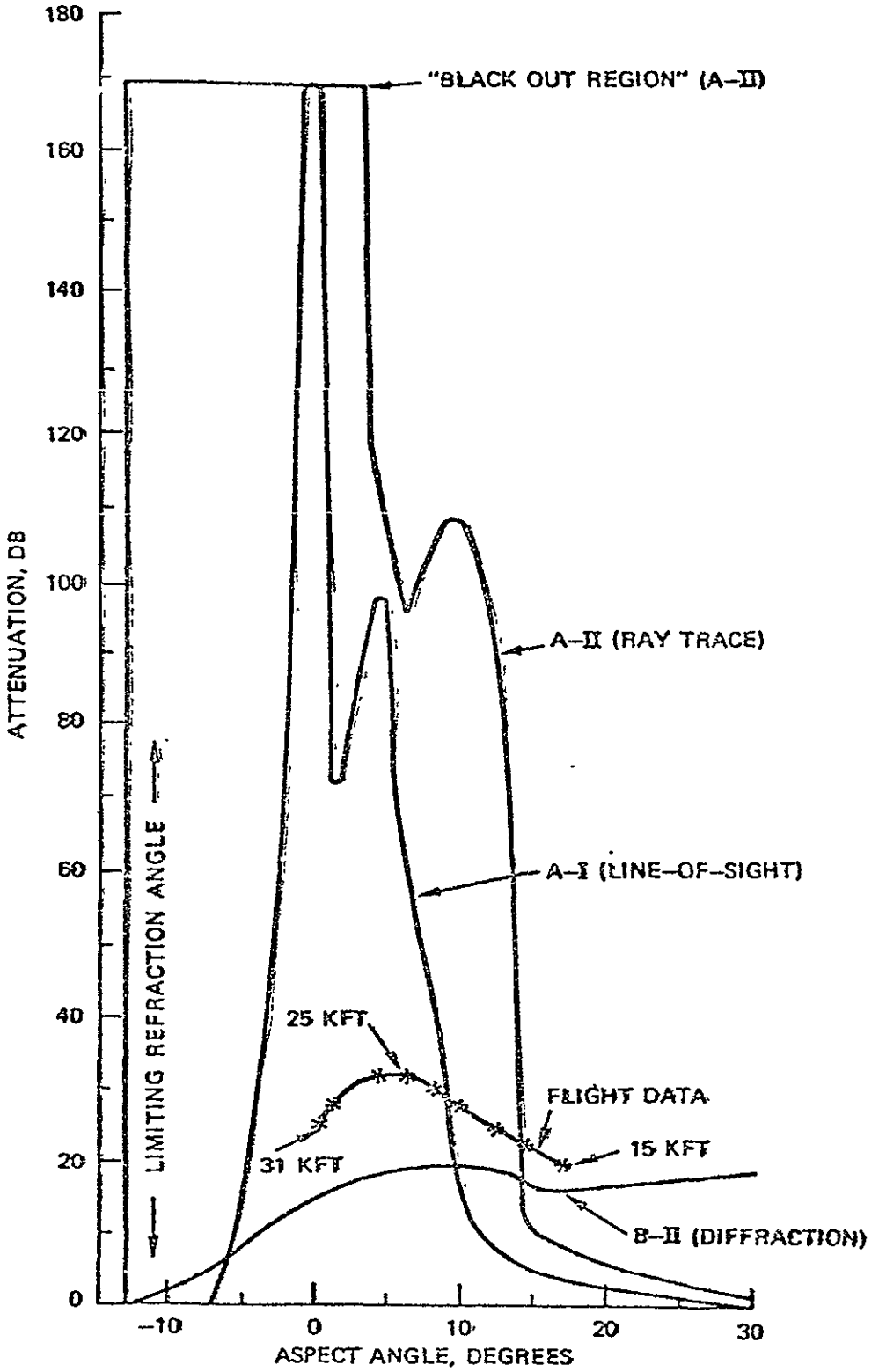

Figure 10. C-band attenuation calculations for ELP propellant in flight at 25,000 ft. altitude. (Flight data are shown for the altitude range 15,000 to 31,000 ft.) Data from Victor (1975).

It is also one in which the turbulent flow is intermittent. Large eddies sporadically convect highly ionized gas from the interior of the mixing zone into and out of this region; the actual plume edge will be at any instant an irregular structure dominated by this large eddy structure. Figure 11, a shadowgraph (Laufer, 1975) of conditions in a laboratory mixing layer between fluids of different density, illustrates the type of structure which we expect in the plume edge region. At a location where the mean electron density is (say) 10^8, with interior densities of 10^{10}, the mean density is more likely a consequence of the local condition being 10^{10} one percent of the time than of its being 10^8 all the time. The RF signal responds to the instantaneous structure of the plume.

The interpretation of the shadow zone signal as a diffracted signal also leads to an opposite dependence on frequency and altitude to what one would have expected for a transmitted signal. At higher frequencies (yet low enough that the plume is opaque) the signal propagation is more nearly geometric, so that one expects a reduced tail-aspect signal as the frequency is increased. At higher altitudes (yet not so high that the plume becomes transparent) the shadowed zone is broader, and the filling in of the shadowed region by diffraction is reduced. On the other hand, to the

Figure 11. Shadowgraph of a mixing layer produced by helium (upper side) at U_1 = 1015 cm/sec and nitrogen at U_2 = 384 cm/sec at a pressure of 8 atm (from Laufer).

extent that edge gradients are somewhat smooth, the plume shadow will be somewhat less broad at higher frequencies.

4.0 COMPUTATIONAL PROCEDURES

In order to calculate plume-induced signal attenuation we should employ a physical optics procedure which accounts for the combined effects of absorption, refraction, and diffraction. In this section we describe such a procedure. Similar techniques have previously been applied to RF propagation in the ionosphere (Chestnut, 1972; Watson and Thomson, 1972), laser beam propagation and thermal blooming in the lower atmosphere (Fleck, Morris, and Feit, 1975; Berger, et al., 1977) and sound propagation in the ocean (Flatte and Tappert, 1972). The application to plume-signal interference is novel, and we therefore describe the procedure in some detail. The procedure is developed in a heuristic fashion; a more formal development is given in the Appendix. We begin by discussing the wave propagation problem in free space. A treatment of absorption and refraction in a material medium is then introduced. Finally, we discuss procedures employed to reduce numerical problems arising from ray divergence and other factors.

Before beginning, we may refer back to Figure 10 to note that the deflection angles of rays refracted by or diffracted around the plume are small (generally less than 10-20°). Under these conditions propagation and scatter take place in a generally forward direction. We may therefore

characterize the propagating wave by a wave vector $\vec{k}$ which is in the nominal direction of propagation, and employ small-angle approximations ($\cos\theta \approx 1$, $\sin\theta \approx \tan\theta \approx \theta$) throughout. This behavior considerably simplifies the analysis and is appropriate so long as we consider a transmitted (or forward-scattered) signal rather than reflection or backscatter.

4.1 A Free-Space Propagation Algorithm

Kirchoff's integral relation, the mathematical statement of Huggens' principle, is the basis of physical optics diffraction theory. As originally developed it is a scalar theory, although vector formulations have been developed (Jackson, 1962). Since plume dimensions are typically large with respect to a wavelength and vector wave corrections are important only when wavelength and aperture dimensions are comparable, the scalar formulation is adequate for our purposes. Let us assume that we know the field amplitude ψ on a plane $Z = Z_o$ normal to the nominal propagation path, which we take to be along the Z axis. Then the field at points on a plane $Z = Z_1$ some distance further along the Z axis is given by the relation

$$\psi(x_1,y_1,z_1) = \frac{1}{2\pi i} k \int_{-\infty}^{\infty}\int_{-\infty}^{\infty} \psi(x_o,y_o,z_o)\ e^{ikr}\ r^{-1}\ dx_o\ dy_o \tag{4-1}$$

where r is the distance between (x_o,y_o,z_o) and (x_1,y_1,z_1).

Since r is

$$r = [(x_1-x_o)^2 + (y_1-y_o)^2 + (z_1-z_o)^2]^{\frac{1}{2}} \qquad (4\text{-}2)$$

the term multiplying the known field in (4-1) is, at a given distance between planes, a function of (x_1-x_o) and (y_1-y_o). Thus, the field at $Z = Z_1$ can be expressed as a convolution,

$$\psi(x_1,y_1) = \int_{-\infty}^{\infty}\int_{-\infty}^{\infty}\psi(x_o,y_o)\ F(x_1-x_o,\ y_1-y_o)\ dx_o\ dy_o\ . \qquad (4\text{-}3)$$

The easiest way to evaluate this convolution, when the number of points in each plane is large, is to multiply the Fourier transforms of ψ and F:

$$\hat{\psi}(k_x,k_y)\Big|_{Z=Z_1} = \hat{\psi}(k_x,k_y)\Big|_{Z=Z_o} \cdot \hat{F}(k_x,k_y) \qquad (4\text{-}4)$$

where the tilde denotes a transformed function. Fast Fourier transforms (FFT's) allow these operations to be done rapidly, with a number of steps proportional to $N_x\ N_y\ \log_2\ (N_x\ N_y)$ instead of the $N_x^2\ N_y^2$ operations required by direct integration at every point.

An efficient computational procedure for evaluating forward wave propagation in free space thus consists of the following steps:

1. Evaluate the Fourier transforms of $\psi(x_o,y_o)$ and the propagation kernel F.
2. Multiply the transforms at each point in k-space to obtain the transform of their convolution.
3. Evaluate the inverse transform to obtain $\psi(x_1,y_1)$.

The process is repeated for however many planes at which one wants to have the field explicitly displayed.

For the Kirchoff integral in the form of Equation (4-1), the Fourier transform of the propagation kernel F cannot be expressed in any simple analytic form. However, by invoking the Fresnel approximation

$$F = \frac{e^{ikr}}{r} \approx \frac{k}{2\pi i(Z-Z_o)} \exp\left\{ik[(x_1-x_o)^2 + (y_1-y_o)^2]/2\ (z_1-z_o) + ik(z_1-z_o)\right\} \qquad (4\text{-}5)$$

we immediately obtain

$$\hat{F} = \frac{e^{ik(z_1-z_o)}}{z_1-z_o} \exp\left\{i(z-z_o)\ (k_x^2+k_y^2)/2\ k\right\}. \qquad (4\text{-}6)$$

Here we assume that the deviation from forward propagation is small enough that we may neglect differences in $|r|$ as

they affect the modulus of the wave reaching z_1, but do not restrict these differences to be small with respect to a wavelength, so that phase effects are important. Since we are considering essentially forward propagation, this version of the small-angle approximation is adequate.

A representative application of this procedure to simple diffraction problems is shown in Figure 12 and 13. In the second of these we show the calculated far-field (Fraunhofer) diffraction pattern of a rectanular aperture, and in the first a photograph from Jenkins and White (1957).

4.2 Effects of a Dielectric Medium

Instead of propagation in free space, we want to treat propagation in a medium whose refractive index varies with position. Let us first consider a thin slab of intervening material and see how we might modify the treatment for this case. Referring to Figure 14, we consider a source field on the plane $z = z_o$, a slab of dielectric material centered about the plane $z = z_1$, and ask for the resulting field amplitudes on the plane $z = z_2$. Beginning with the field at z_o, we calculate the field incident upon

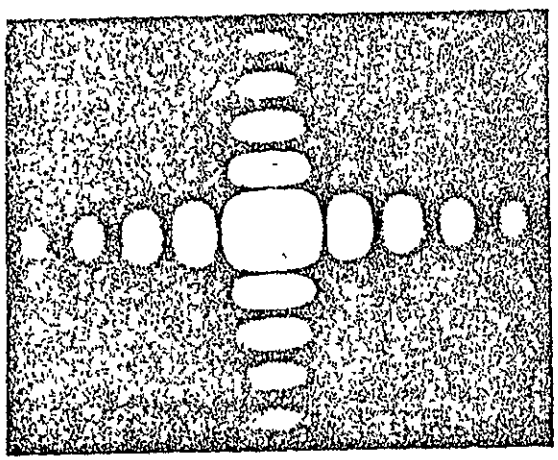

8×7

Figure 12. Fraunhofer diffraction of a rectangular aperture (from Jenkins and White, Fundamentals of Optics).

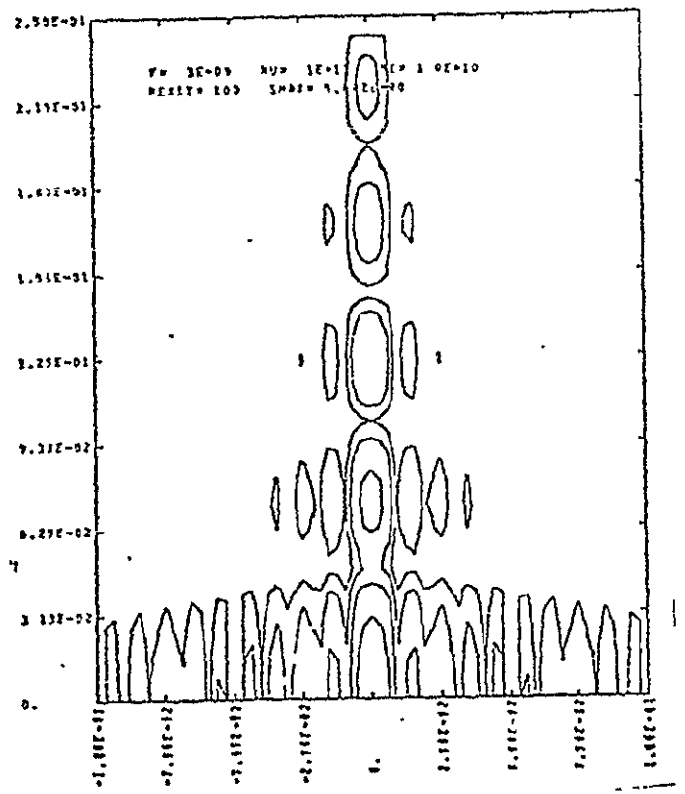

2×10

Figure 13. Calculated Fraunhofer diffraction pattern of a rectangular aperture showing contours of constant intensity. Calculation is symmetric about the abscissa.

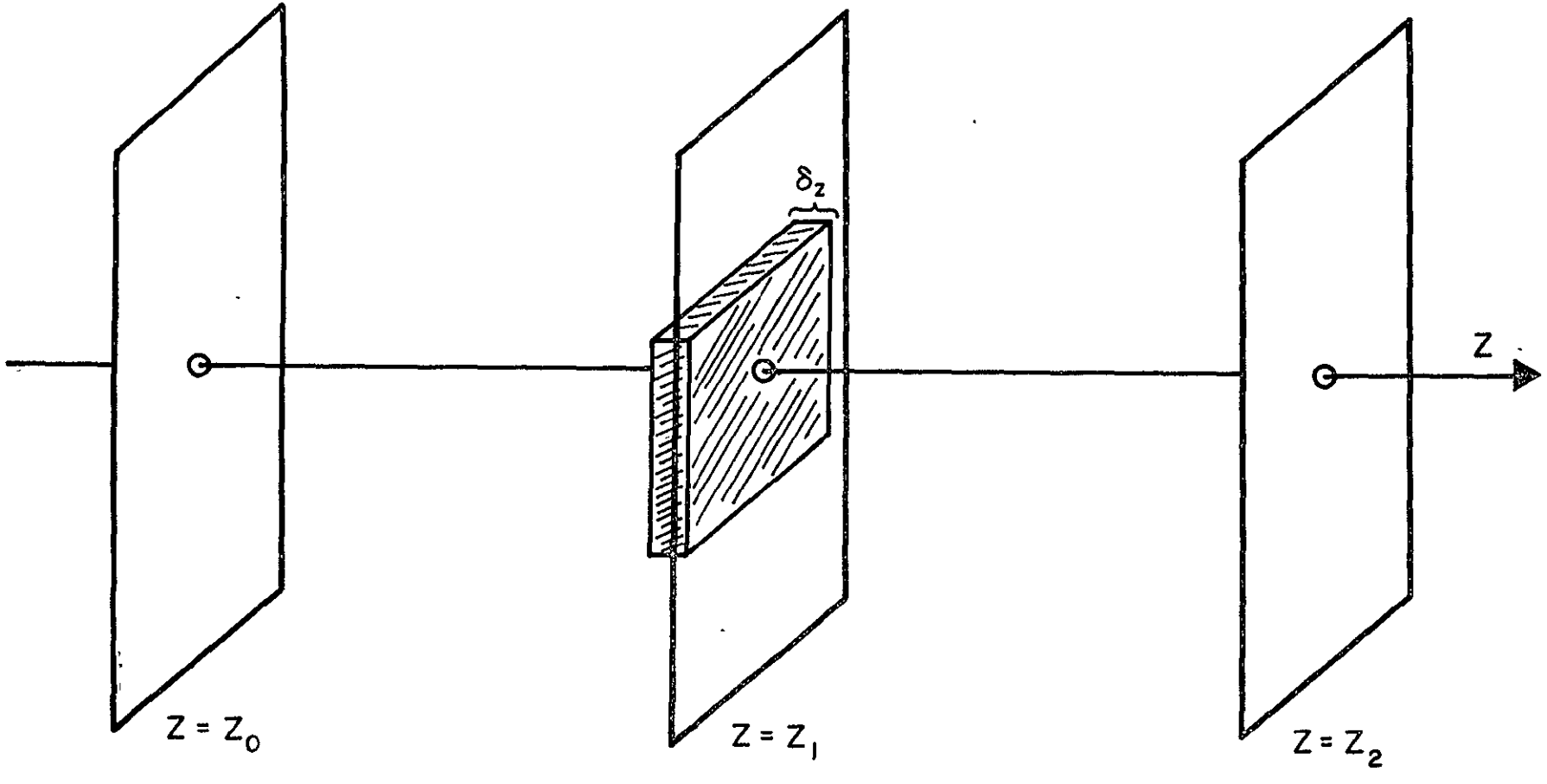

Figure 14. Geometry for effects of a dielectric medium on signal propagation.

the slab by applying the free-space propagation algorithm between z_o and z_1. The wave emerging from the slab, according to the discussion in Section 3.2, is a wave which is corrected in amplitude and phase:

$$\psi(x,y,z_1 + \tfrac{1}{2}\sqrt{z}) = \psi(x,y,z_1 - \tfrac{1}{2}\sqrt{z}) \exp\left\{ i[n_r(x,y)-1]\, k\, \delta z - [n_1(x,y)\, k\, \delta z] + i\, k\, \delta z \right\} . \qquad (4\text{-}7)$$

The last term in the exponent is a position-independent phase correction and can be dropped. The second term represents absorption by the slab, and the first term a position-dependent phase shift. The phase fronts of the emerging wave will be tilted with respect to those of the incident wave to the extent that the real part of n varies with position; this is equivalent to a change in direction of the wave, and corresponds to refraction by the gradients in the slab perpendicular to the nominal propagation direction (the z axis). By applying the free-space propagation of the emergent wave at z_1, we can evaluate the field at z_2.

The extension of this procedure to a thick medium is straightforward. We divide the medium into a number of slabs j separated by distance Δz_j. Between each adjacent pair of slabs we allow the wave to propagate as if in free

space using FFT's to evaluate the Fresnel-Kirchoff integral. At each z station z_j we apply an amplitude and phase correction at each of a preselected set of grid points, appropriate to the local refractive index and the slab thickness Δz_j. The corrected wave is then propagated to the next location z_{j+1}, and this process of alternate propagation and correction is completed until the entire medium has been traversed. Once through the medium, a final propagation step gives the transmitted field at any desired distance. The process is shown schematically in Figure 15.

It can be shown (e.g., Fleck, et al., 1975) that this algorithm is a solution, correct to second order in Δz, of the parabolic wave equation

$$2ik \frac{\partial \psi}{\partial z} = \nabla_\perp^2 \psi + k^2(n^2-1)\ \psi \quad . \tag{4-8}$$

The assumptions employed in deriving Equation (4-8) are equivalent to the Fresnel approximation. In operator form the solution is formally expressed as

$$\psi_{j+1} = e^{-\frac{i\ \Delta z\ \nabla_\perp^2}{4k}}\ e^{-\frac{ik}{2}\ \Delta z \overline{(n^2-1)}}\ e^{-\frac{i\ \Delta z\ \nabla_\perp^2}{4k}}\ \psi_j \tag{4-9}$$

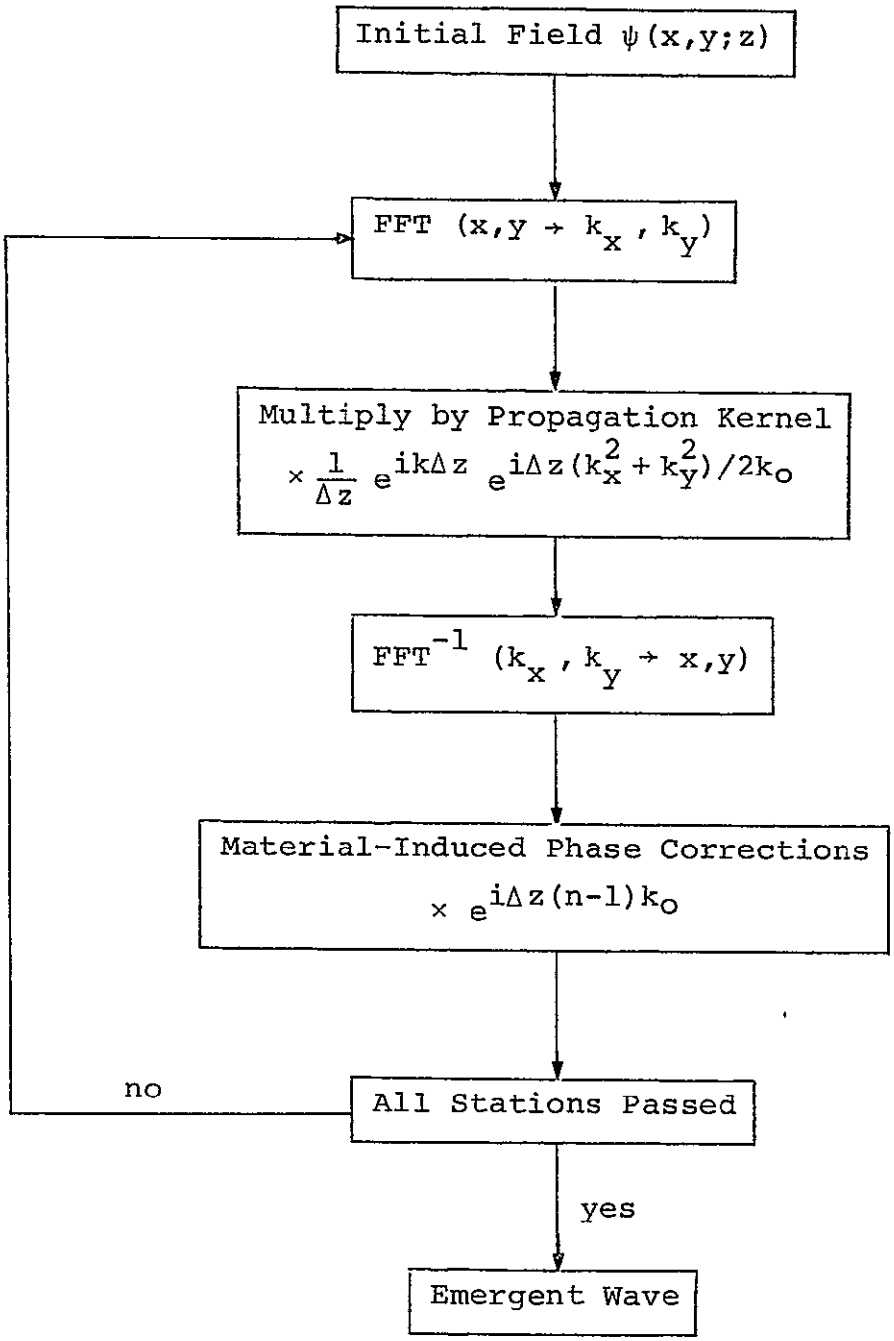

Figure 15. Schematic process of evaluation of signal propagation in an absorbing and refracting medium.

where

$$\nabla_{\perp}^2 = \frac{\partial^2}{\partial x^2} + \frac{\partial^2}{\partial y^2} \qquad (4\text{-}10)$$

and

$$\overline{(n^2-1)} = \frac{1}{\Delta z} \int_{z_j}^{z_{j+1}} (n^2-1)\, dz \approx \frac{2}{\Delta z} \int_{z_j}^{z_{j+1}} (n-1)\, dz \quad . \qquad (4\text{-}11)$$

The algorithm is also applicable to nonlinear wave propagation, in which the local refractive index is a function of the local field amplitude, and has been widely used in that field.

At this point we have available a computational procedure which includes the effects of refraction, absorption, and diffraction in a single calculation. Because each point on the plane $z = z_{j+1}$ is affected by every point on the previous plane $z = z_j$, the procedure includes multipath effects. The phase-correction step is applied at $N_x N_y$ points in each plane, while the convolution operation requires a number of steps proportional to $N_x N_y \log_2 (N_x N_y)$. For a large number of points, the total computation time is therefore roughly proportional to $N_x N_y N_z$, and the field amplitude is determined at each of $N_x N_y$ points in the target (or ground) plane.

4.3 Some Numerical Details

Several problems arise in applying this procedure to propagation in an exhaust plume to or from a wide-angle antenna.* These are primarily associated with the divergence of the rays from the antenna. The convolution of Equation (4-1) in principle requires an integration over the entire plane $z = z_o$. In approximating it by a finite-range discrete Fourier transform, we leave ourselves open to errors arising from the finite mesh spacing in both physical (x) and Fourier (k) space. These mesh sizes are related as

$$\delta k = \frac{2\pi}{N_x \delta x} \tag{4-12}$$

When we limit the range in physical space, we eliminate the low-wavenumber Fourier components lying between δk and $k = 0$. This imposes an implicit assumption that the function is periodic in x space. A similar assumption of periodicity in k space results from the fact that we choose a finite mesh size in x space. Because the function is implicitly periodic, a result which runs into the mesh boundaries in either space results in a calculation in one periodic cell

*A well-known reciprocity theorem allows us to treat the propagation in whichever direction is convenient, since the signal losses along any path in either direction are equal.

containing contributions which are in reality associated with an adjacent cell. In Fourier space this behavior is called aliasing; high-wavenumber components appear as effective low-wavenumber components. In physical space it is called imaging; effects which should appear at large x appear at small x. It is as if ghost or image solutions developed in the computational cell adjacent to the one in which we are interested, and our solution contained contributions from these images. Thus, once the rays from the antenna reach the edge of the grid, it is as if we were seeing contributions from antennas not only at (say) $(x=0, y=0)$ but also from antennas at $(x = N_x\ \delta x, y=0)$, $(x=0, y = N_y\ \delta y)$, $(x = -N_x\ \delta x, y=0)$, $(x=0, y = -N_x\ \delta y)$, and so on (see Figure 16). Brigham (1974) gives a very clear description of these aliasing and imaging phenomena (Gibbs phenomena) and shows how they are related to the properties of discrete Fourier transforms.

Since we have no a priori way of eliminating these image contributions to the computed field once they occur, we seek a procedure which minimizes or eliminates their occurrence. A coordinate transformation due originally to Talanov (1970) has been found useful in treating focused laser beams, where similar problems arise. Talanov's transformation is readily applied here. We write the field on

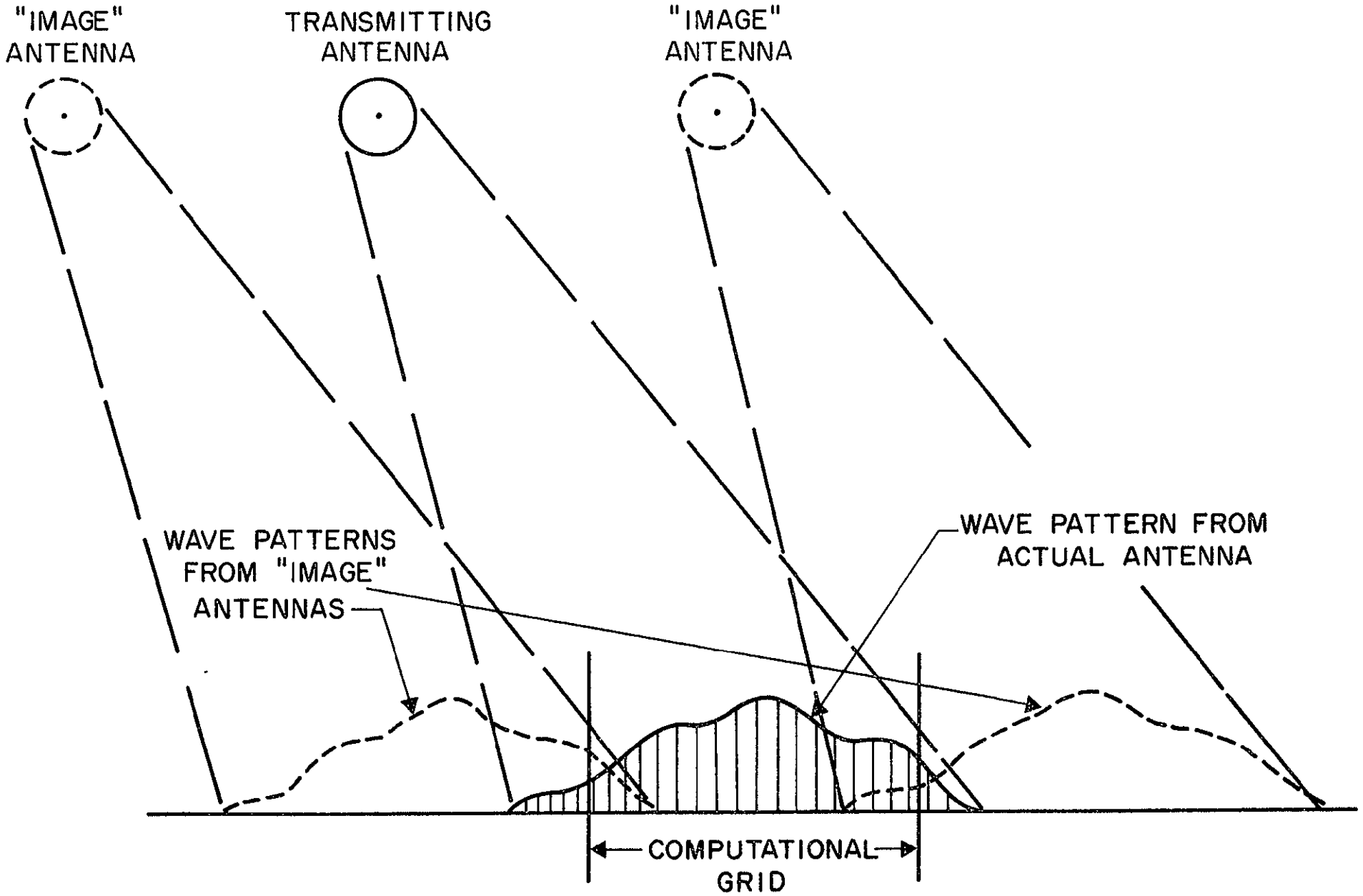

Figure 16. Imaging (leakage) effects caused by discrete resolution on a limited grid.

some plane $z = z_j$ as the produce of some function $\psi'(x,y,z_j)$ and a spherically symmetric phase factor:

$$\psi(x,y,z_j) = \psi'(x,y,z_j)\, e^{ik(x^2+y^2)/2\, z_f} \qquad (4\text{-}13)$$

where z_f is the focal length of the lens which produced the wave front represented by the phase factor (positive for converging beams and negative for diverging beams). Then the freely propagating wave at $z = z_{j+1}$ can be expressed as

$$\psi(x,y,z_{j+1}) = \frac{1}{1-\Delta z/z_f}\, \psi'\left(\frac{x}{1-\Delta z/z_f}, \frac{y}{1-\Delta z/z_f}, z_j + \frac{z_{j+1} - z_j}{1-\Delta z/z_f}\right)$$

$$\times \exp\left\{ik(x^2+y^2)/[2\, z_f(1-\Delta z/z_f)]\right\} \quad . \qquad (4\text{-}14)$$

Applying this transformation involves the following steps:

1. Divide the known field ψ at each point of the plane $z = z_j$ by the phase factor to obtain the residual field ψ'.
2. Calculate the field ψ' at the plane $z = z_{j+1}$ using the algorithm of Section 4.1.
3. Rescale the field amplitude and the mesh according to the relations

$$\left.\begin{aligned} \psi'' &= \psi' \frac{1}{1-\Delta z/z_f} \\ x' &= x(1-\Delta z/z_f) \\ y' &= y(1-\Delta z/z_f) \end{aligned}\right\} \quad (4\text{-}15)$$

4. Correct the phase of ψ'' at each point of the plane $z = z_{j+1}$ by multiplying by the phase factor

$$e^{ik(x'^2+y'^2)/2(z_f-\Delta z)} .$$

The phase and amplitude corrections introduced by the medium are then introduced as in Section 4.2 and the calculation is continued to the next z station.

This transformation converts a spherical wave (in the small-angle approximation) into a plane wave. The mesh on which the field is evaluated thus grows or shrinks as the calculation proceeds, as the focal point is behind or in front of the station being considered. The propagation algorithm, given a uniform plane wave at $z = z_J$ (which has only a $k = 0$ Fourier component) maintains it as a uniform plane wave at all successive stations. The combination of this algorithm and the Talanov transformation also maintains the character of a (small-angle) spherical wave. It will also preserve a

Fraunhofer diffraction pattern, provided that the calculation is initiated at some station at which the wavelength is very small with respect to the product of a pattern dimension times a diffraction angle.

In applying this procedure to the plume-signal interference problem, we generally assume the focal point to be at the antenna. For most conditions of interest, the antenna is located far enough forward on the vehicle that the angle subtended by the plume is small (of order 20°), so that we can consider both the plume and the space for some distance around it within the confines of the small-angle approximation. Three-dimensional flow fields can be treated as easily as axially symmetric ones, and local inhomogeneities are accommodated to the resolution of the mesh.

Since the outer regions of the plume are reflecting, an additional ray divergence is introduced over and above that of the initital spherical wave. Depending on the reflection angle, these rays can sometimes get to the mesh boundary and cause image effects. It is usually easy to recognize these if they are not too strong, but they are an artifact of the calculation. Likewise, rapid variations in plume conditions in a plane introduce high-wavenumber Fourier components and the possibility of aliasing in Fourier space. It is usually desirable to introduce a rolloff

factor which reduces the contribution of the high-k components (and thus may eliminate some fine structure from the result). An apparently satisfactory formulation is

$$\psi_{corr} = \psi_{calc} \exp\left\{-\left[(k_x^2 + k_y^2)/2k_{max}^2\right]^p\right\} \quad , \quad p \geq 1$$

where $k_{max} = \pi/\delta x$ is the maximum wavenumber carried. A similar reduction can be applied to the values of the field near the edge of the grid in x-space; here the factor is applied to the difference from the pure spherical wave. A suitable correction here is the split Hanning function

$$\psi_{corr} = \psi_{calc} \qquad |x| \, , |y| < x_1 \, , y_1$$

$$\psi_{corr} = \psi_{calc} \frac{1}{4}\left[1 + \cos\left(\pi \frac{|x| - x_1}{x_{max} - x_1}\right)\right]$$

$$\left[1 + \cos\left(\pi \frac{|y| - y_1}{y_{max} - y_1}\right)\right] \quad , \; |x| \, , |y| > x_1 \, , y_1$$

with x_1 and y_1 suitably chosen transition values. This treatment is characteristic of many numerical operations (such as digital filtering) involving discrete Fourier transforms.

In the calculations reported here, we have generally employed a 64 by 64 grid. At the point where the plume subtends its maximum angle, between on-third and one-half

of the grid dimension lies within the plume. Thus, 20 to 30 radial points are given within the flow field (less at other stations). This allows a flow field resolution comparable to that of a normal flow field calculation. In some cases we have experimented with a 128 by 128 point grid; the solution for the mean plume is only slightly different from that evaluated with the smaller grid when a mean (time-averaged) flow field is used. A 32 by 32 grid, however, usually causes some loss in quality.

5.0 EXHAUST PLUME FLOW FIELDS

The flow fields for both the Shuttle and Titan III-C exhaust plumes were furnished by Lockheed Missiles and Space Company, Huntsville Research and Engineering Center. Two separate codes are used to evaluate conditions in the portion of the plume which is expanding to ambient pressure and in the downstream pressure-equilibrated trail. The code used in the upstream region (RAMP; Penney, et al., 1976) is essentially a viscous method-of-characteristics solution; the code used downstream (LAMP) is an extended version of the LAPP code developed at Aerochem Research Laboratories (Mikatarian, et al., 1972). Both codes employ a two-equation turbulence model to describe the (time-average) mixing of the exhaust with air. Secondary combustion and ionization-deionization chemistry are included in both codes.

The major limitations to these calculations are, first, the assumption of axial symmetry, and second, their treatment of a mean rather than an instantaneous flow field. The large separation of the SRM's on both Titan III-C and Space Shuttle gives their exhaust plumes a pronounced three-dimensional character, especially at lower altitudes. Figures 17 and 18 illustrate the interaction between the exhuast plumes at two different altitudes. At low altitude the plumes are essentially separate. Such interaction as does occur is primarily due to mixing, and in regions in which

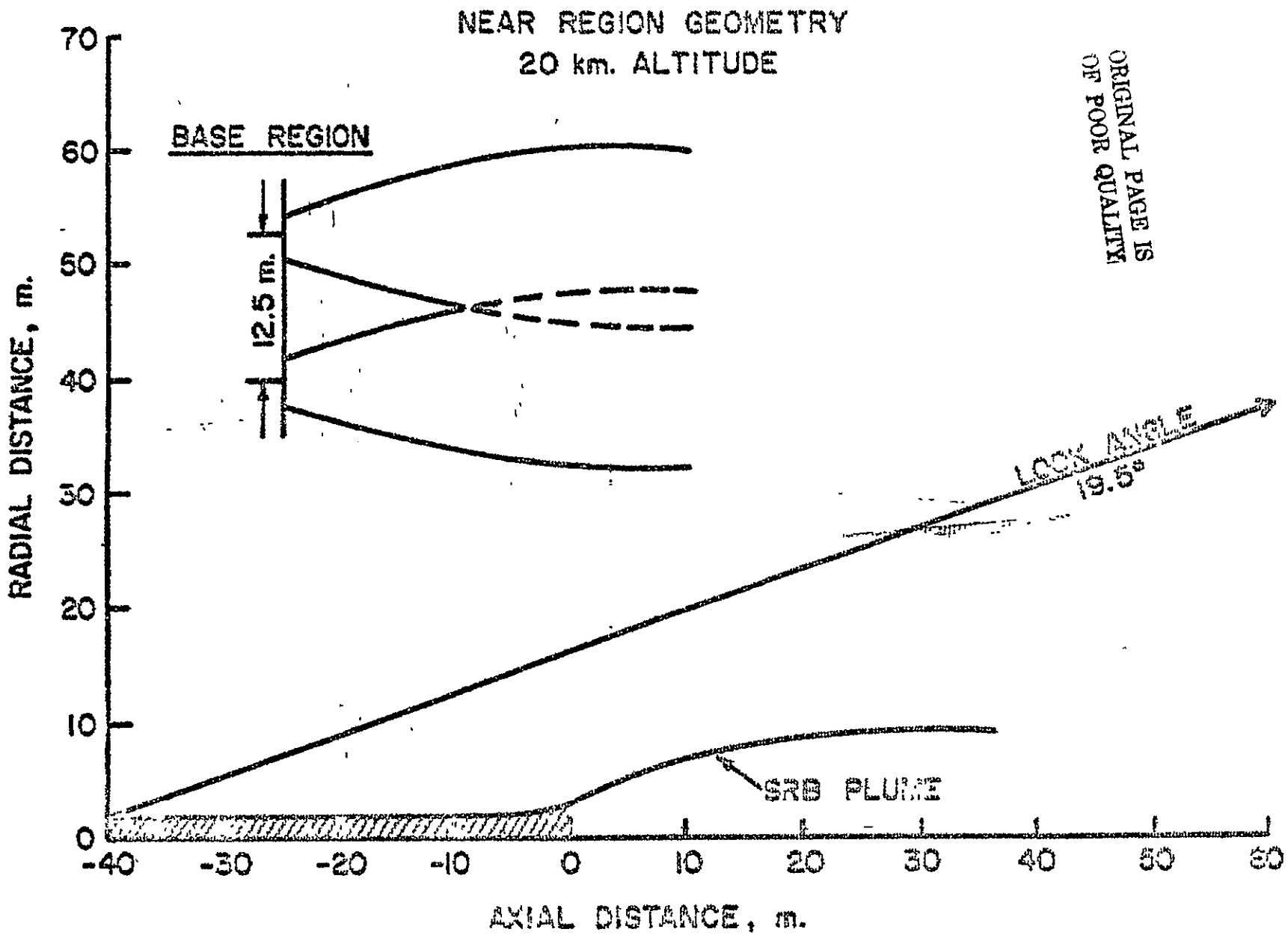

Figure 17. Estimate of SRB plume boundary location at 20 km.

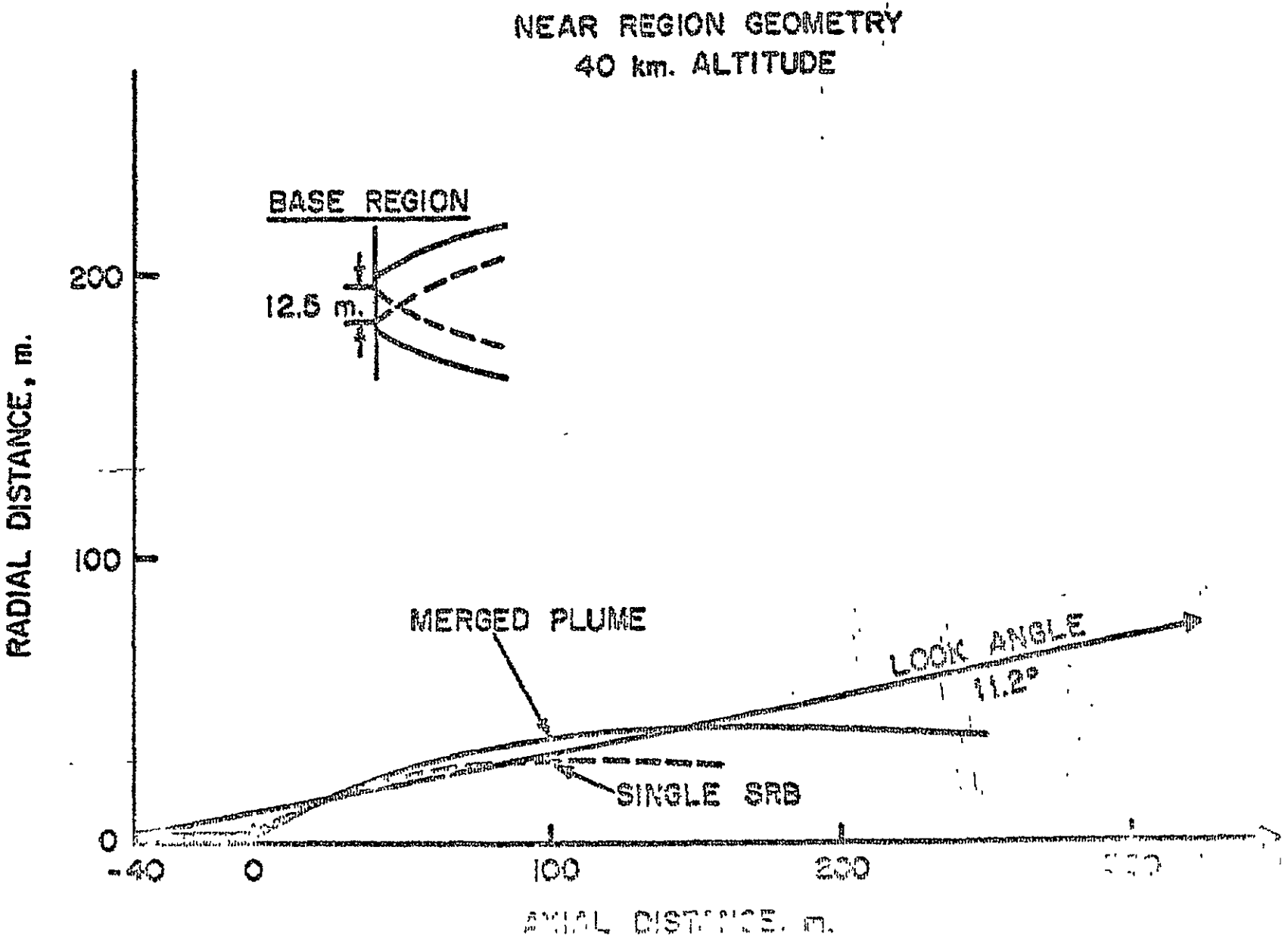

Figure 18. Estimate of SRB plume boundary locations at 40 km.

the concentration of exhaust gas is low. Under these circumstances it is reasonable to evaluate the two plumes independently and to calculate the electrical properties in the overlap region by linear superposition of the two flow fields. At high altitude (near SRM burnout) the plume size is large compared to the motor separation, and it is convenient to treat the combined plume as if it issued from a single nozzle. This treatment has been shown to give good overall plume shapes at very high altitudes, although, of course, the details of the region near the vehicle are not properly described. At intermediate altitude neither treatment is very satisfactory. However, since low-cost procedures for treating three-dimensional plumes including mixing and chemistry are not available, we have adopted the expedient of running the propagation calculation for both superposed and merged plume flow fields, in the expectation that the difference between them will provide some indication of the reliability of the result.

The plume calculation predicts a mean flow field which is the ensemble (or time) average over a large sample of instantaneous flow fields created by the somewhat random processes of turbulent convection. The pattern of these instantaneous flow fields is irregular on the scale of a mixing layer thickness as a result of the large eddy structure

of the flow (Figure 11), although when averaged the flow properties are smoothly varying on this scale. The transmitted signal passes through a large eddy in a time ℓ/c, where ℓ is an eddy dimension. A rough estimate for the overturning time of this eddy is $2\pi\ell/\Delta u$, where Δu is the velocity difference from one side of the eddy to another (of order 1 km/sec). Thus, the signal moves through (or past) the eddy in a fraction of order $\pi\Delta u/c \approx 10^{-5}$ of its characteristic rotation time. The signal thus sees a succession of instantaneous flow structures; plume-induced noise is essentially the result of differences in signal properties resulting from passage through and around these structures. In addition, the mean transmitted signal, being a nonlinear function of the flow structure, is not the same when treated as the result of interaction with a time-averaged flow field as it is when (correctly) treated as the average of many interactions with different instantaneous flow fields.

Because the propagation calculation is relatively efficient, it becomes feasible to attempt to model this process by constructing several realizations of the turbulent plume, propagating the signal through each of them, and then (incoherently) averaging the results. If we could simulate the turbulent field exactly, and perform the propa-

gation calculation on a fine enough mesh, this would provide an exact solution* for the time-dependent signal strength, from which we could then infer not only mean signal level, but also many of the noise characteristics induced by the plume. This approach has proven quite fruitful in investigations of the propagation of optical and RF beams through the atmosphere. In the present case, we are limited in the resolution available, and we can only hope to model some of the grosser features of the effects of turbulence.

Although gross, these features are of interest to signal propagation. Inhomogeneities in the plume are expected to have a measurable effect on the signal when the scale of the inhomogeneity, ℓ, times the difference between the wave vectors of the scattered and incident signal, Δk, is of order 2π. For small-angle scattering $\Delta k \approx k\Delta\theta$, where $\Delta\theta$ is the scattering angle, and so $\ell\ k\ \Delta\theta/2\pi = \ell\ \Delta\theta/\lambda \approx 1$. For the range safety signal $\lambda = 0.74$ meters, and for S-band $\lambda = 0.14$ meters. According to field measurements, scattering angles from 0 to about 0.25 radians are of interest. The scales of interest are therefore greater than about 3 meters

*To the order of the approximations invoked in developing the propagation algorithm.

for the Range Safety signal and greater than about 0.5 meters for the S-band link. Scales of order 1-2 meters are typically resolvable in the propagation calculation near the region where the plume subtends its greatest angle with respect to the roll axis. We should therefore expect that we can obtain a reasonable estimate of the effects of turbulence on the signal at VHF or UHF frequencies, and a somewhat cruder estimate at S-band. Some of the noise features should also come from such a calculation, although actual simulation of the time-dependent signal strength would require a great deal of computation.

Because the plume is overdense and highly absorbing except in the outer regions of the mixing layer, we should expect some differences between turbulent effects in plume interference and those in (for example) optical propagation through the atmosphere. A prominent feature of this region is convection of material from the inner regions of the plume by large eddies (of the order of the mixing layer width in size). The flow here is essentially intermittent, so that time-resolved measurements of local properties at some fixed position would show periods of high electron density alternating with periods in which the electron density was

very low. The probability distribution function of the electron density would tend to be bimodal, being the sum of an ambient distribution (essentially a delta function) and a function characteristic of regions further inside the mixing layer. This bimodality of the distribution function is clearly shown in measurements of temperature fluctuations in a mixing region between hot and cold air by La Rue and Libby (1974).

It has often been observed that the boundaries of turbulent shear flows exhibit a sharp interface between regions of turbulent and non-turbulent flow. The properties of this interface have been the object of considerable study; La Rue and Libby (1976) have recently summarized and extended these studies. Here we can consider the small-scale turbulence or some other property of the turbulent fluid (elevated temperature in the case of La Rue and Libby) as a marker for fluid on the inside of the interface. It is found that many of the statistical properties of the interface (including the fact that the intermittency factor* is an error function of distance transverse to the mean flow, that the probability distribution of the crossing frequency at a point is essentially Gaussian, and the probability distributions of the durations of turbulent and non-turbulent

*Defined as the fraction of time that fluid at a given position is turbulent or hot.

fluid passage) are well described by considering the position of the interface $\vec{x}_I$ to be a Gaussian-distributed random variable. (Alternatively, we could consider the displacement $\vec{D}_I$ from its mean position to be the Gaussian variable.) Although certain fine details of the interface are not so well described by this model,* it is an excellent approximation for the gross features.

These observations suggest that a productive treatment of the turbulent structure of the plume could be developed by treating the electron density and collision frequency as fluid marker properties which are convected about under the influence of a turbulent field in which the displacement from a mean position is a Guassian random variable. According to one form of the central limit theorem, we can produce a Gaussian random variable by constructing a set of realizations in physical space based on a Fourier representation whose power spectrum is well-behaved and whose phases are a set of random numbers uniformly distributed between 0 and 2π. We have adopted this approach.

The turbulent field displaces fluid with certain assigned properties from the expectation value of its position $\langle\vec{x}\rangle$ to a displaced position $\langle\vec{x}\rangle + \vec{D}(\vec{x},t)$. The turbulent

*Such as interface slope, which is important to establishing the mechanism of entrainment.

displacement $\vec{D}$ is the path integral of the turbulent velocity $\vec{u}(\vec{x},t)$:

$$\vec{D} = \int_0^t \vec{u}\, dt \qquad (5\text{-}1)$$

We can write this in terms of the time derivative of $\vec{D}$ as

$$\vec{u} = \frac{d\vec{D}}{dt} \qquad (5\text{-}2)$$

where the derivative is a substantive derivative (following fluid elements): $\frac{d}{dt} = \frac{\partial}{\partial t} + \vec{u}\cdot\nabla$.

The remainder of this section is concerned with developing a model for the turbulent displacement $\vec{D}$. In the interests of computational tractability, a number of simplifying approximations have been introduced. Most of these are justified by approximate physical arguments rather than by rigorous derivations. We have attempted to retain certain features which could be important, including the possibility of correlations between displacements which exist at different axial locations in the plume. We do this by considering the power spectrum of the velocity and displacement fields to evolve as fluid is convected downstream by the mean flow, and by assigning a set of frequencies to the Fourier modes representing the displacement.

The evolution of the spectrum presents an immediate problem. In principle, we could set up and solve a transport equation for the spectrum as a function of position.* In practice this turns out to be difficult, and we adopt instead a procedure in which the local spectrum is determined by some overall fluid properties at a given value of axial distance Z. On the basis that the turbulent region in the plume is somewhat like a self-preserving mixing layer between fluids of different velocities, we expect the turbulent velocity spectrum to evolve with distance downstream as follows: Shortly downstream from the origin, the mixing region dimension is small, so that the lowest wavenumber k_o of the velocity or displacement spectrum is large. (This wavenumber is inversely proportional to the outer or integral scale of the turbulence; the relation is derived in Appendix II.) As the mixing layer grows, the cutoff wavenumber decreases; since the maximum scale increases linearly with z, we should expect to find k_o decreasing as z^{-1}. However, if the mixing region is self-preserving, the turbulent intensity must be the same at all stations, so that the area under the curve representing the turbulent spectrum must be constant. Thus, the spectrum should evolve

*Here we would consider the power spectrum to represent spatial and temporal scales small with respect to the distance over which the spectrum changes appreciably.

as shown in Figure 19. Close to the origin the spectrum is made up of small, highly energetic eddies, while farther downstream the eddies become progressively larger, but less energetic. The turbulent displacement cannot exceed a scale proportional to the mixing layer dimension, so that there must exist a minimum wavenumber k_o at which the spectrum either cuts off or saturates.

Each spatial Fourier component of the displacement will have a correlation time inversely proportional to its frequency, or an axial correlation length proportional to U/ω_k, where U is the downstream convective velocity. Strong correlations should exist for $\Delta Z\ \omega_k/U << 1$, while essentially no correlations should exist for $\Delta Z\ \omega_k/U >> 1$. We should expect some effects on the signal if the turbulent structure at successive phase screens is correlated. To allow for this, we assign a frequency to each of the Fourier modes and allow the phases of the modes to change as $\omega_k t$.

The evolution of the displacement with axial distance is evaluated as follows: Suppose that all axial (i.e., z-direction) velocities are equal at every point on an x-y plane and that they are much larger than all perpendicular velocities. Under these conditions we can define a time t' measured by an observer moving downstream with the flow, such that $\frac{\partial}{\partial t'} = \frac{\partial}{\partial t} + U \frac{\partial}{\partial z}$. If we also assume that we can

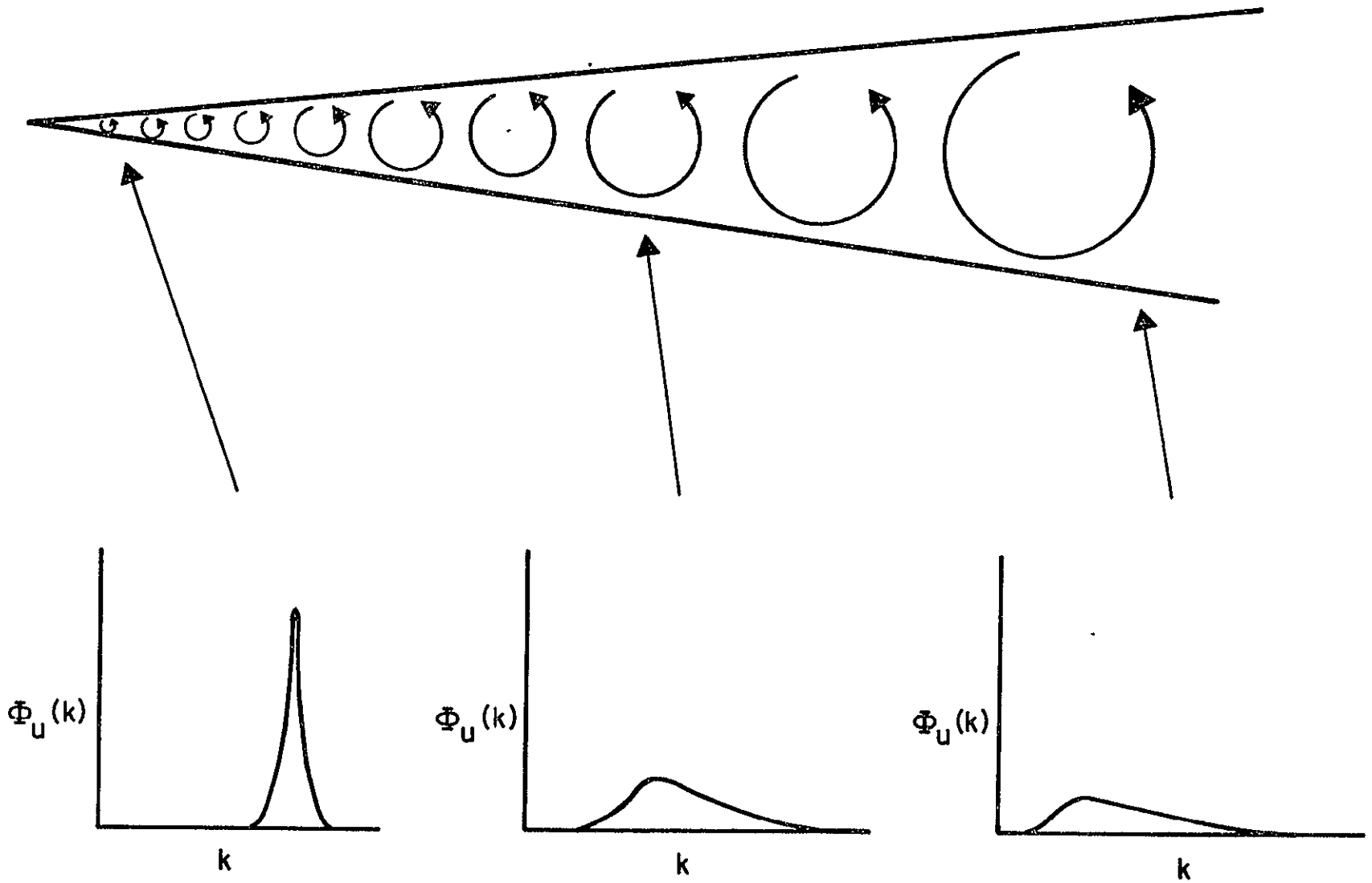

Figure 19. Evolution of the power spectrum of velocity fluctuations in a turbulent mixing layer.

neglect the convective terms involving the horizontal velocities (a reasonable assumption if the mean axial velocity is large with respect to lateral turbulent velocities), then we can replace the total derivative in Equation (5-2) by a partial derivative, and write

$$\vec{u}' = \frac{\partial \vec{D}}{\partial t'} \quad . \tag{5-3}$$

The space-time Fourier transform of this is

$$\vec{D}_k = \frac{\vec{u}_k}{\omega_k} \tag{5-4}$$

where ω_k is the frequency of the displacement Fourier component $\vec{D}_k$.

We now return to the concept that an eddy overturning time (its period, τ) is its circumference divided by its velocity, or

$$\tau \approx \pi\lambda/u \tag{5-5}$$

In terms of wavenumber and frequency,

$$\omega \approx k\ u_k\ (a\pi)^{-1}$$

where a is a constant of order unity. Thus the displacement Fourier components are

$$\vec{D}_k \approx \hat{k}\ (a\pi)\ k^{-1} \tag{5-6}$$

where $\hat{k}$ is a unit vector in k-space. In practice, we construct $\vec{D}(\vec{x})$ as a discrete Fourier series. The squared amplitudes in these series represent the contribution to the total power of the displacement field from a range of wavenumbers between $\vec{k}$ and $\vec{k} + \Delta\vec{k}$. Thus the discrete values of the amplitudes of $\vec{D}_k$ are

$$|\vec{D}_k| = \hat{k}\ (a\pi)\ k^{-2}\ (\Delta k_x\ \Delta k_y)^{\frac{1}{2}} \tag{5-7}$$

where Δk_x and Δk_y are determined by the grid dimensions. We now have an expression for the Fourier components of the turbulent displacement and an expression for their frequency. Using these expressions we can construct a realization of the turbulent displacement field and advance it in time (or alternatively in z) as it moves down the plume.

We expect the three-dimensional turbulent velocity spectrum $\Phi_u(k)$ to obey the Kolmogorov $k^{-11/3}$ law in the inertial range and to have a low-wavenumber cutoff or saturation corresponding to the largest eddy size (of order of the lateral dimensions of the turbulent region);

the dissipation scale is well below any scale we must consider. A reasonable expression for the turbulent velocity spectrum is

$$\Phi_u(k) = c(k_o^2 + k^2)^{-11/6} \tag{5-8}$$

where the long-wave saturation wavenumber k_o is expected to be a steadily decreasing function of time. The constant c is chosen by requiring that the mean square turbulent velocity $\langle u'^2 \rangle$ be obtained when the spectrum is integrated over all wavenumbers. Thus

$$c = \langle u'^2 \rangle / \int_o^\infty \Phi_u(k)\, dk \tag{5-9}$$

or explicitly,

$$c = \frac{\Gamma(11/6)\ k_o^{2/3}\ \langle u'^2 \rangle}{2\pi\ \Gamma(3/2)\ \Gamma(1/3)} = 0.512\ k_o^{2/3}\ \langle u'^2 \rangle \tag{5-10}$$

A computational procedure for evaluating realizations of the turbulent flow field compatible with the arguments given above is the following: At the beginning of each separate propagation calculation, a realization of the turbulent displacement field in Fourier space is calculated by assigning amplitudes, phases, and frequencies to a set

of modes. We assign N modes to each wavenumber $\vec{k}$; each of these N modes has a different assigned frequency. The mode amplitudes of the x components of the displacement are

$$D_x^o(k_x, k_y, \omega_{ki}) = k_x[\Delta k_x \Delta k_y]^{\frac{1}{2}} a\pi(Nk^3)^{-1} \times \exp(2\pi i R) \quad (5\text{-}11)$$

where R is a random number uniform in the interval (0,1). The y components are evaluated from a similar expression. The frequencies of these modes are evaluated from the velocity spectrum as follows: We first calculate an expectation value of the velocity at a given wavenumber as

$$\langle u_k \rangle = [\Phi_u(k)\ k\ \Delta k_x\ \Delta k_y]^{\frac{1}{2}} \quad (5\text{-}12)$$

where Φ_u is the three-dimensional velocity spectrum, Equation (5-8). The expectation value of the frequency is then

$$\langle \omega_k \rangle = k\langle u_k \rangle / a\pi \quad . \quad (5\text{-}13)$$

The frequencies of the N individual modes at a given wavenumber are assigned by sampling from a Gaussian distribution. Explicitly, the relation used is

$$\omega_{k,i} = \langle\omega_k\rangle \; [1 + R] \qquad (5\text{-}14)$$

where R is a Gaussian-distributed random number having zero mean and unit variance.

We have not yet taken account of the long-wavelength saturation of the displacement spectrum. The saturation wavenumber k_o is inversely proportional to the integral scale of turbulence, L_T, which we expect to be roughly proportional to the width of the mixing region. From explicit calculations using a set of turbulence model equations (supplied by Lockheed), we deduce that $L_T \approx 0.05\ L_{mix}$, where L_{mix} is the width of the mixing layer. Thus at each station we can set

$$k_o = 0.75/L_T \quad . \qquad (5\text{-}15)$$

This results in a scale for the large eddies $(2\pi/k_o)$ of the order of 50% of the mixing layer width, which appears reasonable. The saturation factor is simply applied to the spectrum at each station; in addition, a phase factor containing the frequency is also applied. Thus,

$$D_x(k_x, k_y, \omega_{ik}; z) = D_x^o(k_x, k_y, \omega_{ik}) \; \frac{k^3}{[k_o^2(z)+k^2]^{3/2}} \; e^{i\,\omega_{ik}\,Z/U} \qquad (5\text{-}16)$$

and similarly for D_y. The total displacement component at a given value of k is the sum over the N modes:

$$D_x(k_x, k_y; z) = \sum_i D_x(k_x, k_y, \omega_{ik}; z) \quad . \qquad (5\text{-}17)$$

The resulting Fourier amplitudes are then subjected to an inverse fast Fourier transform which provides the displacements as functions of position in physical space. The electron density and collision frequency at a point (x,y) are assigned the values at the displaced positions $(x-D_x, y-D_y)$ in the reference flow field calculation. This reference flow field should be chosen such that the expectation values of the electron density and collision frequency, averaged over an ensemble of realizations of the turbulent displacement field, are the local values predicted by the mean flow calculation. In general, this will mean that the reference flow field will be different from the computed mean flow: only in special circumstances will the average over all turbulent displacements be equal to the local value.

If the probability that the turbulent displacement is between $\vec{D}$ and $\vec{D} + d\vec{D}$ is $P(\vec{D})\, d\vec{D}$, then the mean electron density is

$$\langle N_e(\vec{x}) \rangle = \int N_e^{(r)} (\vec{x}-\vec{D})\, P(\vec{D})\, d^2\vec{D} \qquad (5\text{-}18)$$

where $N_e^{(r)}(\vec{x})$ is the electron density of the unknown reference flow and where we have assumed that $P(\vec{D})$ is normalized to unity. Since this has the form of a two-dimensional convolution, we can write the Fourier transform of $\langle N_e \rangle$ as

$$\langle N_e(\vec{k}) \rangle = N_e^{(r)}(\vec{k})\, P(\vec{k}) \tag{5-19}$$

and thus the Fourier transform of the reference field is

$$N_e^{(r)}(\vec{k}) = \langle N_e(\vec{k}) \rangle / P(\vec{k}) \quad . \tag{5-20}$$

Thus if we know $P(\vec{D})$, we can in principle find the reference electron density field by transforming the given mean field, dividing by the transform of $P(\vec{x})$, and then performing an inverse transform on the result.

It is known that such deconvolutions are often unsuccessful as the result of numerical noise, which results in the introduction of spuriously large values at some wavenumbers for the reference field (those where $P(\vec{k})$ is small). In addition, test calculations indicate that the convolution has only a small effect upon electron density profiles unless $\langle D^2 \rangle$ is a significant fraction of the profile width. For these reasons we have neglected the convolution error in our turbulence calculation, with the result that our reference field--the mean field--is somewhat

more extensive than it should be. Matched filter deconvolution techniques are capable in principle of compensating for noise errors, at the cost of some errors in localization. These remain a subject for investigation in future work.

Because the grid of the propagation changes in scale as the calculation proceeds as a result of applying Talanov's tranformation, we carry out the calculation of $\vec{D}(\vec{x})$ in physical space on a constant reference grid. This grid is chosen to be identical to the computational grid at the station where the plume subtends its greatest angle with respect to the roll axis. Values of the electron density and collision frequency are first calculated on this reference grid and then interpolated to the grid of the propagation calculation. Our calculation evaluates a displacement everywhere in this reference grid, including the potential flow outside the plume. We could avoid this either by imposing a damping factor on the displacement at some distance from the mixing region or (possibly) by introducing a phase coherence in $\vec{D}(\vec{k})$ which would limit $\vec{D}(\vec{x})$ to the mixing region by phase cancellation elsewhere. On the other hand, the electron density outside the plume is essentially zero, and convection of it produces no net effect unless it is convected into the plume. We therefore simply allow $\vec{D}(\vec{x})$ to be evaluated on the entire grid.

An example of the effects introduced by this procedure is shown in Figure 20. The contour plots on the top show the imaginary part of the refractive index for the mean flow (in this case for two superimposed plumes) at a given axial station; the plots on the bottom show the index contours resulting from applying a turbulent displacement. The resulting irregularity is clearly apparent, and appears to be of reasonable size in relation to the overall plume size. Note the sharpness of the edge of the plume as evidenced by the close spacing of the lower contours (two plots at right).

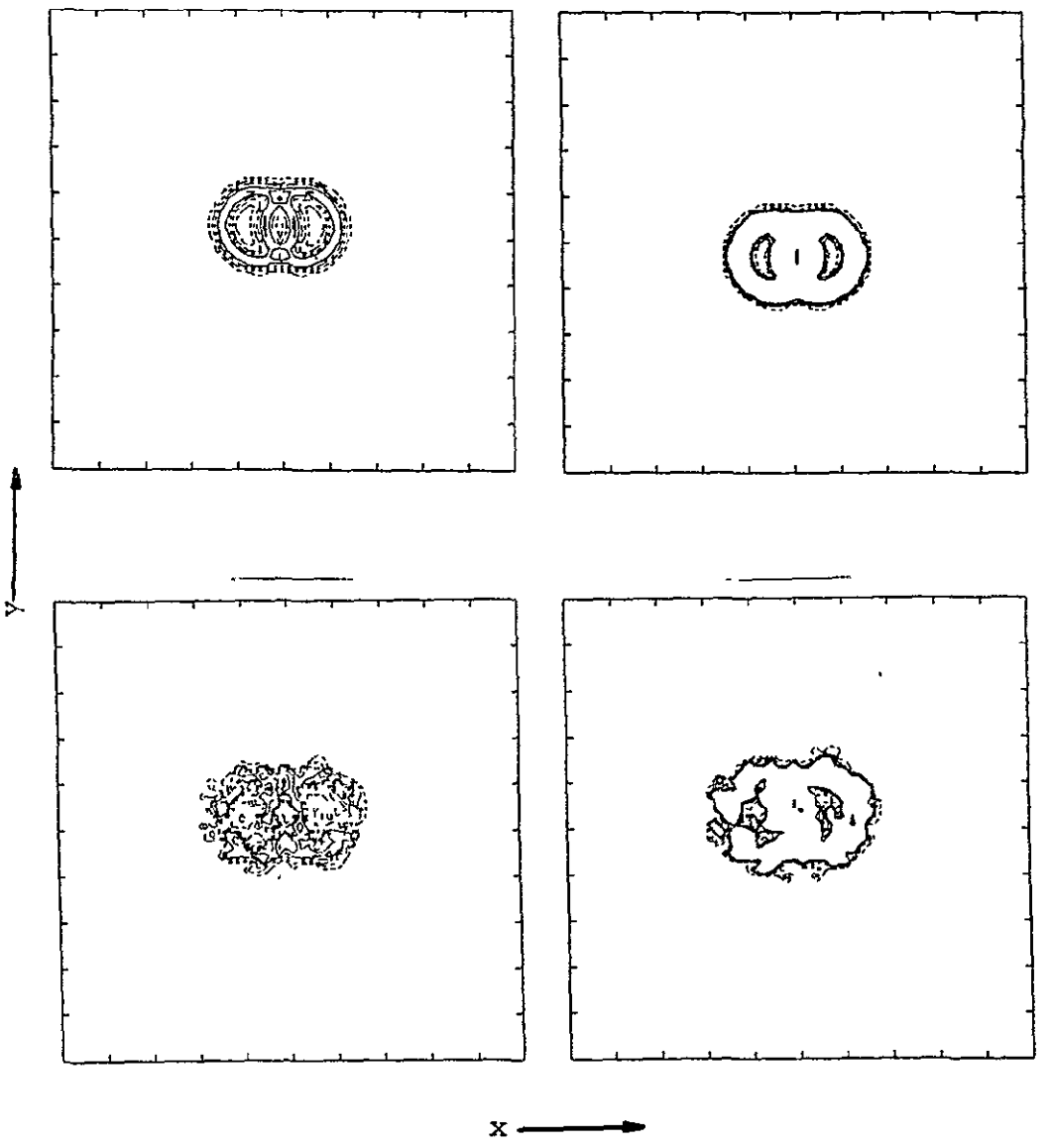

Figure 20. Contours of the imaginary part of the refractive index in turbulent and non-turbulent exhuast plumes (turbulent beneath) of a Titan III-C at 20 km altitude. Left plots show higher contour levels. In each plot, dashed contours are lower.

6.0 DEMONSTRATION AND COMPARISON WITH EXPERIMENT

We have applied these procedures to the exhaust plumes of the Titan III-C and the Space Shuttle. In each case we calculate the signal pattern from the antenna to the ground, and employ reciprocity to identify the signal strength as that resulting at the antenna due to transmission from a ground station. Because the near field antenna pattern is not available, we have assumed that the antenna is an isotropic radiator. No blocking by the vehicle is assumed except in the plane of the vehicle base. The signals that we calculate on the side of the vehicle away from the antenna are therefore not to be trusted.

Because some attenuation data are available for the Titan III-C, we can compare our predictions with experiment in that case. The quality of agreement between theory and experiment (keeping in mind the condition of the data) should provide an indication of the error bounds to be placed on our calculations for the Space Shuttle. We also have used the Titan III-C as a test case for some of the procedures we employ to represent the turbulent, three-dimensional exhaust plume using the axially symmetric, time-averaged flow field.

6.1 Signal Interference Effects

It will be helpful, and illustrative of several features of the plume-signal interference phenomenology, to follow the progress of the calculation through an example: These calculations are for a Titan III-C plume at 36 km. The signal frequency is S-band and the two-engine plume is treated as a single merged plume from an equivalent single engine. We begin at a z station near that at which the plume subtends the maximum angle as seen from the antenna location. Figure 21 shows a computer-generated contour plot of the field amplitude $|\psi|$ in a plane normal to a line drawn aft from the antenna parallel to the vehicle roll axis (and to the plume axis). The plume axis is not identical with the origin of the plot because the antenna is one side of the vehicle (the left in this case.) The contours are uniformly spaced on a linear scale. The lower three levels are dotted, while the upper three are solid lines. A maximum occurs between the two complete outer circles, while the "islands" outside them are a secondary maximum. Small irregularities in the contours are the effects of interpolation of the flow field data to a rectangular grid, combined with offset of the antenna. The contours at the top are values of $|\psi|/|\psi_o|$, where ψ_o is the field at the nozzle exit.

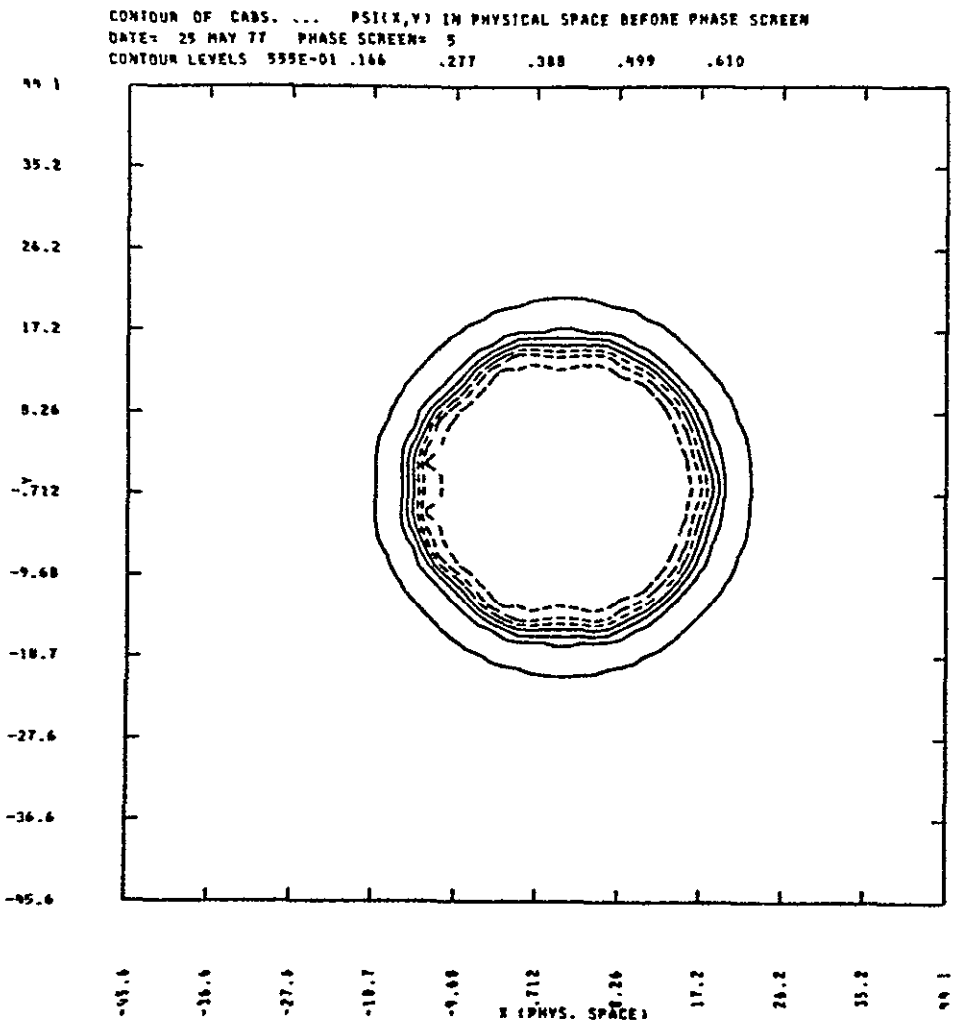

Figure 21. Contour plot of the value of $|\psi|$ incident upon a plume station. Coordinates are in meters, and contours in values of $|\psi|/|\psi_o|$.

Even at this station, about 10 meters downstream from the engine, the field is very strongly attenuated near the plume centerline.

Figure 22 shows a plot of the imaginary part of the plume's refractive index in the same plane. Comparison of this figure with the previous figure shows that the region of the field in which the amplitude is appreciable lies mostly outside the plume. The attenuation at the lowest contour level is approximately 4 db/meter. The result of subjecting the incident field to passage through this phase screen is shown in Figure 23. (The screen thickness is about 2 meters.) The values of $|\psi|$ are shown for the same levels as in Figure 21. Little has happened to the external field, but that at the edges of the plume has been absorbed, as evidenced by the greater displacement of the low contours from the plume axis.

The behavior of the calculation at the other stations is roughly similar. Figure 24 shows the values of the field amplitude just after the last phase screen included in this calculation. Some diffraction has evidently occurred, since the higher contours are more spread out than before. The field strength is lower as a result of geometric spreading; note the larger values of x and y. The region of appreciable phase change (Figure 25) occupies only a

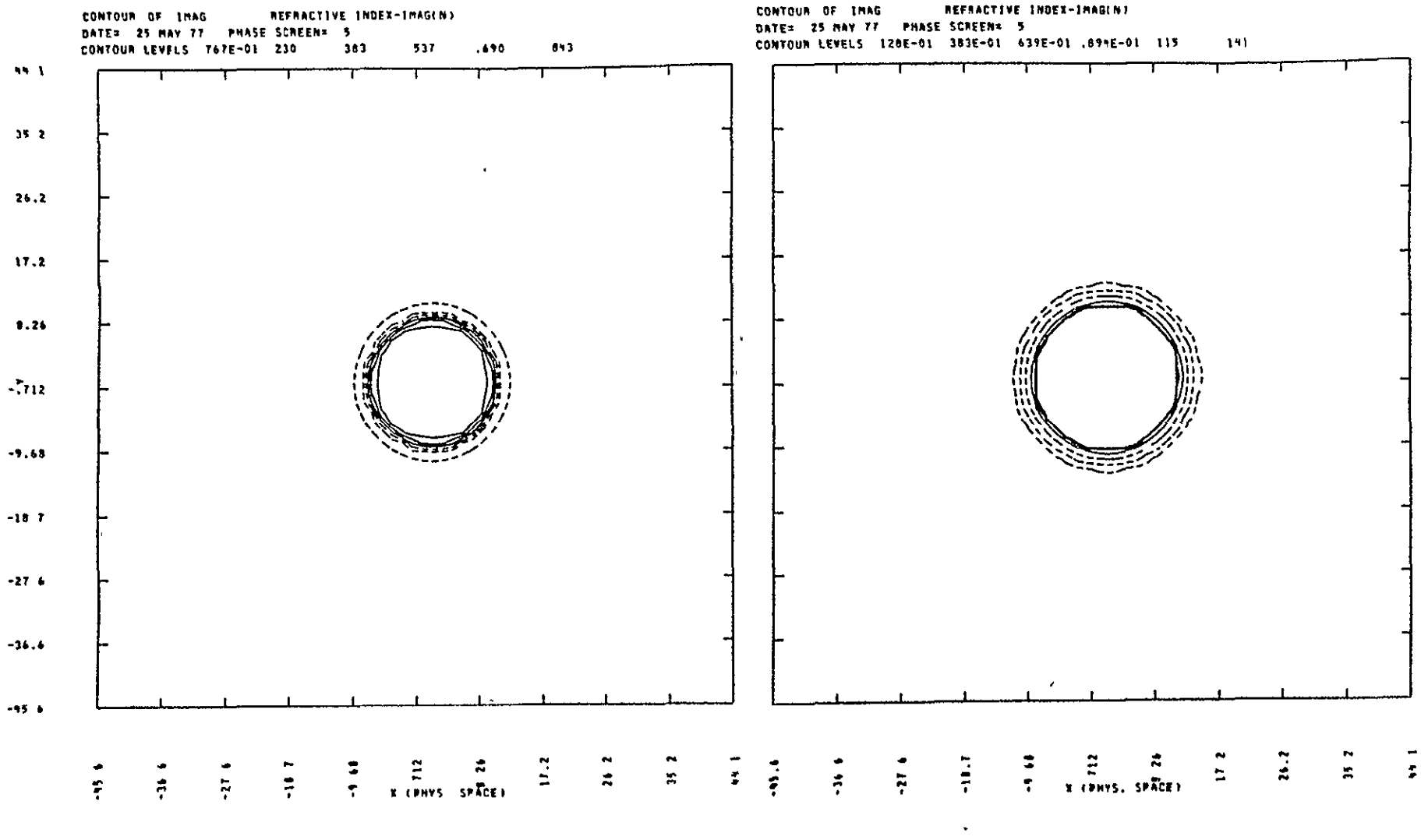

Figure 22. Contours of the imaginary part of the refractive index (high at left, low at right) at the axial station of Figure 21.

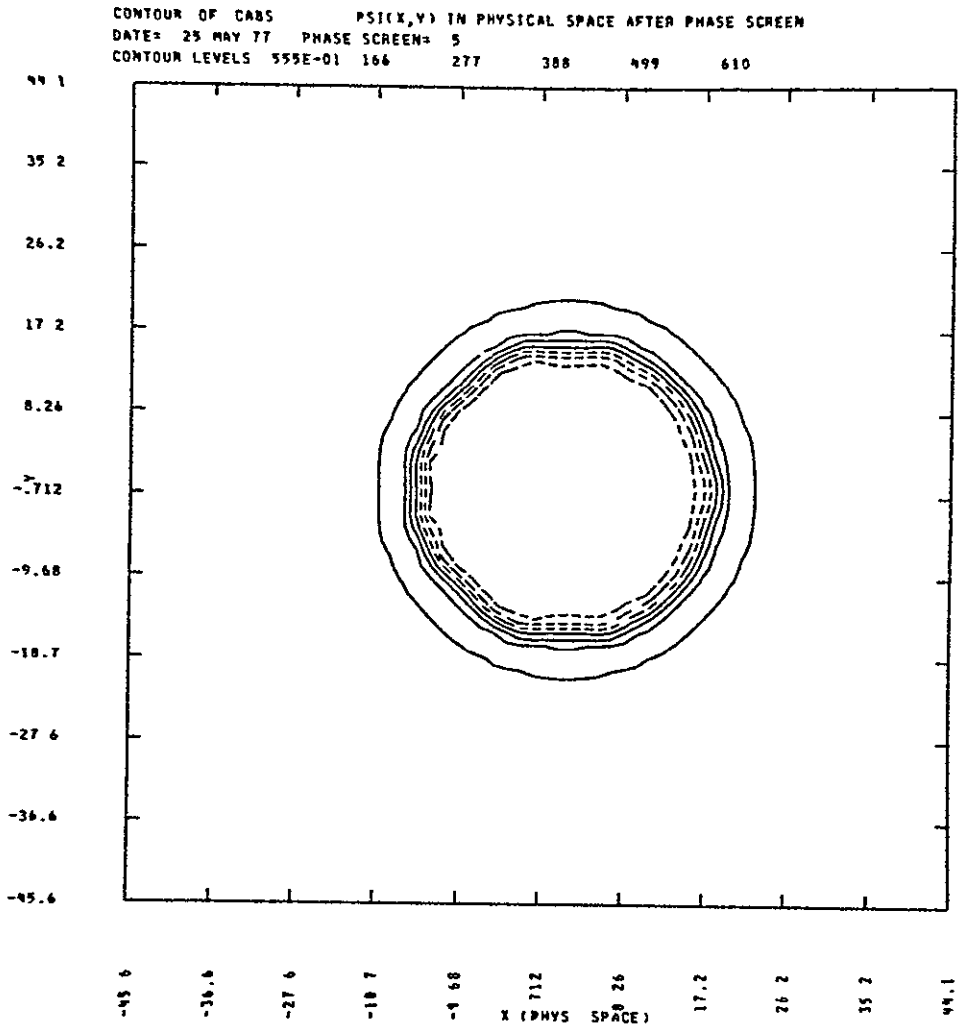

Figure 23. Contours of constant field amplitude after emerging from the phase screen represented by the previous figure.

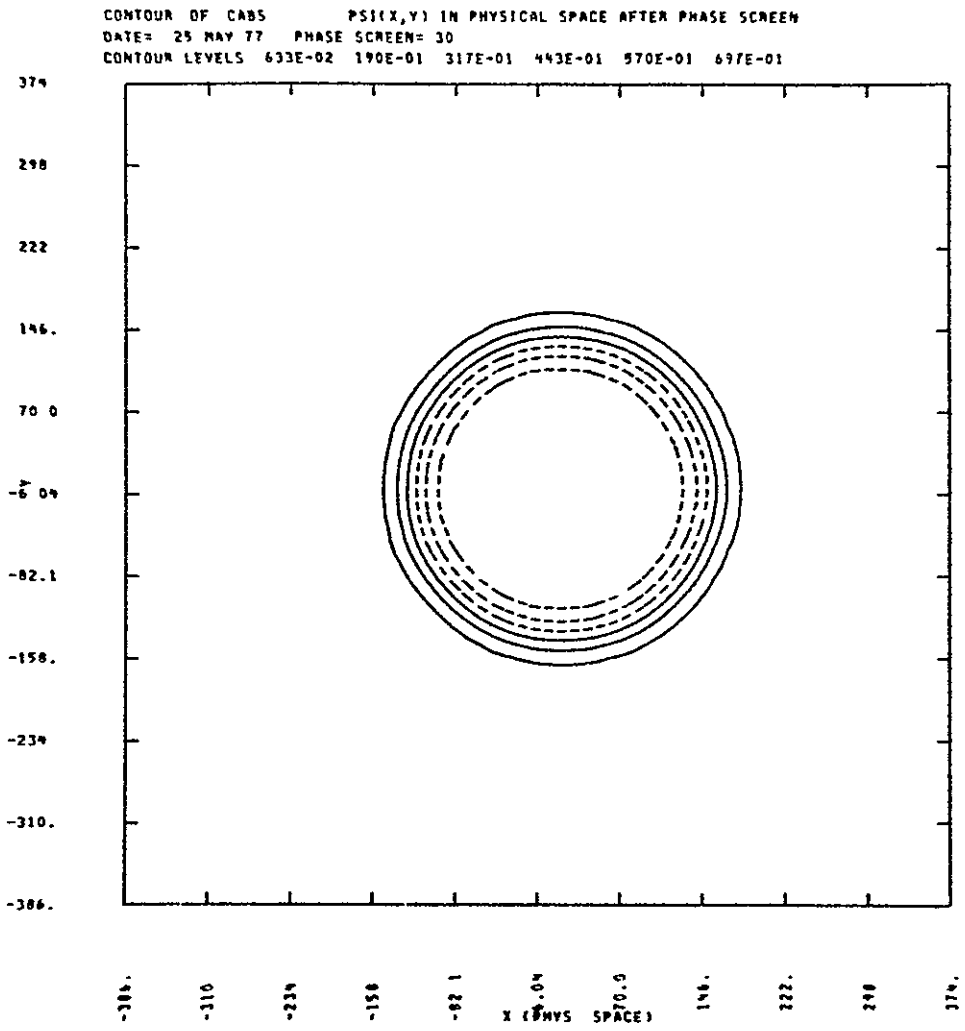

Figure 24. Contours of constant field amplitude just after the last phase-changing screen.

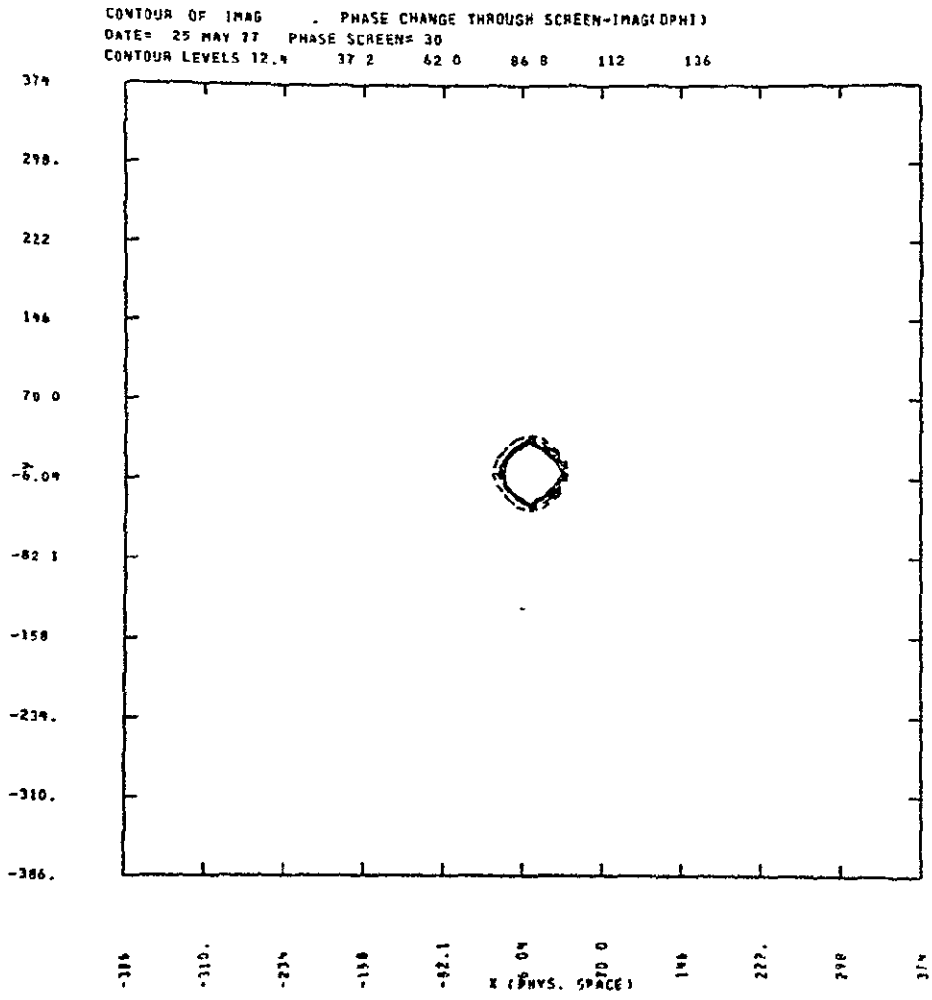

Figure 25. Contours of the imaginary part of the phase change (attenuation exponent) in the last phase screen considered.

very small portion of the grid at this station; this is a consequence of the plume's spreading less rapidly than the mesh, which grows in accordance with geometric optics under the rules of the Talanov transformation.

Finally, Figure 26 shows intensity contours in a far-field plane (in this case, 50 km behind the vehicle). The intensity is normalized with respect to the uniform free-space intensity, and the contour levels are in db (volts). The abscissa and ordinate are angles in the x and y direction, in degrees. The angular resolution of this calculation is about 1.3 degrees. The intensity is given at each of 4096 points in this grid. Figures 27 and 28 show the intensity ratio in db along the $\theta_y = 0$ and $\theta_x = 0$ axes of the previous figure. Only the $\theta_x = 0$ cut is symmetric; this is a result of the initial offset of the plume axis from the nominal propagation axis in the x direction. The maximum attenuation level is about 90 db.

We have performed a few elementary variations about this basic type of calculation illustrating the importance of the various elements of the calculation. When the electron density at every point in the plume is doubled, the results are very little different from the nominal case. This indicates the relative unimportance of conditions

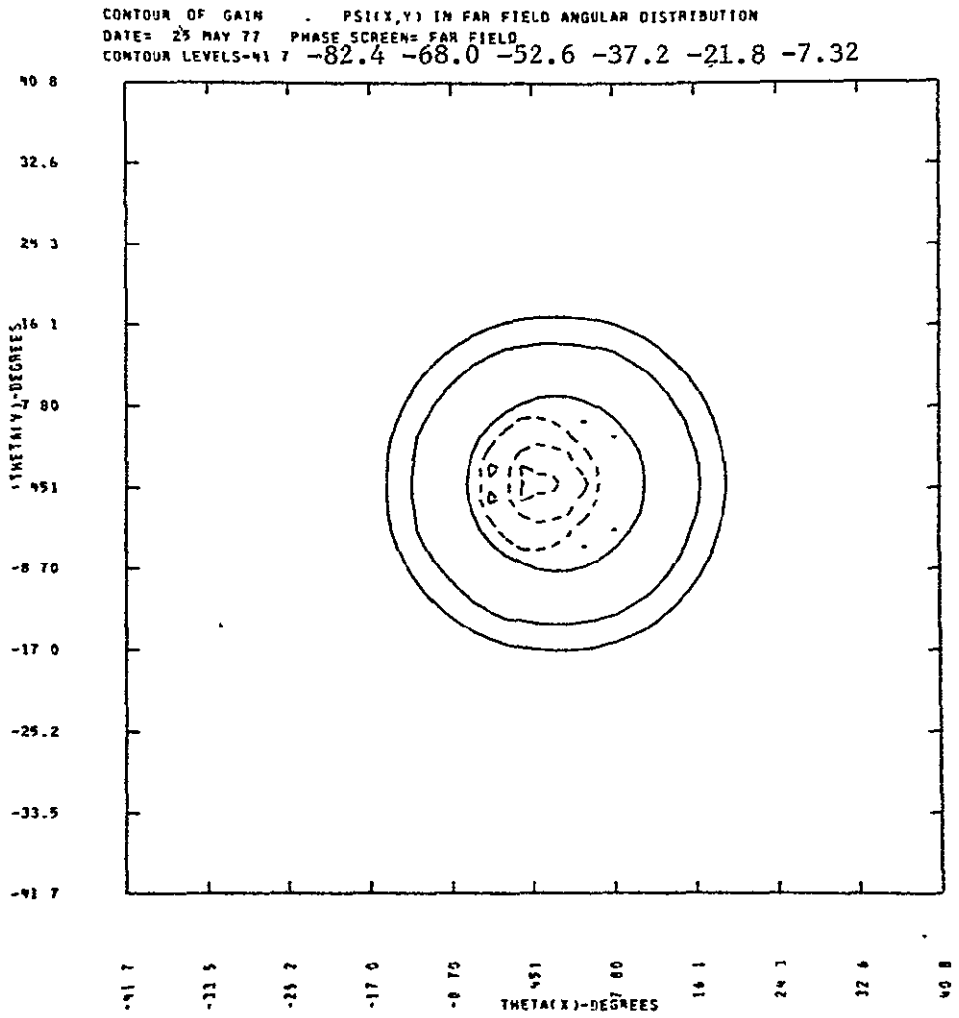

Figure 26. Contours of constant normalized field intensity (in db) in the far field (Titan III-C at 36 km).

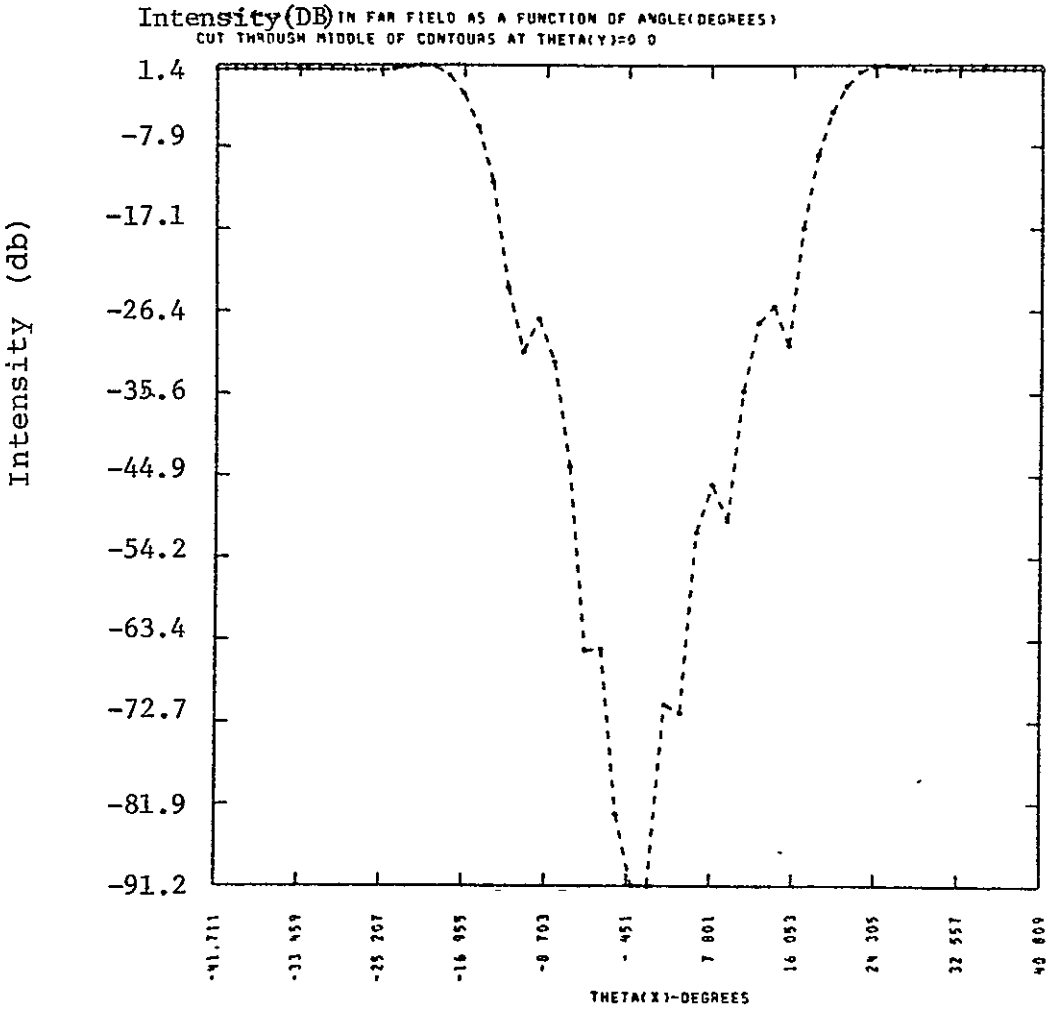

Figure 27. Far-field intensity as a function of aspect angle θ_x (normal to motor plane) for $\theta_y = 0$.

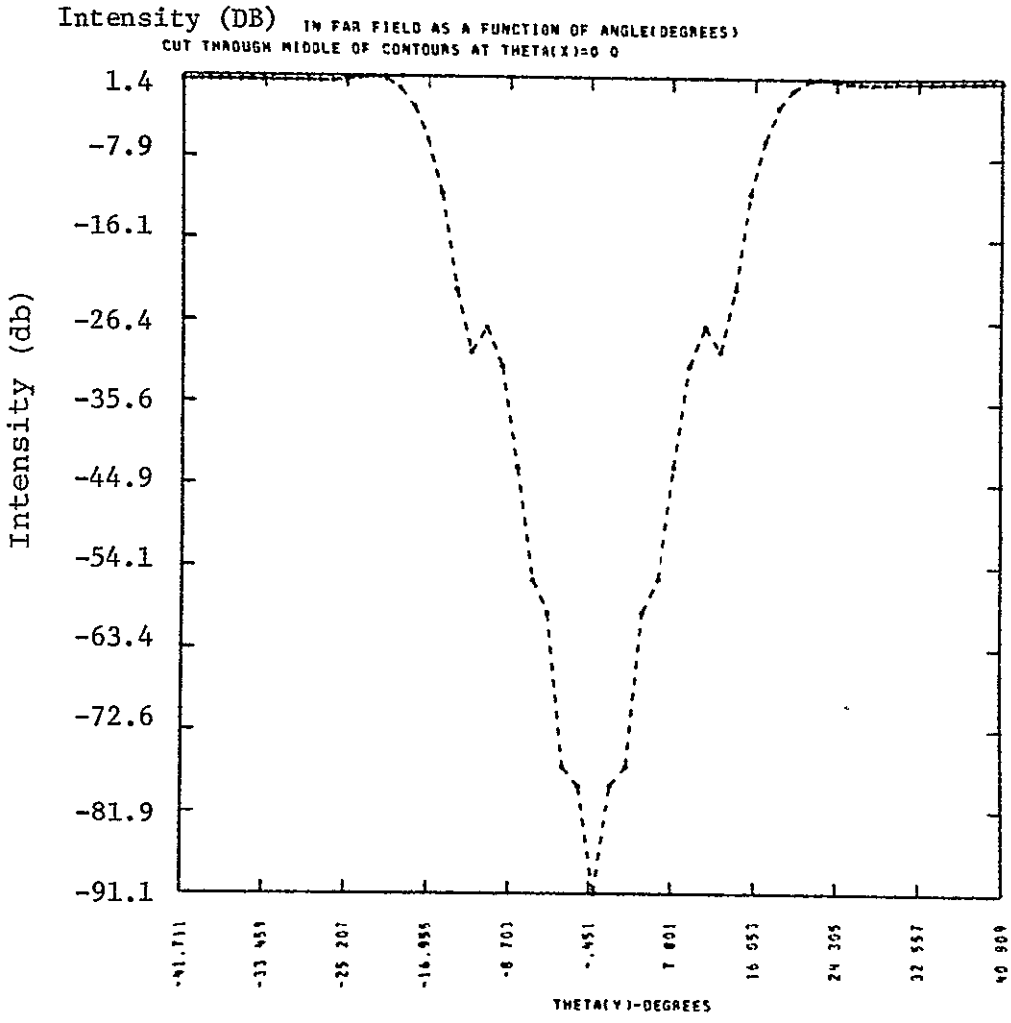

Figure 28. Far-field intensity as a function of aspect angle θ_y (in motor plane) for $\theta_x = 0$.

within the plume when the absorption is high. It also depends upon the relative steepness of the electron density gradients near the edge of the plume; if these are sharp, then even a substantial change in the value of n_e will not produce much change in the position of the plume edge, the extent of the shadowed region, and the diffraction pattern around it. However, if we increase the dimensions of the plume by a modest fraction (say 10-20%), the attenuation pattern in the far field becomes appreciably wider and deeper. These trial calculations indicate that simple geometric blockage by the plume is the predominant effect.

The irrelevance of internal plume properties to the signal is again illustrated by Figure 29. This shows the signal attenuation per unit length expected in a Titan III-C plume at 36 km altitude as a function of radial distance at the axial station shown in Figures 21-23 at P-band and S-band frequencies. The dots are the actual points from the flow field calculation. Note that although the S-band signal is less attenuated than the P-band signal in the outer region of the plume, the difference is essentially irrelevant. The attenuation levels of interest are less than 1 db/meter, and these low levels are attained only at the plume edge. Note also that the effective S-band plume at those attenuation levels is not much less wide than the P-band plume.

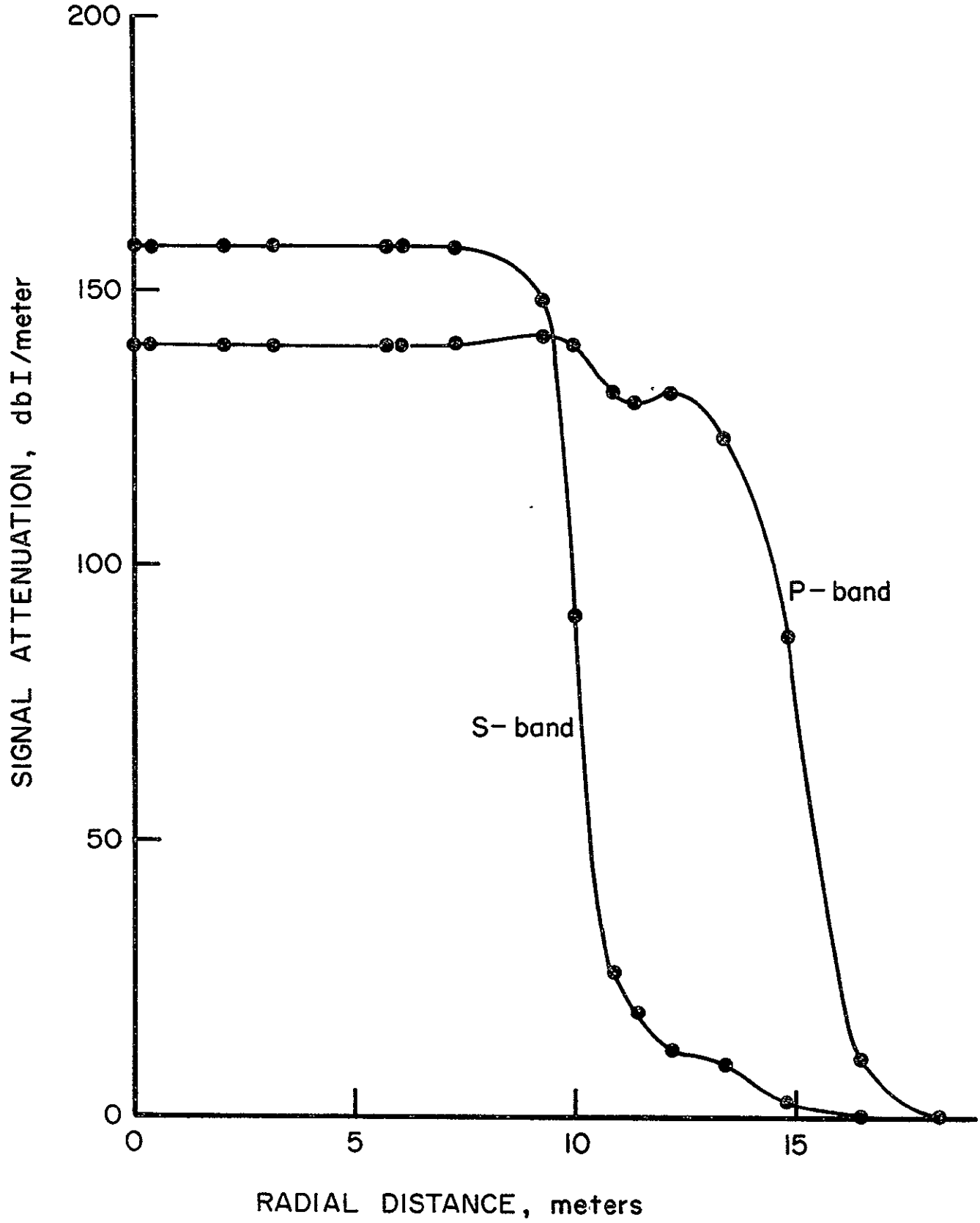

Figure 29. Attenuation as a function of radial distance at a station near maximum plume blockage in the exhaust plume of a Titan III-C at 36 km altitude.

Figure 30 shows the geometry of the plume and the far-field signal in schematic fashion. The plume is here represented by the actual set of phase screens used in the calculation (excluding some far downstream which have no effect). Each perpendicular line from the abscissa represents a phase screen; the edge is at the 1 db/meter attenuation level. The dashed line angled upwards from the antenna represents the edge of the shadowed region (umbra). The amplitude of the far-field signal is shown at right, as a function of aspect angle. The geometric terminator passes along the edge of the plume for an appreciable distance. Multiple scattering at several axial stations undoubtedly has some influence on the result. The dominant effects of geometry upon the signal are clearly shown.

Introducing simulated turbulence into this calculation has a noticeable effect upon the behavior of the plume and signal at intermediate stages, and a less significant effect in the far field. The plume is essentially sharp-edged on the grid scale, and the predominant effect of turbulence is to distort the edges of the plume. Figure 31 shows the resulting signal at a station in the plume for a specific realization of the turbulent displacement. (Compare this figure with Figures 21-23.) The incoming field is shown at left, and the outgoing at right. It appears that the turbulence at this station has to some

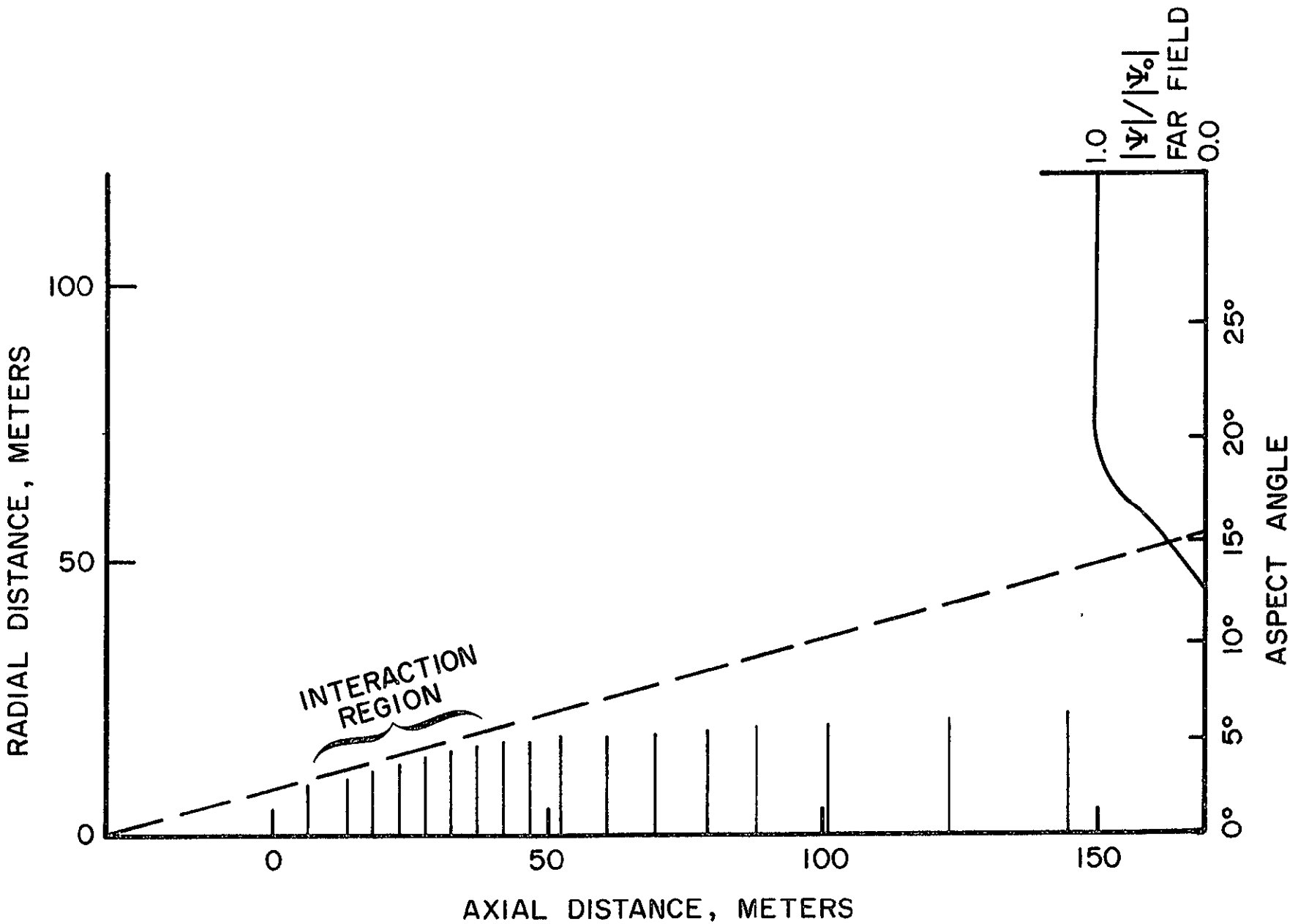

Figure 30. Plume-signal interaction geometry. Plot at right shows normalized field amplitude as a function of aspect angle (S-band).

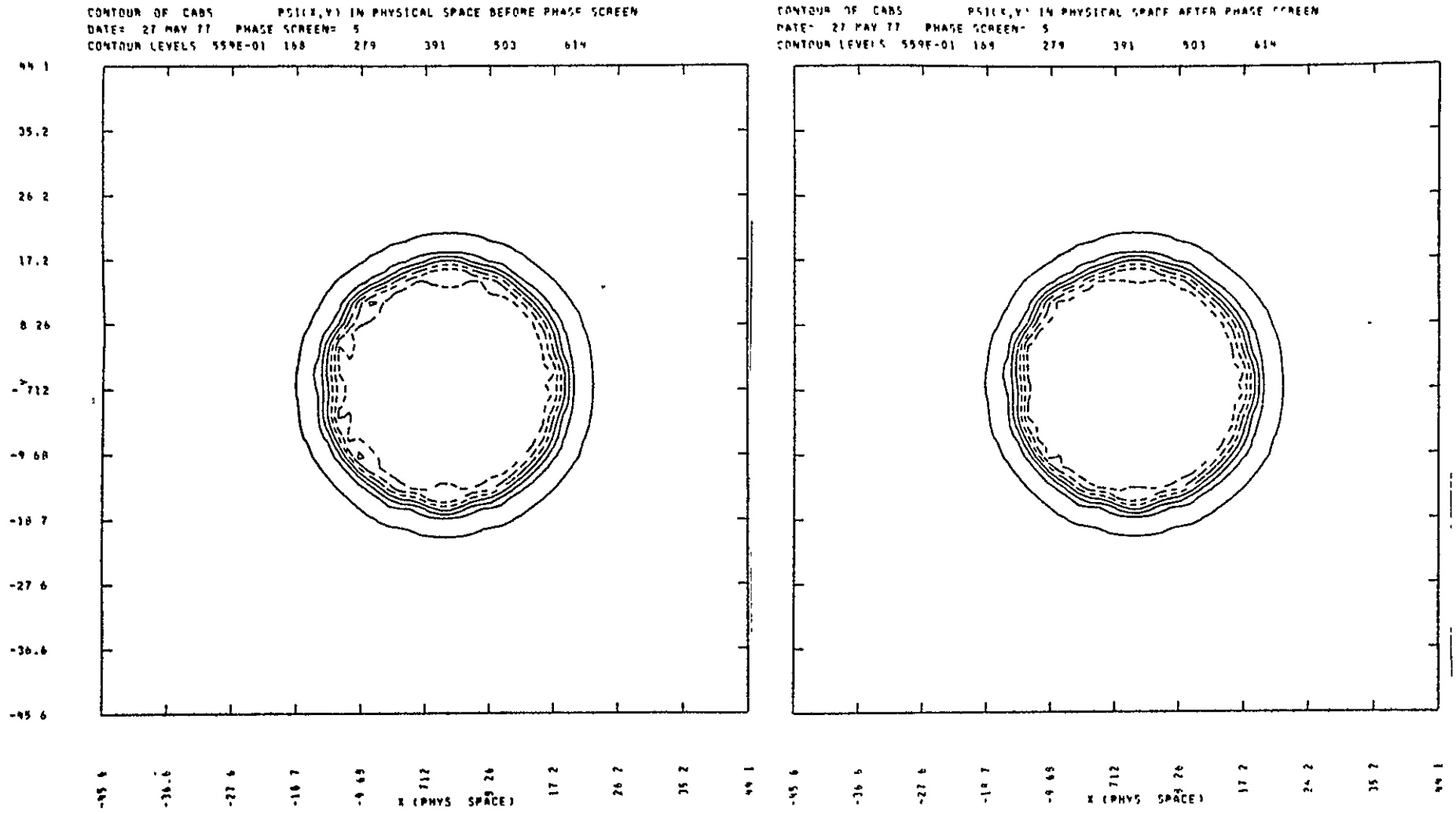

Figure 31. Incident (left) and emergent (right) fields at an axial station (cf. Figures 21-23) in a turbulent Titan III-C plume (individual realization) at 36 km altitude.

extent counteracted the effects which occur at earlier stations, and made the field a bit smoother. One might expect this behavior if the structure decorrelates quickly with axial distance (or convected time).

Figure 32 shows the effects of simulated plume turbulence on the far-field signal. Here we show several plots of field intensity versus aspect angle in the plume of the two solid motors for the Titan III-C. (These plots would be symmetric in the absence of any turbulent effects; the calculation is otherwise identical with that of Figure 28.) The abscissa is identical with that of Figure 28; the ordinate is computer-generated and varies slightly. Peak attenuation (essentially tail aspect) varies from about 80 to 90 db in these calculations. The introduction of simulated turbulence has not greatly affected the overall signal attenuation pattern, although several details (especially the position and shape of fringes) are affected. The variability in the predicted signal is greatest at tail aspect (standard deviations of 4-6 db) and generally decreases toward the edge of the shadowed region. No large signal dropouts are predicted by this model of propagation in (or better, around) a turbulent medium.

At lower altitudes the effects of turbulence are somewhat greater. Figure 33 shows a realization of the incident and emergent wave fields at an axial location

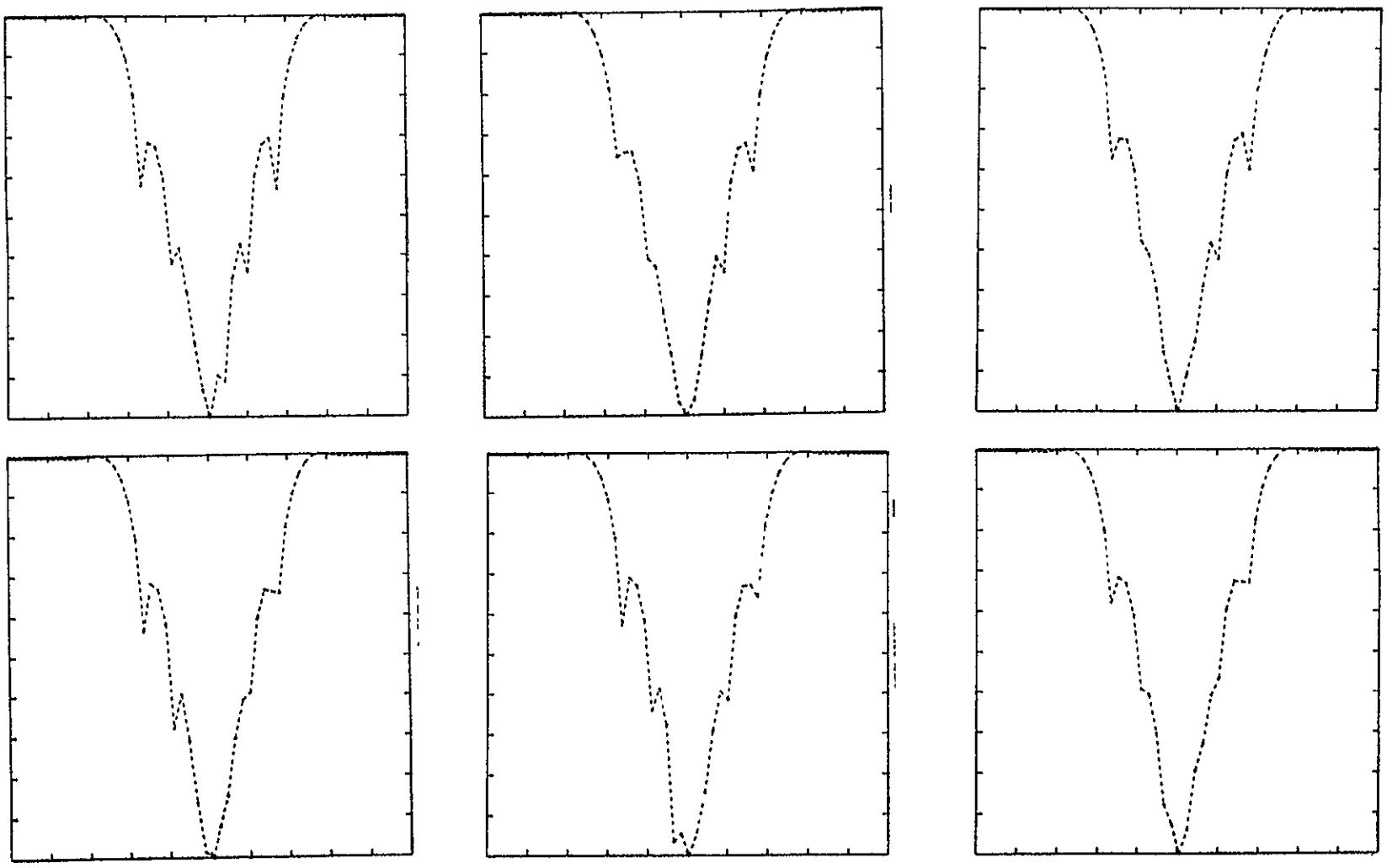

Figure 32. Plots of field intensity $|\psi|^2$ in db vs. aspect angle θ_y (in solid motor plane) for several individual realizations of simulated plume turbulence. Titan III-C at 36 km. Compare with Figure 28.

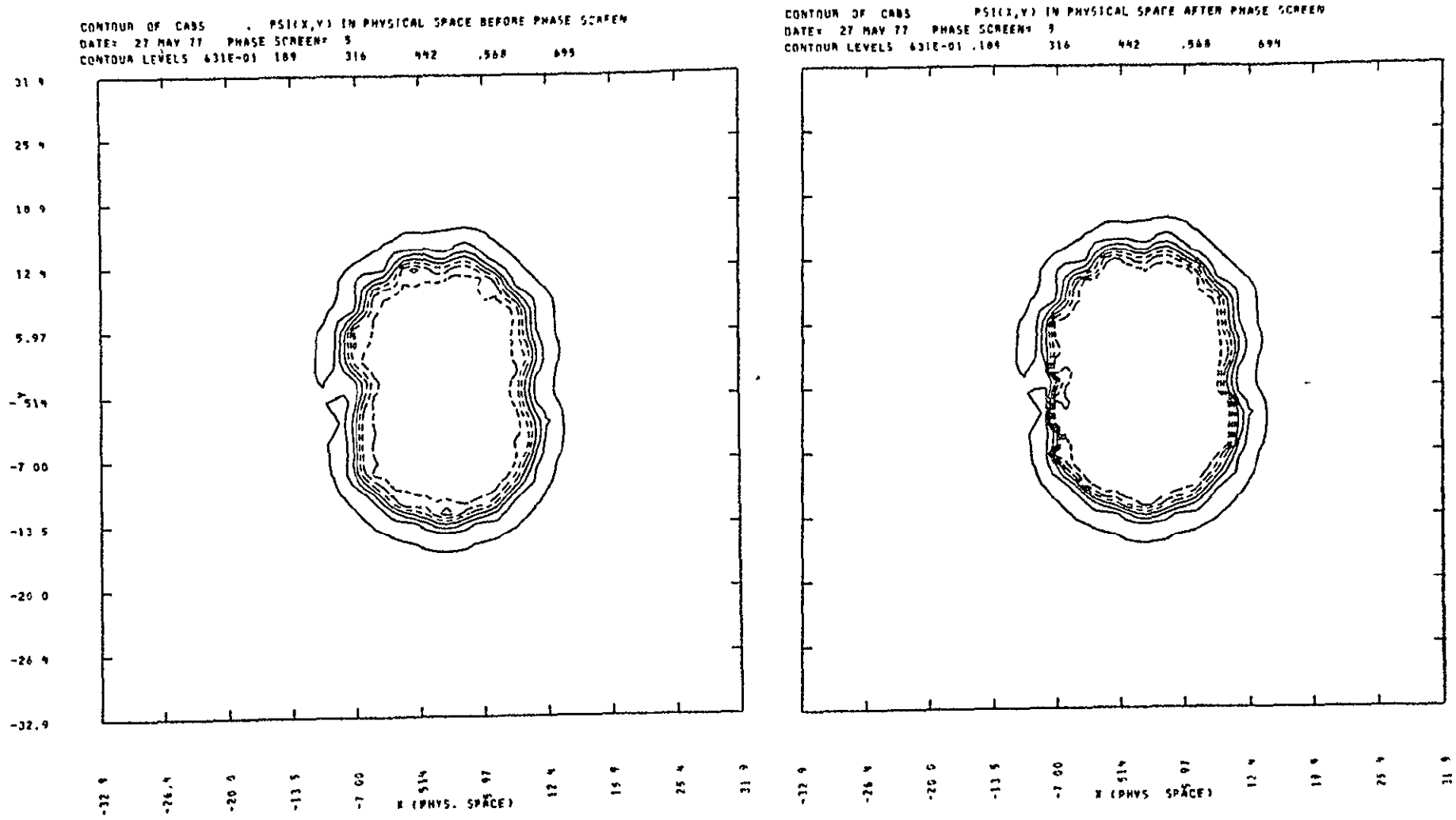

Figure 33. Incident (left) and emergent (right) field amplitudes at an axial station in a Titan III-C plume at 20.6 km altitude with simulated turbulence.

roughly equivalent to that of Figure 31 for the Titan III-C at 20.6 km, and Figure 34 shows the far-field amplitude variation for a set of realizations. (In these calculations we treat the flow field as a superposition of two independent plumes.) The attenuation for the mean flow is shown in Figure 35. Figure 33 indicates that the turbulent displacements are somewhat greater with respect to the plume outline at low altitude. This is probably a consequence of the mixing layer's representing a smaller fraction of the plume cross section at higher altitude, where a greater degree of inviscid expansion takes place. The tail aspect signal attenuation in these calculations varies between 88 and 102 db. Note that the effects of turbulence on the position and intensity of the secondary diffraction minima appear to also be greater at lower altitude. These effects will have some influence on the AM noise level in the signal, although we do not consider this calculation sufficiently well checked out to quote a value. The effects of simulated turbulence are considerably less at P-band than at S-band.

We have performed a few calculations in which the effects of the parameters entering the turbulence simulation have been varied in order to determine the sensitivity of the propagation calculation to them. The scale of turbulence (which determines the saturation wavenumber k_o --see

6-2

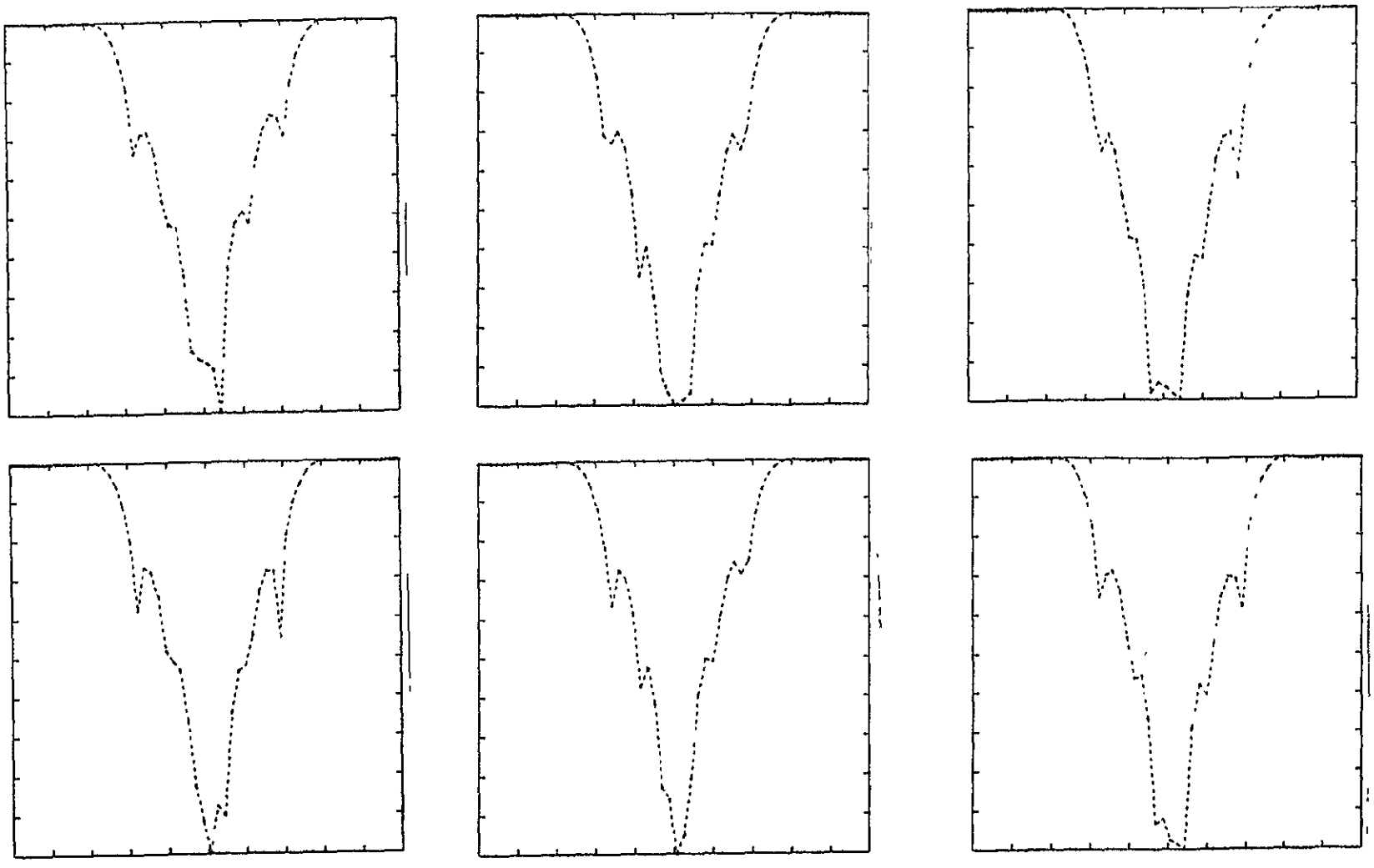

Figure 34. Plots of field intensity $|\psi|^2$ in db vs. aspect angle θ_y (in solid motor plane) for several individual realizations of simulated plume turbulence. Titan III-C at 20 km. Compare with Figure 35.

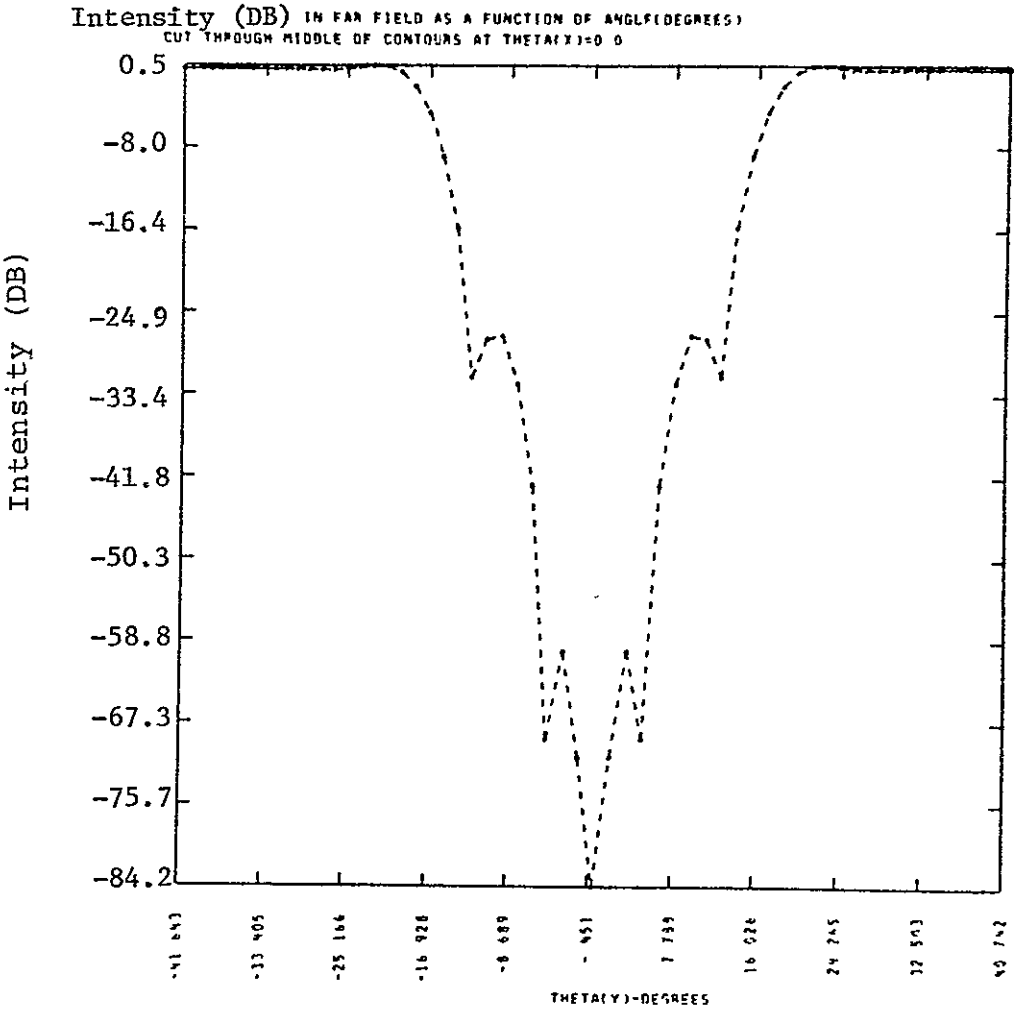

Figure 35. Plot of normalized intensity in db as a function of aspect angle θ_Y (in motor plane) in the far field. Titan III-C at 20.6 km.

Section 5 and Appendix II) is the parameter which has the greatest effect. Doubling or quadrupling the scale appears to introduce additional noise and 4-6 db greater signal attenuation at all angles where it exits. This finding should be taken as a caveat on our results. The scale in the outer regions of the mixing layer could be somewhat different from what we have assumed. It may be possible to determine effective values of the parameters by comparison with various data. Because coding of the turbulence model was not completed until late in the study, we have not done so.

6.2 Titan III-C Calculation and Comparison with Experiment

Calculations for the Titan III-C plume were performed at 20.6 and 36.0 km altitude, corresponding to times 80 and 110 seconds after liftoff, in order to compare the model predictions with field data. The first time corresponds approximately to the onset time for appreciable attenuation in Poehler's measurements. Only the solid motors (Stage 0) are burning at this time. The Stage I engines burn a mixture of hydrazine and unsymmetrical dimethylhydrazine (UDMH) with nitrogen tetroxide. Unlike the hydrogen-oxygen fuel used in the Shuttle orbiter stage, the Titan III-C Stage I propellant produces a somewhat ionized exhaust* and its plume produces attenuation at higher altitudes where the SRM's have been dropped (see Figure 3), and we

*H.A. Poehler ascribes the observed attenuation to the release of alkali metal impurities from the ablative shirt of the nozzles.

wish to avoid this complication. We thus do not treat the plume after Stage I ignition.

Figures 36-39 show calculated attenuations for the smooth flow field of the Titan III-C plumes at these altitudes. At the lower altitudes we have treated the plume as the superposition of two independent plumes from the two engines. At the higher altitude we have treated the plume as a single "merged" plume, i.e., as if it came from a single nozzle with the combined thrust of the two motors, by simply multiplying all plume dimensions by a factor of $\sqrt{2}$. In doing so we make errors in plume chemistry and local electron densities inside the plume; our previous calculations indicate that this is permissible.

These calculations are compared with Poehler's measurements in Figures 40-43. Since the observations are made at a variety of azimuthal angles, we show calculations both versus θ_x (normal to motor plane) and θ_y (in motor plane). The agreement between the calculation and the experiment is generally satisfactory at P-band and less so at S-band. One feature of the calculations which does not appear in the data is the strong attenuation of the S-band signal near tail aspect. Since the calculation is in fair agreement with measurements at angles greater than 5°, we believe that this strong tail-aspect attenuation is real. The data do not show it because

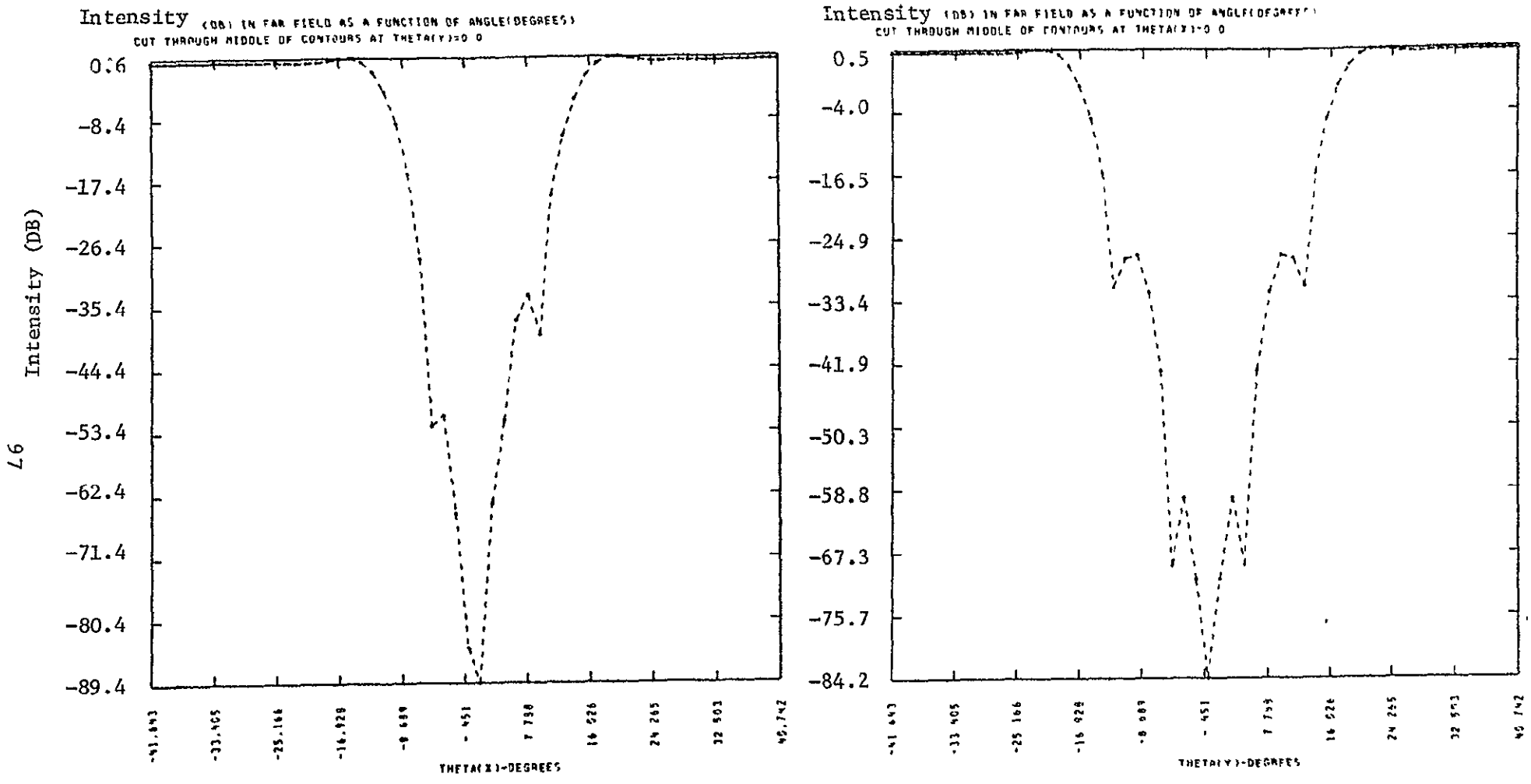

Figure 36. S-band attenuation vs. aspect angles θ_x and θ_y for Titan III-C at 20.6 km.

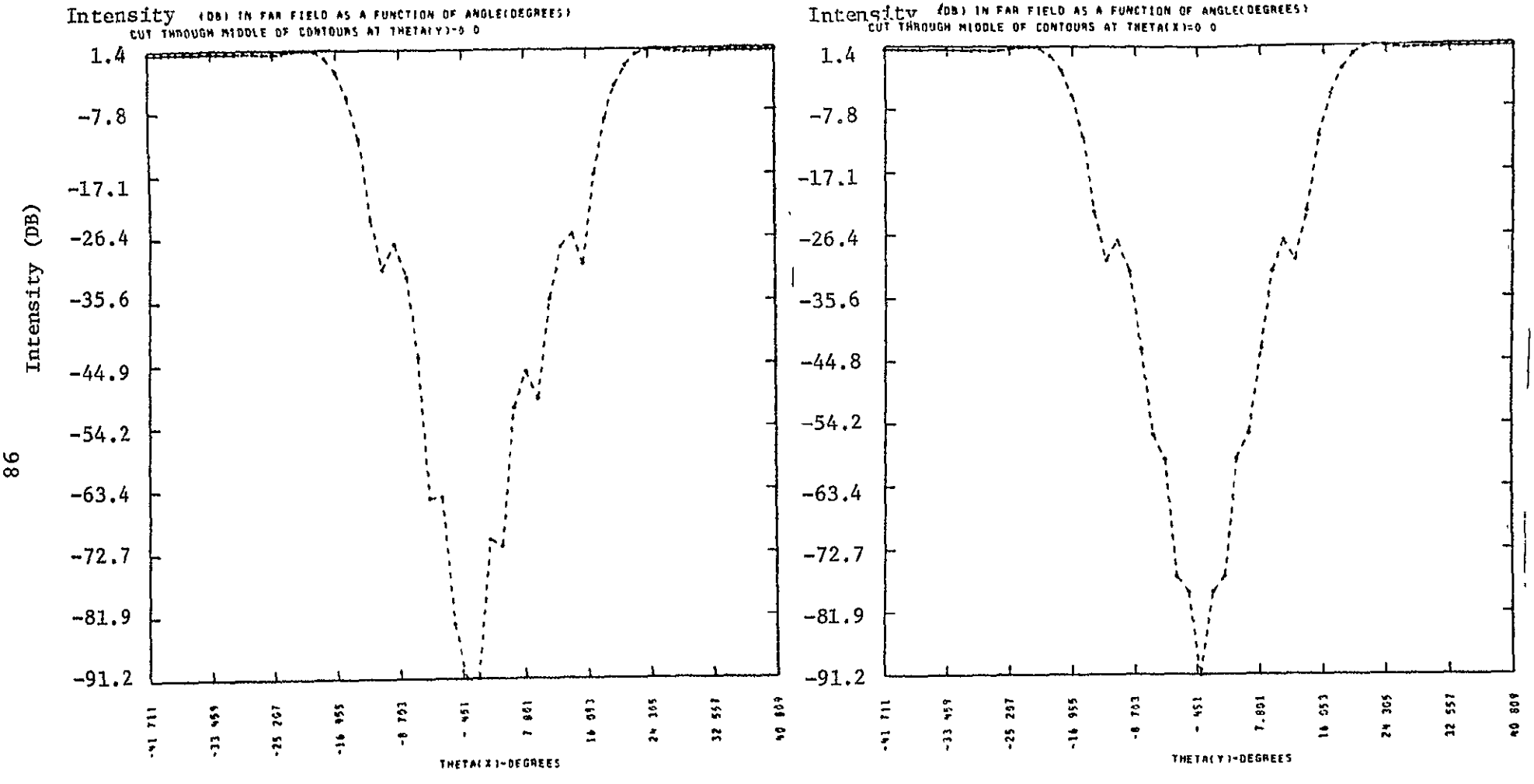

Figure 37. S-band attenuation vs. aspect angles θ_x and θ_y for Titan III-C at 36 km.

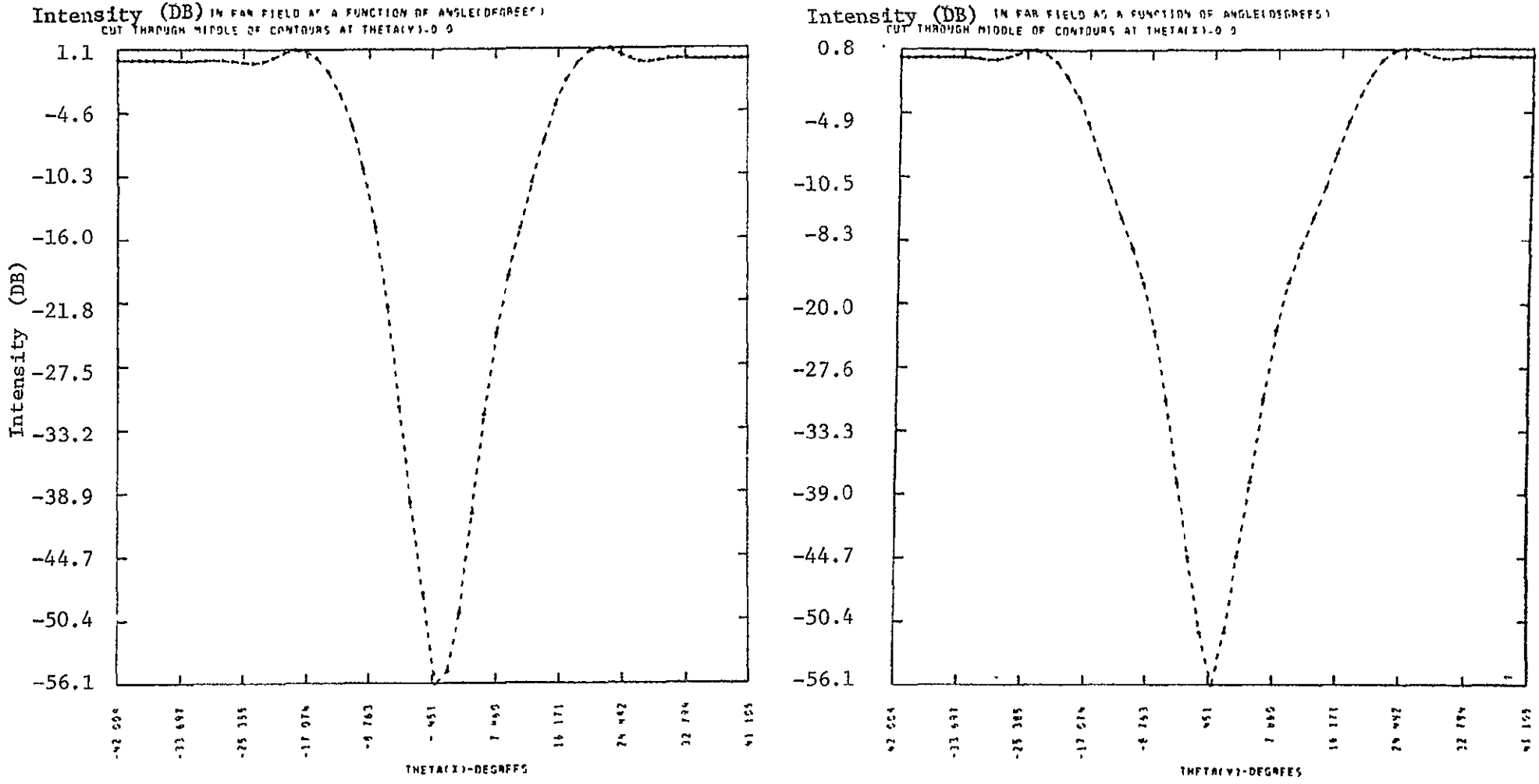

Figure 38. P-band attenuation vs. aspect angles θ_x and θ_y for for Titan III-C at 20.6 km.

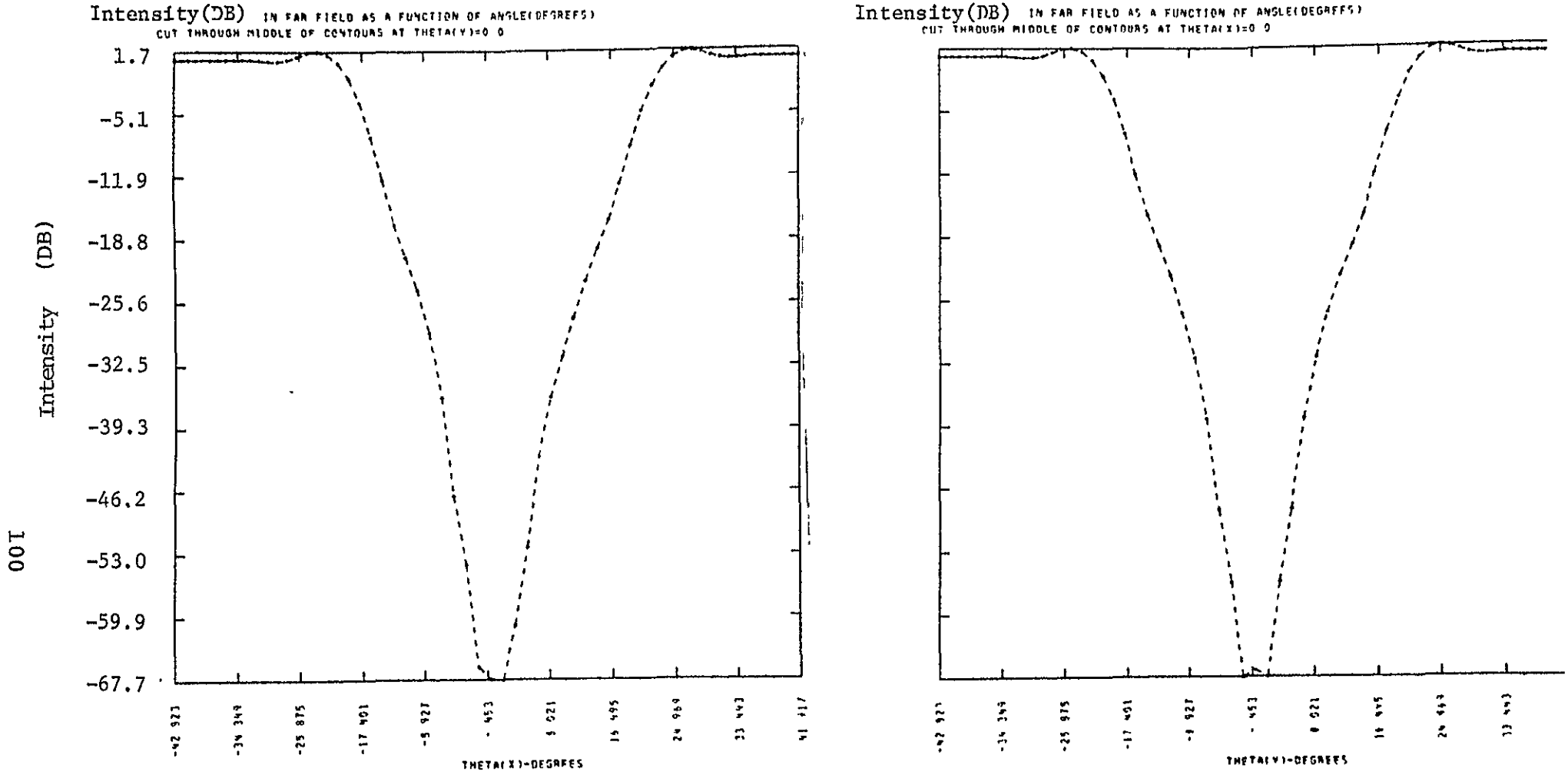

Figure 39. P-band attenuation vs. aspect angle θ_x and θ_y for Titan III-C at 36 km.

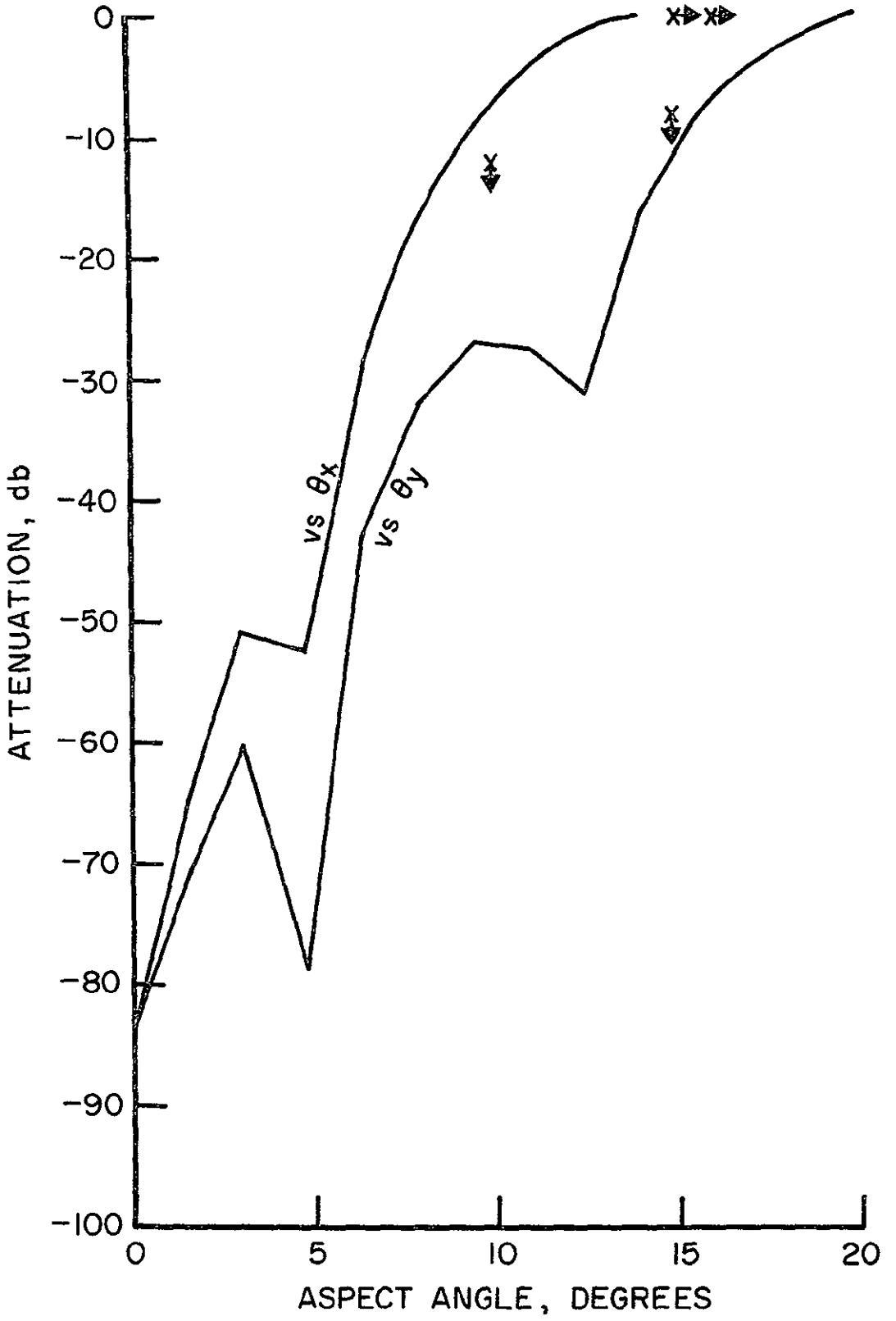

Figure 40. Comparisons between prediction and field data: Titan III-C at 20.6 km, S-band.

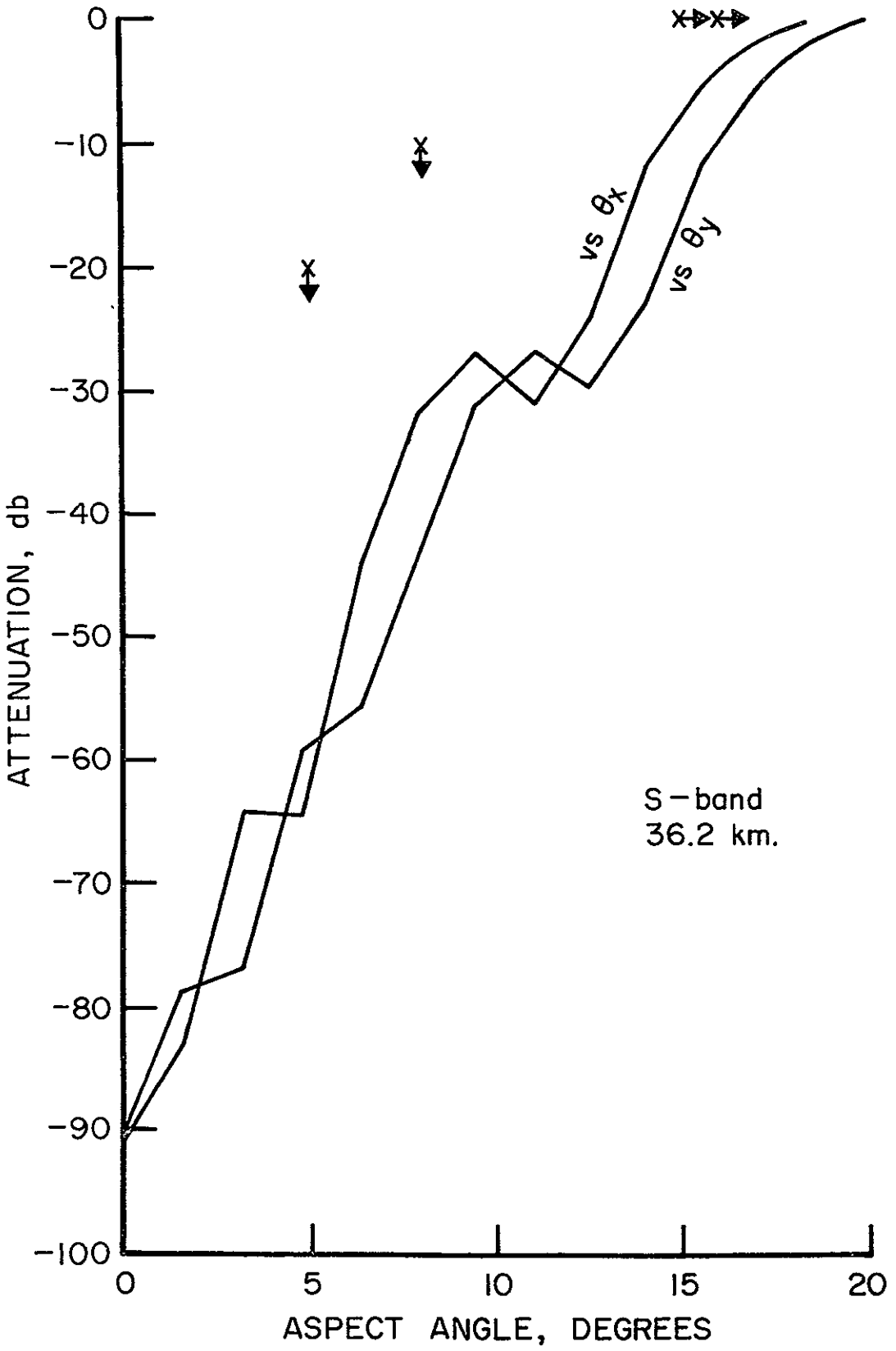

Figure 41. Comparisons between predictions and field data: Titan III-C at 36 km, S-band.

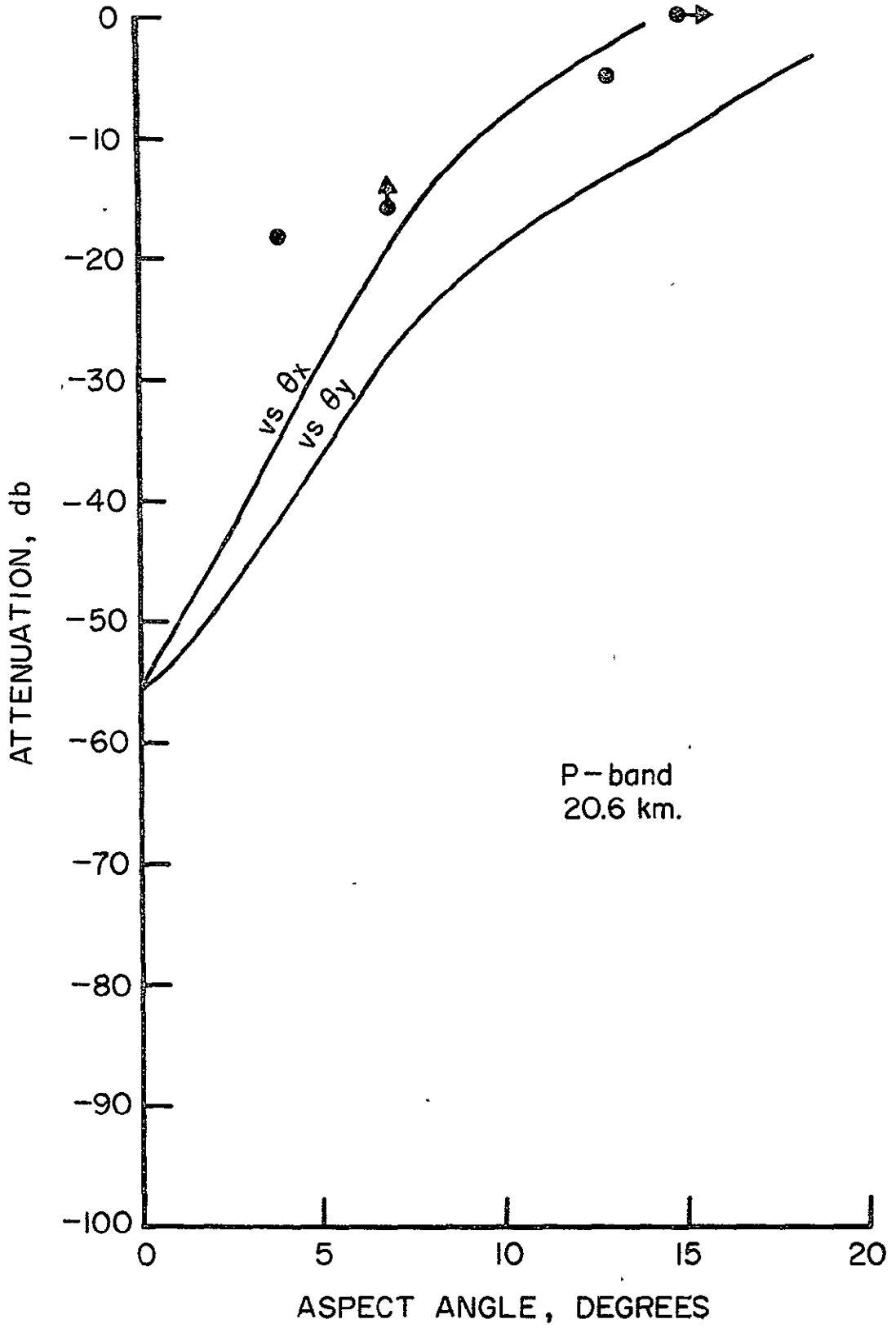

Figure 42. Comparisons between predictions and field data: Titan III-C at 20.6 km, P-band.

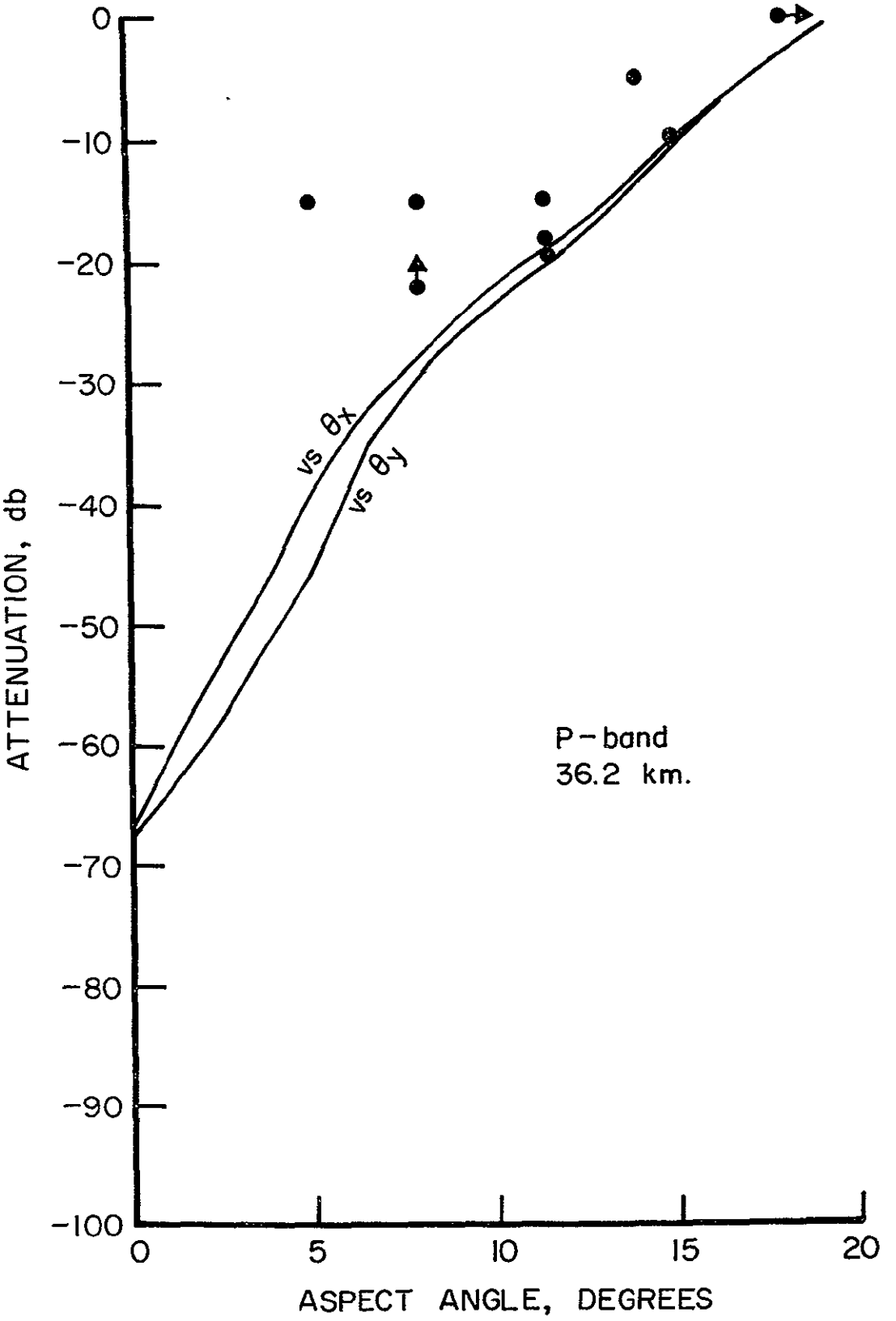

Figure 43. Comparisons between predictions and field measurements: Titan III-C at 36 km, P-band.

the fixed location of the ground stations and the launch geometry did not allow any measurements to be made at angles less than about 5 degrees.

Our investigations of the effects of simulated turbulence in the previous section indicated that large effects were not to be expected for mean signal attenuation. An average over a modest ensemble (10 realizations) of the turbulent displacement field did not produce any great difference from the smooth-flow calculations, although some smearing of the interference fringe effects near 10-12° at S-band was observed.

These comparisons indicate that our model has well reproduced the phenomenology of RF interference by large solid-motor plumes. The agreement with data is generally acceptable, although the high-altitude S-band predictions apppear to fall substantially below the measurements. Because our numerical resolution is not sufficient to resolve turbulent structures of the sort which would scatter S-band radiation strongly through the angles involved in bending the plume-skimming ray back toward tail aspect, it is conceivable that subgrid-level scattering processes may be involved in producing the high measured signals under these conditions; this subject remains to be explored. In any case, the calculation appears conservative, and it can be applied to the prediction of interference effects of the Space Shuttle plumes with reasonable confidence.

7.0 RESULTS FOR SPACE SHUTTLE

7.1 Results

We have performed several calculations of Shuttle SRB plume attenuation at the Range Safety signal frequency of 416.5 MHz. Our results are for the antennas on the SRB's; similar effects are expected for the external tank (ET) location. These calculations specify field intensities on a 64×64 grid in a far-field plane normal to the vehicle roll axis. Detailed results will be furnished separately to NASA/MSFC; in this report we show only selected features.

Figures 44-46 show attenuation results as functions of aspect angles θ_y and θ_x. Here the θ_x aspect is in the plane normal to the SRB's and the θ_y aspect is in the plane of the SRB's. The axis is a line parallel to the roll axis passing through the antenna. Because the antenna is offset in both x and y from the roll axis, no plane of symmetry exists in these calculations. The plume is treated as a linear superposition of two independent SRB plumes at the two lower altitudes, and as a single "merged" plume at the higher altitude. These calculations are for the mean flow field. Because of vehicle blockage effects not included in our calculations, only results on the side on which the antenna is located are likely to be meaningful. This is the side of <u>negative</u> θ_x and θ_y.

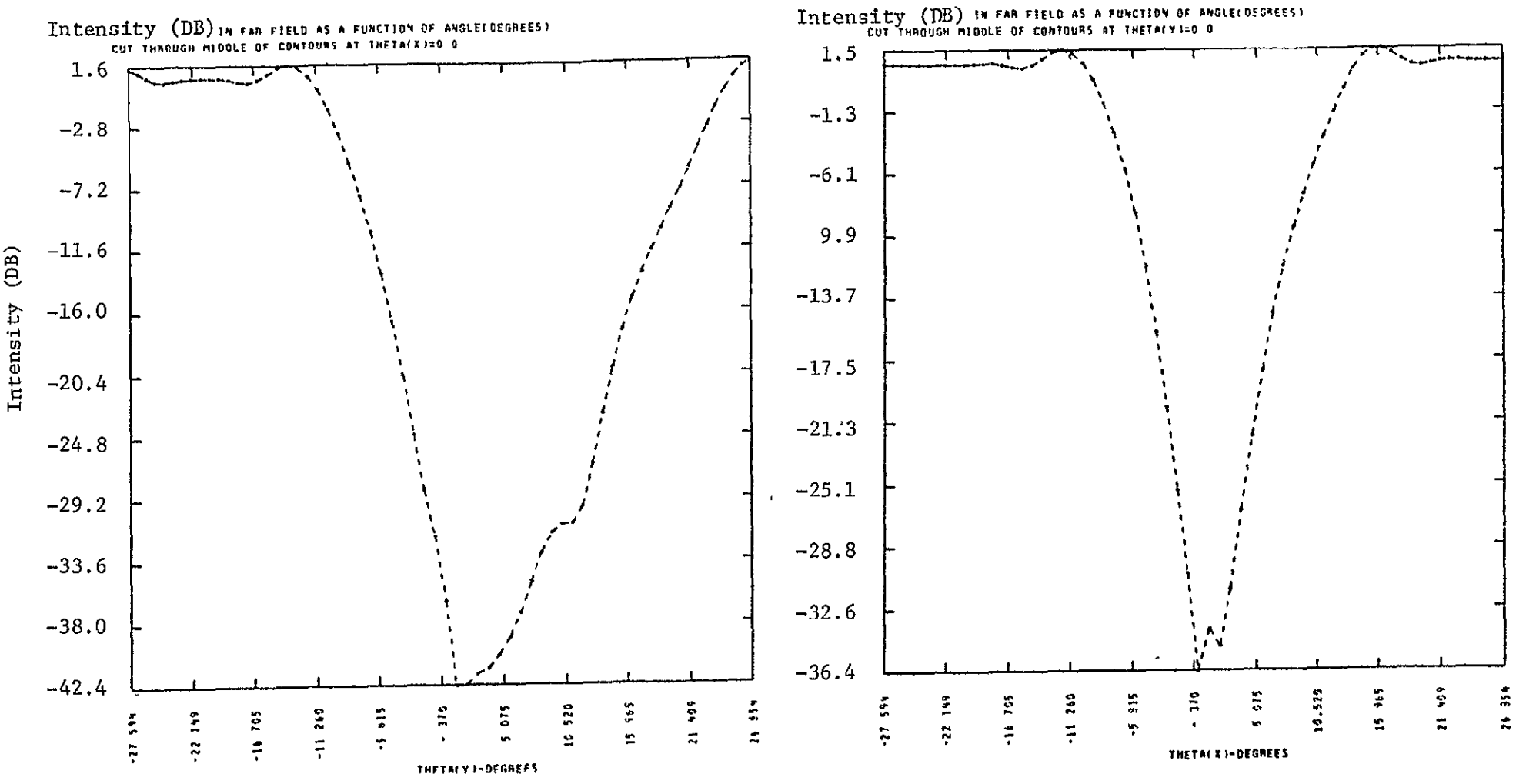

Figure 44. Predicted Space Shuttle range safety signal attenuation as a function of the aspect angle θ_y and θ_x at 9.3 km altitude (SRB antenna).

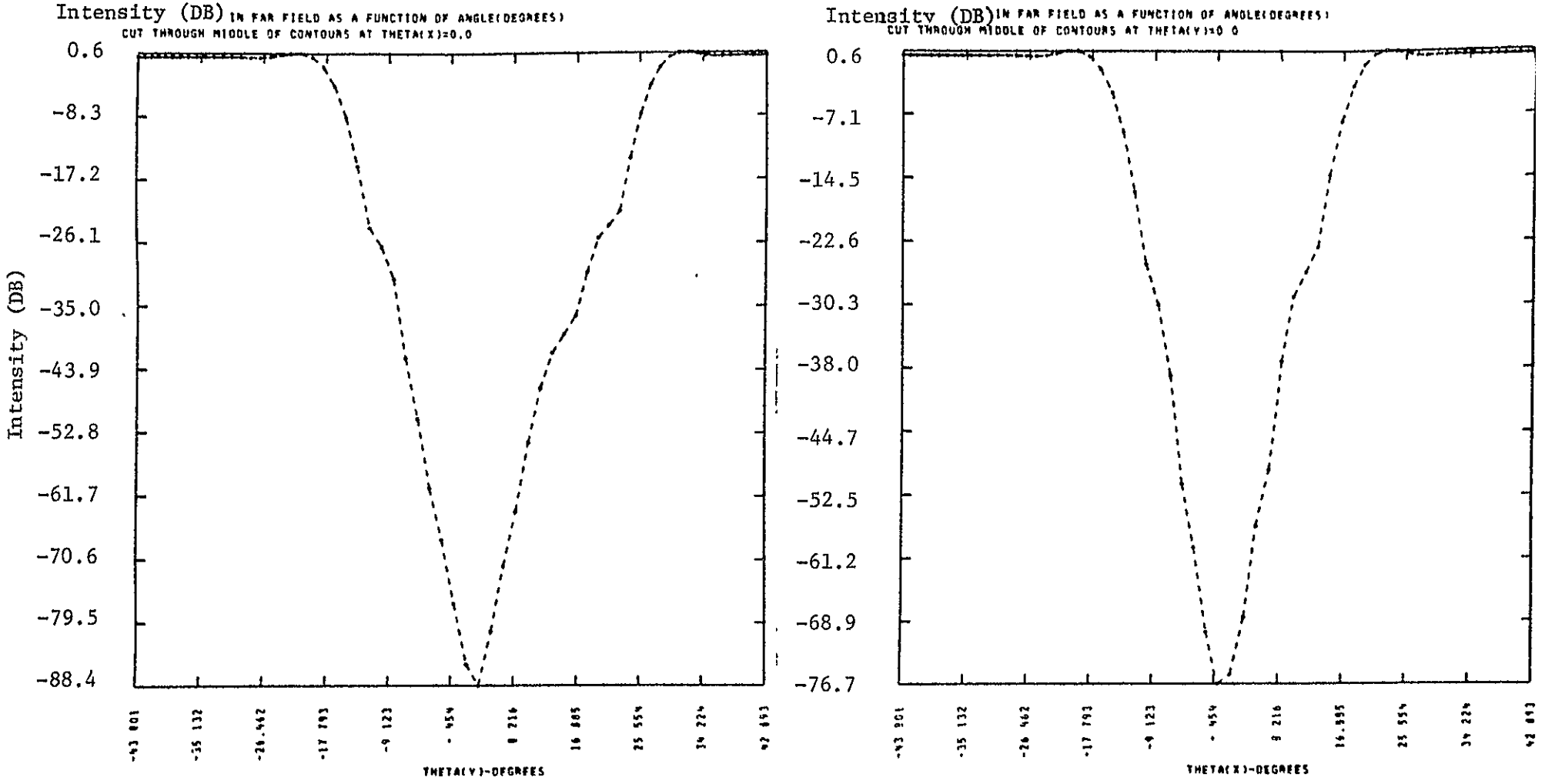

Figure 45. Predicted Space Shuttle range safety signal attenuation as a function of the aspect angles θ_y and θ_s at 25 km altitude (SRB antenna).

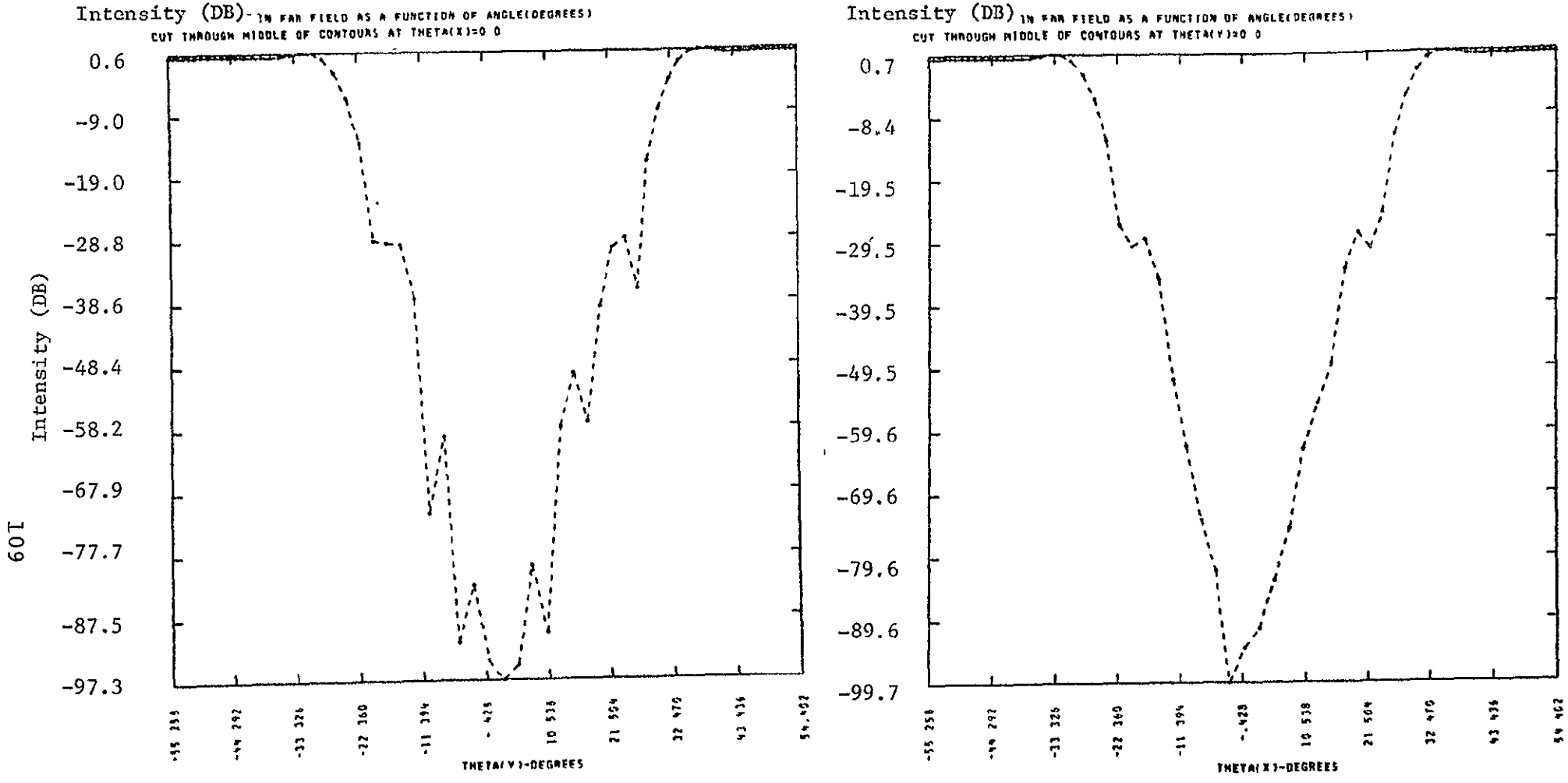

Figure 46. Predicted Space Shuttle range safety signal attenuation as a function of the aspect angles θ_y and θ_x at 37.5 km altitude (SRB antenna).

Obtaining reliable results on the far side of the vehicle would require dropping our assumption that the antenna pattern is isotropic and (most probably) embarking on detailed analysis of vehicle skin currents, a task outside the scope of this study.

In addition to these calculations for the nominal flow fields, we have examined the effects of turbulence and of variations in descriptions of turbulent mixing and electron chemistry in the edge region. In the case of the latter two quantities, Lockheed has estimated a correction to the effective radial position of the plume boundary which depends on axial distance and (in the case of mixing) on turbulence. The effect in both cases is to displace the boundary slightly inward, i.e., toward the plume centerline, from the nominally calculated value. The change in mixing model makes electron-rich material diffuse less rapidly, while the changes in chemistry result in more rapid electron loss in the outer regions of the plume because of attachment to atmospheric species.

Figures 47-49 show contour plots of the normalized far-field intensity, $|\psi|^2/|\psi_o|^2$, in db where $|\psi_o|^2$ is the intensity in the absence of a plume, for the nominal plume calculation. The lower left quadrant of these and succeeding plots corresponds to angles in the quadrant of the antenna with respect to the roll axis.

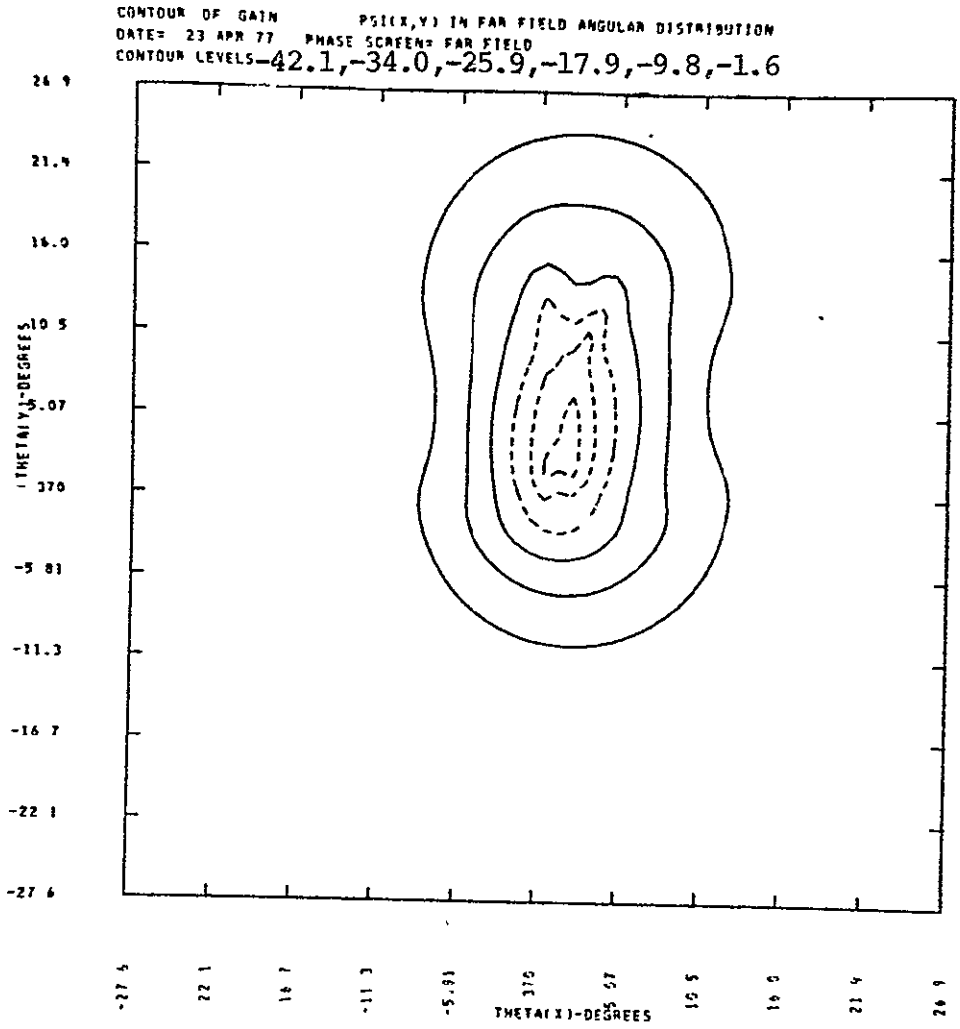

Figure 47. Contours of normalized far-field intensity for Space Shuttle at 9.3 km altitude. Nominal mean flow field. Contour levels on this and succeeding plots are in db.

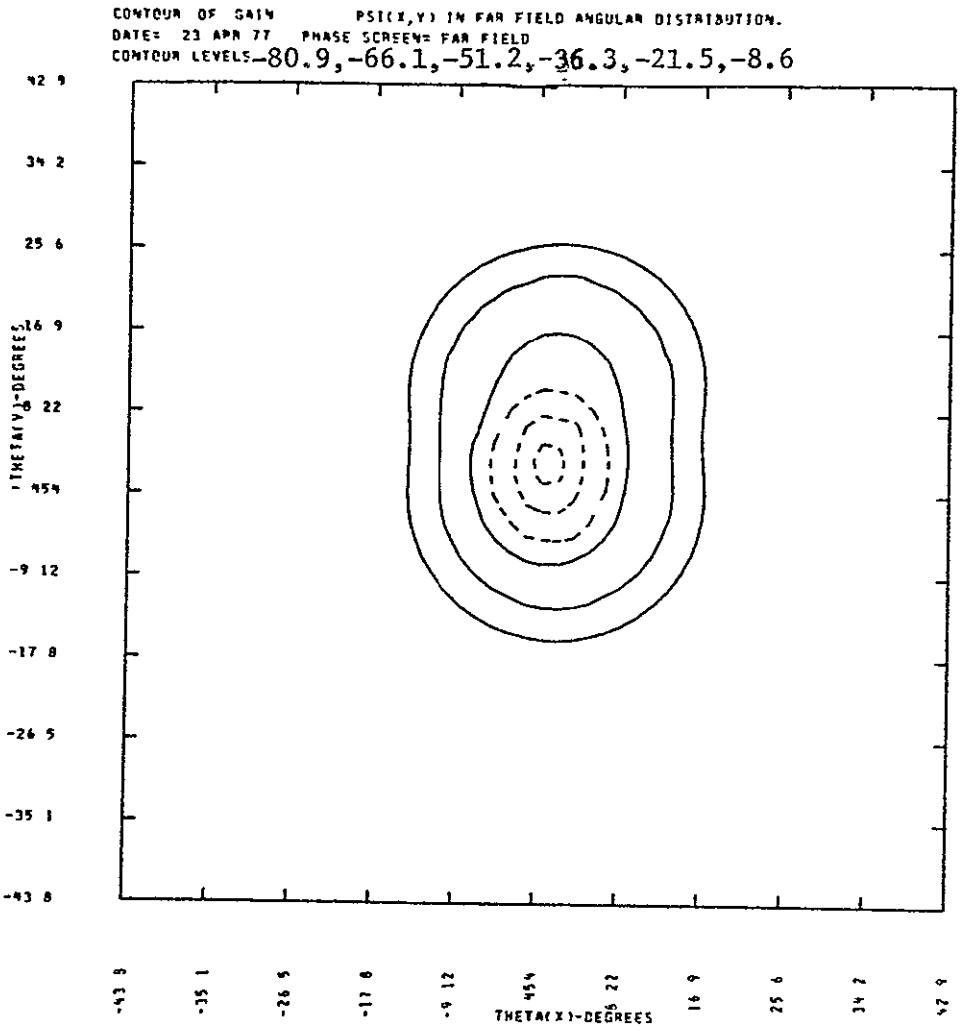

Figure 48. Contours of normalized far-field intensity for Space Shuttle at 25 km altitude. Nominal mean flow field.

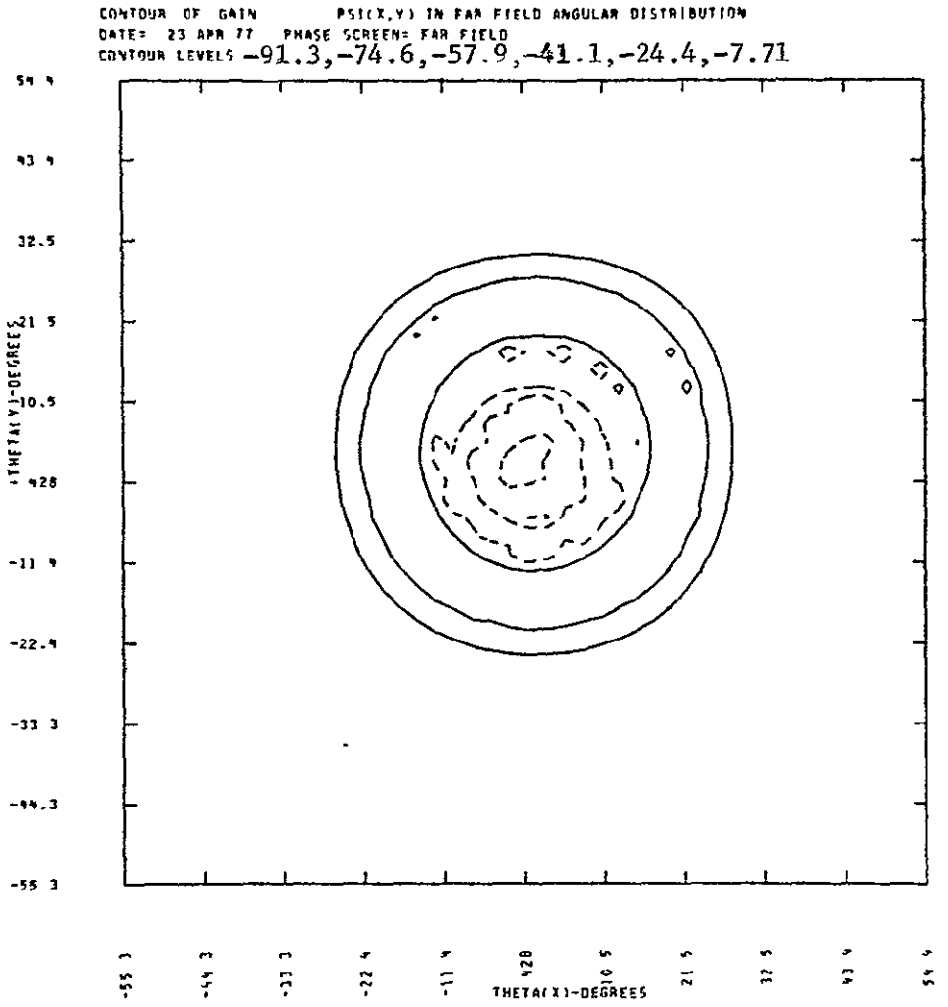

Figure 49. Contours of normalized far-field intensity for Space Shuttle at 37.5 km altitude. Nominal flow calculation.

Figures 50-52 show similar contours for calculations in which Lockheed's recommended plume boundary position variation has been applied to the nominal flow fields. In these cases the plume with variations in mixing rate is on the left, and the plume with variations in edge electron chemistry on the right. (The easiest way to compare these with the nominal contours is to make copies and overlay the contour plots, since the contour levels are generally similar.) In general, applying these variations to the flow field results in a slight decrease in attenuation (or increase in the transmitted signal). Local attenuation increases can occur as the result of changes in the position of interference fringes. Since the effect of turbulence is to smear out these fringe patterns, we do not believe that these modest local increases in attenuation should be considered important.

The effects of turbulence on the normalized far-field intensity are shown in Figures 53-55. These calculations are the average amplitude over ten realizations of the turbulent plume. Including simulated turbulence causes a slight broadening and deepening of the attenuation pattern, similar to the effects shown in Section 6.1 The effects are greatest at tail aspect and somewhat greater at the higher altitudes. In general, large effects are found only when the signal loss due to the mean flow is high ($\gtrsim$ 70 db).

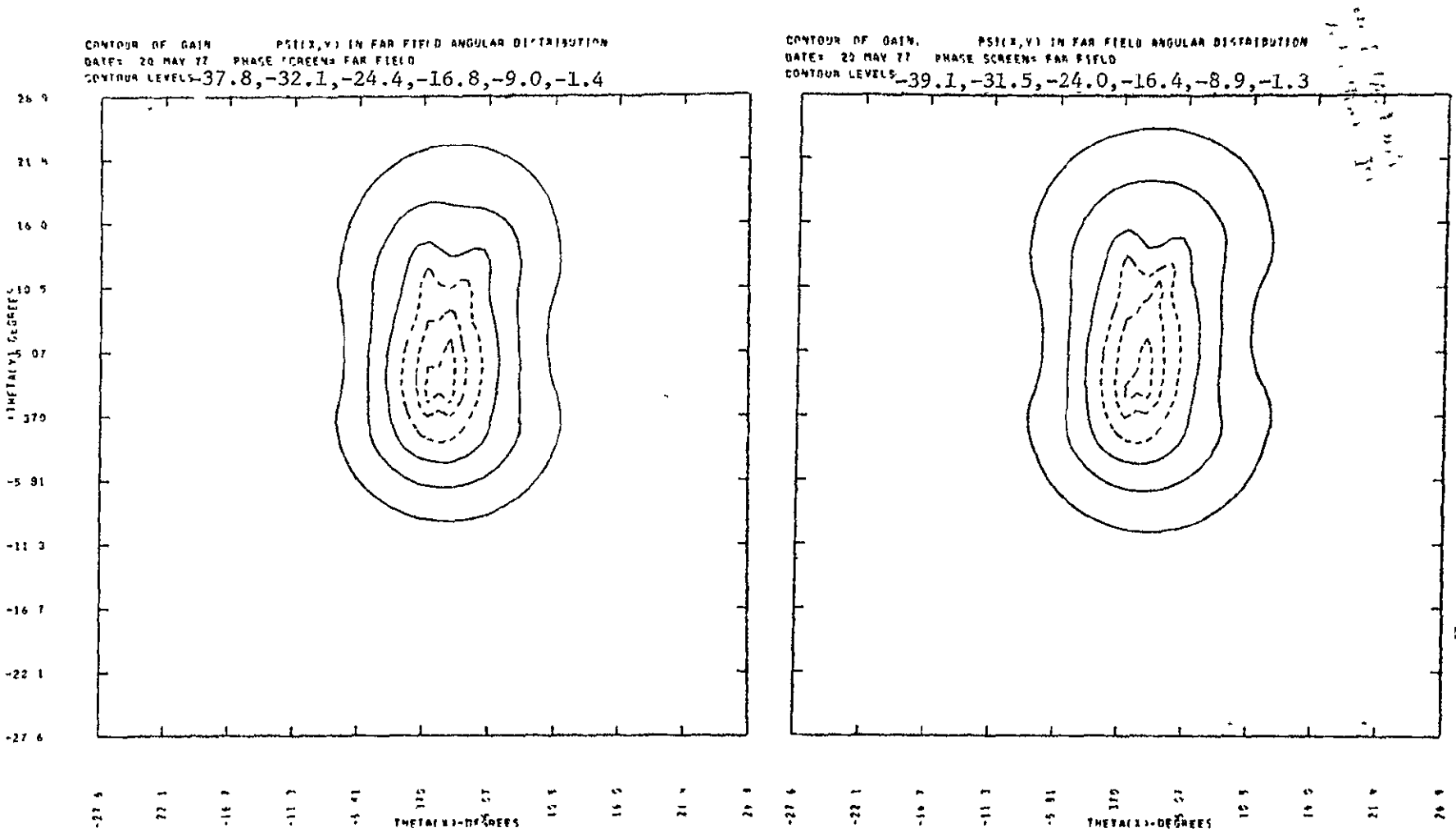

Figure 50. Contours of normalized far-field intensity for Space Shuttle at 25 km altitude. Left, mixing variation; right, edge kinetics variation.

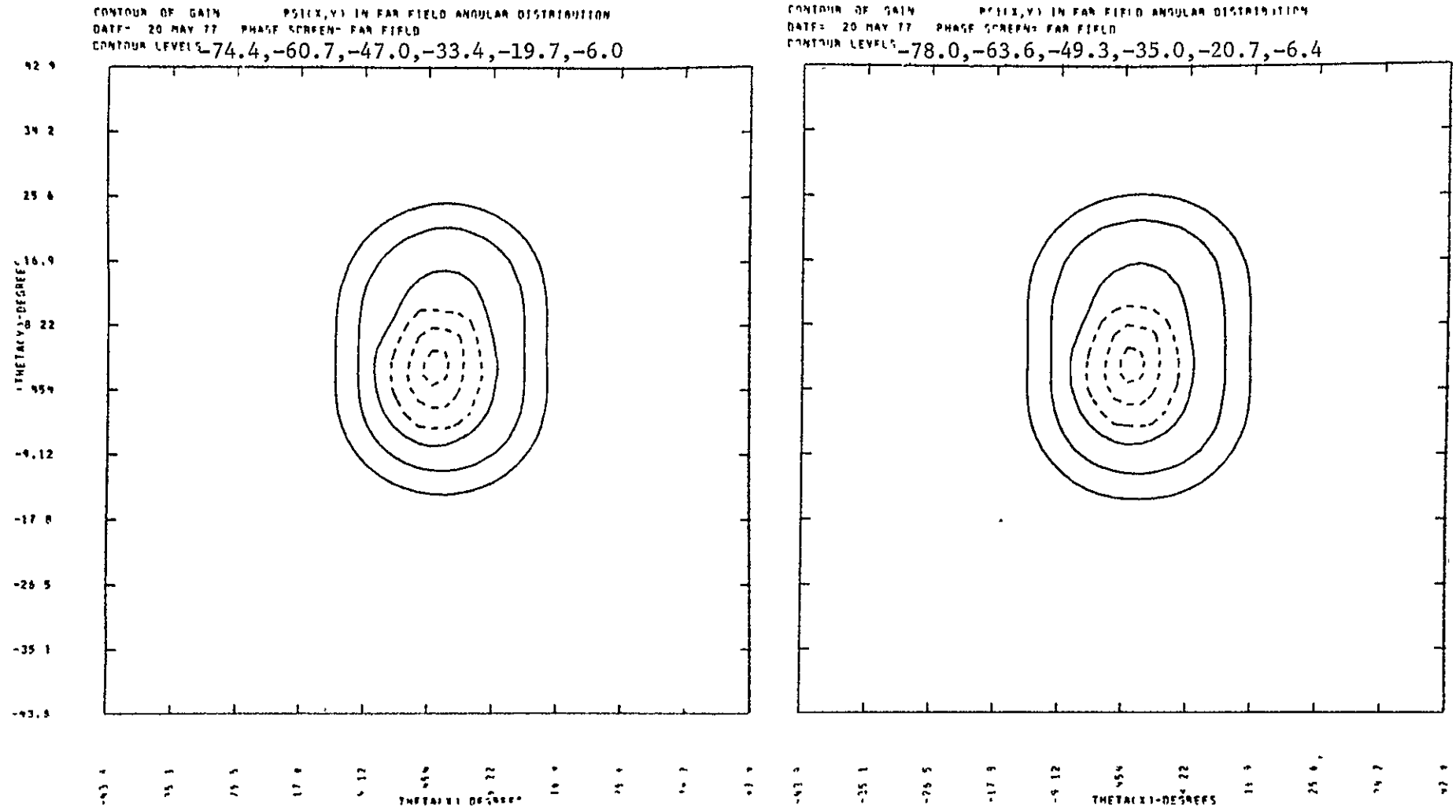

Figure 51. Contours of normalized far-field intensity for Space Shuttle at 25 km altitude. Left, mixing variation; right, edge kinetics variation.

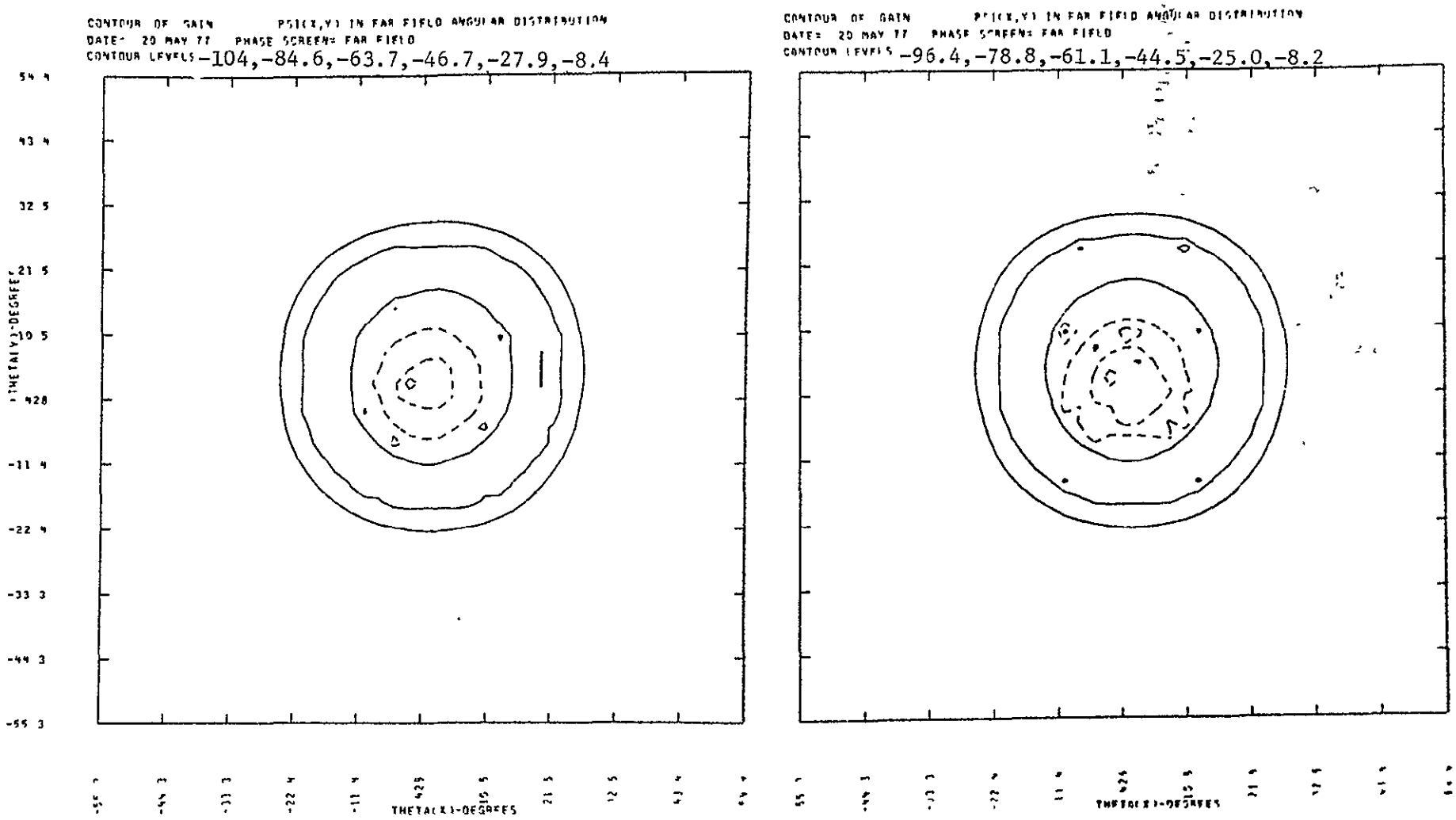

Figure 52. Contours of normalized far-field intensity for Space Shuttle at 37.5 km altitude. Left, mixing variation; right, edge kinetics variation.

Contour levels: -49.4, -41.2, -32.8,
-24.6, -16.3, -8.0

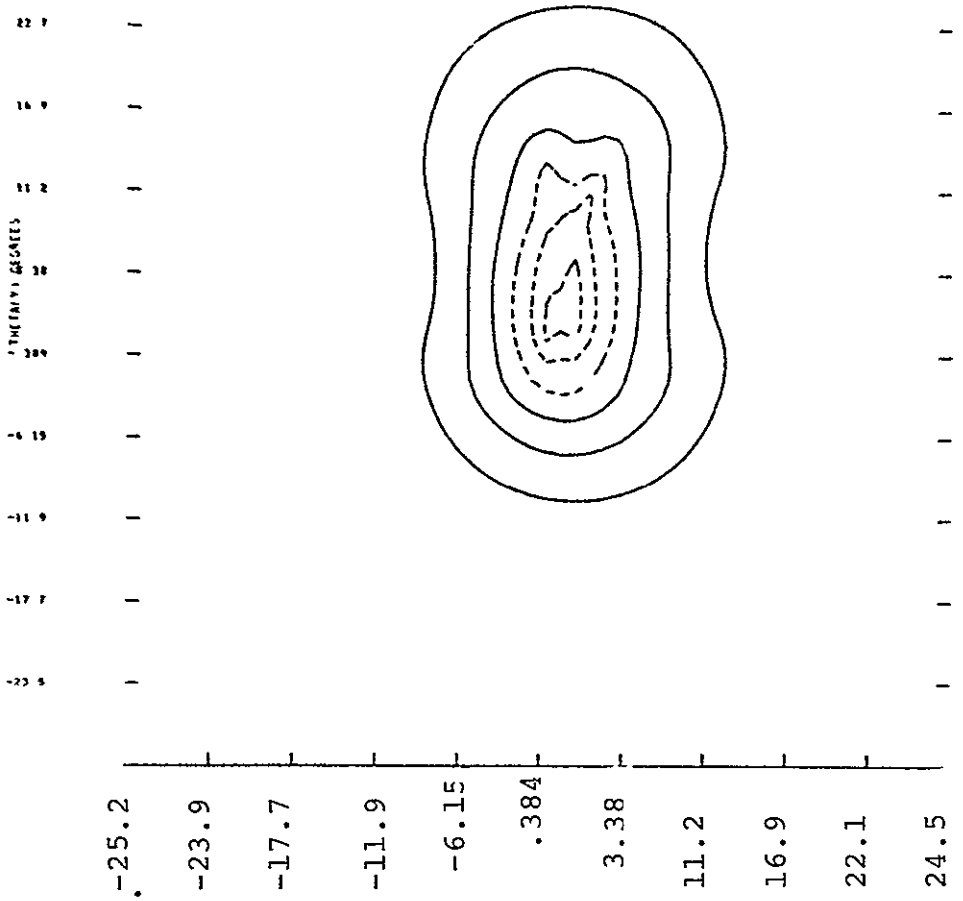

Figure 53. Contours of normalized far-field intensity for Space Shuttle at 9.3 km altitude. Average of 10 realizations of simulated turbulence.

Contour levels: -91.4, -75.2, -61.0

-44.4, -28.6, -11.0

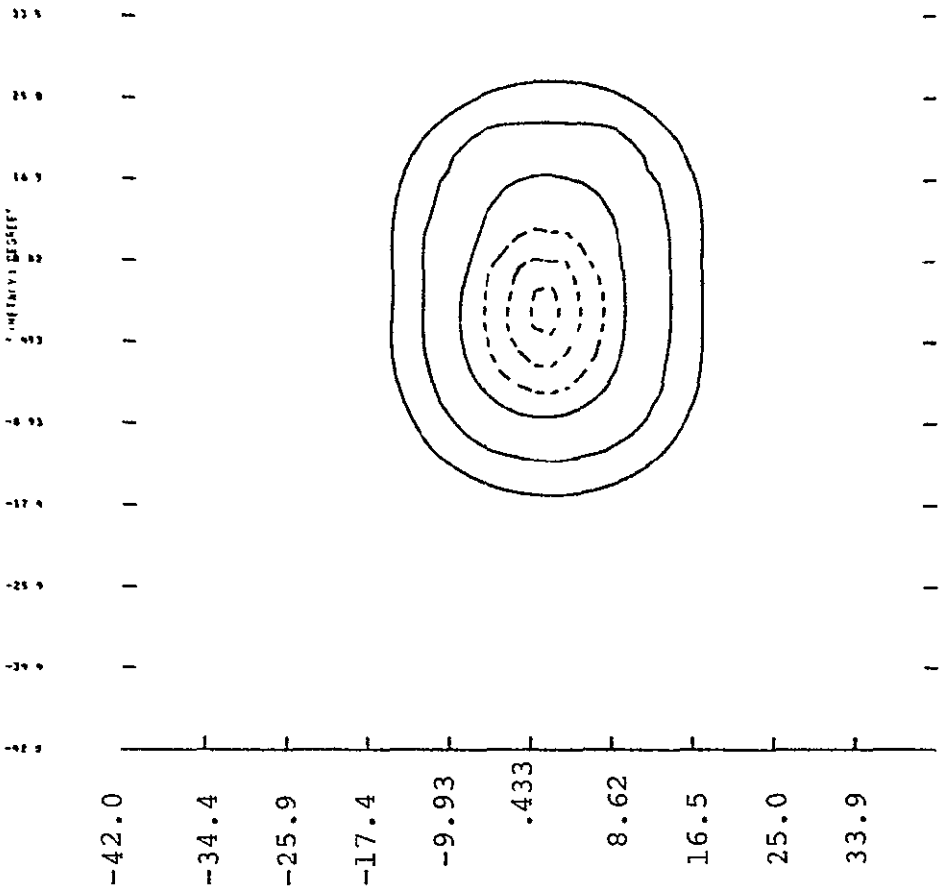

Figure 54. Contours of normalized far-field intensity for Space Shuttle at 25 km altitude. Average of 10 realizations of simulated turbulence.

Contour levels: -113.8, -93.4, -73.8,
-54.2, -34.6, -15.2

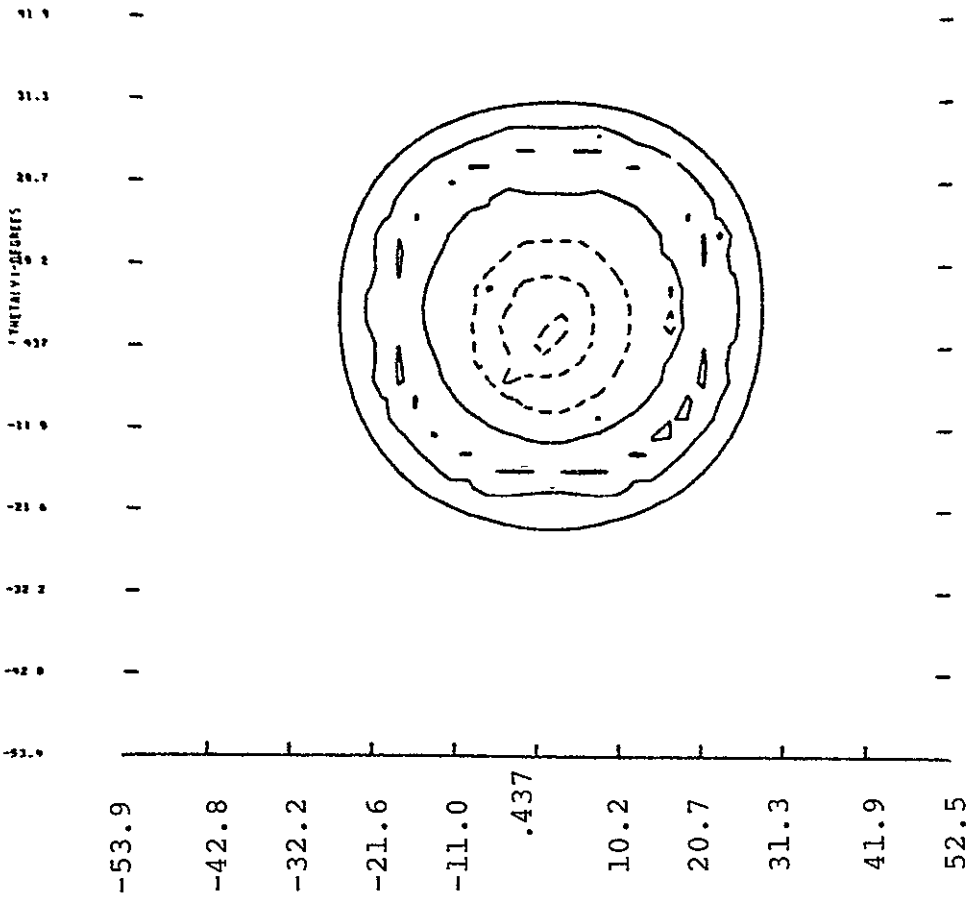

Figure 55. Contours of normalized far-field intensity for Space Shuttle at 37.5 km altitude. Average of 10 realizations of simulated turbulence.

7.2 Comments and Conclusions

Comparisons of our signal interference calculations for Space Shuttle during SRB burn with those for Titan III-C 0^{th} Stage indicate that, at any given altitude, the Space Shuttle plume induces a greater signal loss than the Titan III-C plume at UHF-VHF frequencies. This is a result of the generally increased geometric blockage for the Shuttle, as evidenced in Figures 8 and 9. Although we have not performed calculations at S-band, we believe that the interference effects for Space Shuttle will also be greater at high frequencies. Signal losses of 30 db or greater have been said to cause difficulty with the Range Safety system.* The aspect angles at which these attenuation levels are predicted are about 1°, 9°, and 15-20°, depending on azimuthal angle, for altitudes of 9.3 km, 25 km, and 37.5 km, respectively. The implications on location of transmission sites depend upon whether the system must transmit a signal under nominal or "worst-case" trajectory conditions. The range of excluded aspect angles increases with increasing altitude and should continue to do so until SRB burnout. A higher or lower value of the maximum acceptable signal loss would result in onset of the

*Lee Malone, NASA/MSFC, private communication.

attenuation problem at a lower or higher altitude, respectively, and a greater or lesser range of excluded aspect angles at the higher altitudes.

In applying these results to evaluating the locations of alternate transmission sites for Range Safety transmitters (to insure that at least one transmitter has a low-loss path to the vehicle), a reasonable degree of conservatism would appear to result in preferring the predictions based on the nominal flow field over those in which the mixing rate and edge kinetics variations have been included. The comparisons of the Titan III-C predictions with measurements indicate that the mean flow predictions are close to measured values. The effects of simulated turbulence cause a modest broadening and deepening of the attenuation pattern. Because coding of the turbulence model was completed late in the study period, we have not had much time to study its effects on the signal under various parameter variations. It is also desirable to compare the results with a greater variety of data, such as those to be obtained in static test experiments. We therefore recommend that our mean-flow results be used in design analyses, but that a 5-db safety factor be applied to any calculated result in

which the nominal predicted signal loss is less than 30 db. This procedure not only is consistent with the effects of including simulated turbulence, but also would result in our calculated results for Titan III-C lying at the lower edge of the scatter in Poehlers' data.

In all our calculations we have assumed that the antenna pattern is isotropic. We have already noted that our results are probably unreliable on the occluded side of the vehicle. If the near-field pattern were known in the vicinity of the vehicle, we could have used it as an initial condition to the propagation calculation; however, only the far-field (Fraunhofer) pattern is known.

The total signal loss is a combination of antenna pattern losses and plume-induced losses. Because the transmitted signal is diffracted around the edges of the plume rather than propagated directly through it, the resultant signal loss at some point in the plume shadow is not simply the db sum of the antenna loss and the plume loss at that point. Calculating the signal loss by such a procedure would be overly conservative in the case that a region of high antenna loss coincides with a region of high plume loss. One could conceive also of conditions under which it is optimistic. A more realistic procedure is to add the db plume loss to the db antenna loss at the plume edge. Because the signal near small aspect angles, where high plume-induced

losses occur, is the contribution of rays diffracted over a region of the plume edge, it is reasonable to calculate the effective antenna contribution as a linear (not logarithmic) average over some range of azimuthal angles at aspect angles where the plume-induced loss is 3 db. The range of azimuthal angles will depend upon the shape of the plume pattern and the location of the point in question. For small aspect angles, an average over 90° in the quadrant about the roll axis containing the antenna appears reasonable.

APPENDIX I: The Parabolic Wave Equation and the Split Operator Solution

It is easy to show, starting with Maxwell's equations, that the basic wave equation for the electric field amplitude is

$$\frac{1}{c^2}\frac{\partial^2 E}{\partial t^2} = \frac{1}{\varepsilon}\ \nabla^2 E \qquad \text{(I-1)}$$

where ε is the dielectric constant. Letting the time-dependent part of the quasi-steady solution be given as $e^{i\omega t}$ where $\omega = ck$, we obtain Helmholtz' equation

$$\nabla^2 E + k^2 \varepsilon E = 0 \quad . \qquad \text{(I-2)}$$

Now assume that propagation is predominantly in the direction of the z axis and that the field is represented as the product of a sinusoidal term e^{ikz} and a slowly varying term $\psi(x,y,z)$; then

$$\frac{\partial^2}{\partial z^2}\left[e^{ikz}\ \psi\right] + \left[\nabla_\perp^2\ \psi + k^2\ \varepsilon\ \psi\ \right] e^{ikz} = 0 \quad . \qquad \text{(I-3)}$$

Carrying out the z differentiation and neglecting the second derivative of the slowly varying quantity ψ gives

$$2i\ k\ \frac{\partial \psi}{\partial z} = \nabla_\perp^2\ \psi + k^2(\varepsilon - 1)\ \psi = 0 \qquad \text{(I-4)}$$

which is the parabolic wave equation.

A formal solution to this equation over a propagation step $z^n \rightarrow z^{n+1}$ is

$$\psi^{n+1} = \exp\left\{-\frac{i}{2k}\left[\Delta z\ \nabla_\perp^2 + k^2 \int_{z_n}^{z_{n+1}} (\varepsilon-1)\ dz\right]\right\}\psi^n. \quad \text{(I-5)}$$

For any analytic function $(\varepsilon-1)$ such that a Taylor series in z exists, this is equivalent to second order in z to the symmetrized split operator form

$$\psi^{n+1} = e^{-\frac{i}{4k}\Delta z\nabla_\perp^2}\ e^{-\frac{ik}{2}\Delta z\overline{(\varepsilon-1)}}\ e^{-\frac{i}{4k}\Delta z\nabla_\perp^2}\ \psi^n \quad . \quad \text{(I-6)}$$

The proof below is taken from Fleck, Morris, and Feit (1975).

Consider the somewhat simpler equation

$$\frac{\partial\psi}{\partial z} = a(z)\ \psi = (\nabla_\perp^2 + b)\ \psi \ . \quad \text{(I-7)}$$

Formally,

$$\psi(z) = \exp\left\{\int_o^z a(z')\ dz'\right\} \quad \text{(I-8)}$$

where the exponent is taken to mean

$$\exp\left\{\int_o^z a(z')\ dz'\right\} = 1 + \int_o^z a(z')dz' + \int_o^z a(z')dz' \int_o^{z'} a(z")dz" + \text{-----} \quad \text{(I-9)}$$

Substituting for $a(z)$ and keeping terms through second order in z we have

$$\exp\left\{\int_0^z a(z')dz'\right\} = 1 + \nabla_\perp^2 z + \int_0^z b(z)dz' + \nabla_\perp^2 \frac{z^2}{2}$$
$$+ \nabla_\perp^2 \int_0^z dz' \int_0^{z'} b(z'')dz'' + \int_0^z b(z')z' \nabla_\perp^2 dz'$$
$$+ \int_0^z b(z')dz' \int_0^{z'} b(z'')dz'' \quad . \tag{I-10}$$

Also to second order in z,

$$e^{\frac{1}{2}\nabla_\perp^2 z} e^{\int_0^z b(z')dz'} e^{\frac{1}{2}\nabla_\perp^2 z} = 1 + \nabla_\perp^2 \frac{z^2}{2} + \int_0^z b(z')dz'$$
$$+ \int_0^z b(z')dz' \int_0^{z'} b(z'')dz'' + \nabla_\perp^2 \frac{z}{2} \int_0^z b(z')dz'$$
$$+ \frac{z}{2} \int_0^z b(z') \nabla_\perp^2 dz' \tag{I-11}$$

and therefore

$$\exp\left\{\int_o^z a(z')dz'\right\} = e^{\frac{1}{2}\nabla_\perp^2 z}\ e^{\int_o^z b(z')dz'}\ e^{\frac{1}{2}\nabla_\perp^2 z}$$

$$- \nabla_\perp^2 \int_o^z dz' \left[\frac{z}{2} b(z') - \int_o^{z'} b(z'')dz'\right]$$

$$- \int_o^z dz'\ b(z')\ \left(\frac{z}{2} - z'\right)\ \nabla_\perp^2 + \mathcal{O}(z^3) \quad . \qquad \text{(I-12)}$$

Now if $b(z)$ has a Taylor series representation in z,

$$b(z) = b(o) + b'(o)\ z + b''(o)\ z^2 + \text{----} \qquad \text{(I-13)}$$

all the remainder terms are third order. Thus, through terms of second order in z, the split operator form is a solution to the model equation, which differs from the parabolic wave equation only by nomenclature.

APPENDIX II: Relation of k_o to the Integral Scale Turbulence

The integral or outer scale of turbulence is defined as (see, e.g., Bradshaw, 1976)

$$L_{T,x} = \frac{1}{2} \int_{-\infty}^{\infty} \langle u_x(o)\ u_x(x) \rangle\ dx / \langle u^2(o) \rangle \qquad \text{(II-1)}$$

where $\langle u_x(o)\ u_x(x) \rangle$ is the two-point velocity correlation function for the x direction. (In isotropic turbulence this scale is independent of direction.) Here we have used the fact that $\langle u(o)\ u(x) \rangle$ is a symmetric function of x to extend the range of the integral to $-\infty$. A one-dimensional power spectrum of the turbulent fluctuations is defined as

$$\phi_{xx}(k_x) = \frac{1}{2\pi} \int_{-\infty}^{\infty} \langle u_x(o)\ u_x(x) \rangle\ e^{ik_x x}\ dx \qquad \text{(II-2)}$$

so that

$$u_x(o)\ u_x(x) = \int_{-\infty}^{\infty} \phi_{xx}(k_x)\ e^{ik_x x}\ dk_x \quad . \qquad \text{(II-3)}$$

The three-dimensional power spectrum $\Phi_{xx}(\vec{k})$ is defined as

$$\Phi_{xx}(\vec{k}) = \frac{1}{(2\pi)^3} \int \langle u_x(o)\ u_x(\vec{x}) \rangle\ e^{-i\vec{k}\cdot\vec{x}}\ d^3\vec{x} \quad . \qquad \text{(II-4)}$$

Here the xx subscript reminds us of the direction of the velocities. The one-dimensional spectrum defined above is the projection of the three-dimensional spectrum on the k_2 axis:

$$\phi_{xx}(k_x) = \int_{-\infty}^{\infty}\int_{-\infty}^{\infty} \Phi_{xx}(k_x, k_y, k_z)\, dk_x\, dk_y \quad . \qquad \text{(II-5)}$$

(It should be distinguished from another kind of one-dimensional spectrum $\phi(k)$, which results from integrating $\Phi(\vec{k})$ over all solid angles at a given value of $k = |\vec{k}|$. It is this other spectrum $\phi(k)$ which obeys the Kolmogorov law in the inertial regime.) In terms of the 1-D and 3-D spectra ϕ_{xx} and Φ_{xx} we can express L_T as

$$L = \frac{1}{2} \int_{-\infty}^{\infty}\int_{-\infty}^{\infty} \phi_{xx}(k_x)\, e^{ik_x x}\, dk_x\, dx \Big/ \int \Phi_{xx}(\vec{k})\, d^3\vec{k} \,. \qquad \text{(II-6)}$$

Using the relation (II-5) between the 1-D and 3-D spectra, we can write

$$L_T = \frac{1}{2} \int_{-\infty}^{\infty}\int_{-\infty}^{\infty}\int_{-\infty}^{\infty}\int_{-\infty}^{\infty} \Phi_{xx}(\vec{k})\, dk_y\, dk_z\, e^{ik_x x}\, dk_x\, dx \Big/$$

$$\int \Phi_x(\vec{k})\, d^3\vec{k} \quad . \qquad \text{(II-7)}$$

Upon changing the order of the integrations, we have

$$L_T = \pi \int_{-\infty}^{\infty} \int_{-\infty}^{\infty} \int_{-\infty}^{\infty} \Phi_{xx}(\vec{k}) \cdot \frac{1}{2} \int_{-\infty}^{\infty} e^{ik_x x} dx \, dk_x \, dk_y \, dk_z \Big/$$

$$\int \Phi(\vec{k}) \, d^3 \vec{k} \quad . \tag{II-8}$$

The inner integral is $2\pi \, \delta(k_x)$, where $\delta(x)$ is the Dirac delta function. Thus we can perform the k_x integration immediately, obtaining

$$L_T = \pi \int_{-\infty}^{\infty} \int_{-\infty}^{\infty} \Phi(o, k_y, k_z) \, dk_y \, dk_z \Big/ \int \Phi(\vec{k}) \, d^3 \vec{k} \quad . \tag{II-9}$$

If we now assume isotropic turbulence, the spectrum is a function of $k = |\vec{k}|$ only. Under these conditions we can transform to polar coordinates (cylindrical in the numerator, spherical in the denominator) and carry out the trivial angle integration to arrive at the result

$$L = 2\pi^2 \int_o^{\infty} \Phi(o,K) \, K \, d \, K \Big/ 4\pi \int_o^{\infty} \Phi(k) \, k^2 \, dk \tag{II-10}$$

where

$$K = (k_y^2 + k_z^2)^{\frac{1}{2}} = (k^2 - k_x^2)^{\frac{1}{2}} \tag{II-11}$$

Inserting our model expression [Equation (5-8) of the text]

$$\Phi(k) = c \, (k_o^2 + k^2)^{-11/3} \tag{II-12}$$

we then have

$$L_T = \frac{\pi}{2} \frac{\int_0^\infty (k_o^2 + K^2)^{-11/6} \, K \, d \, K}{\int_0^\infty (k_o^2 + k^2)^{-4/6} \, k^2 \, dk} \quad . \tag{II-13}$$

The integrals are found to be ratios of gamma functions. Explicitly, we have

$$L_T = \frac{\pi}{2} k_o^{-1} \frac{\Gamma(1) \; \Gamma(5/6)}{\Gamma(3/2) \; \Gamma(1/3)} \tag{II-14}$$

or, numerically,

$$k_o = 0.746 \, L_T^{-1} \tag{II-15}$$

Thus the saturation wavenumber k_o is approximately the inverse of the integral scale of turbulence, an intuitively obvious result.

REFERENCES

Berger, P.J., P.B. Ulrich, J.T. Ulrich, and F.C. Gebhardt, 1977, "Transient Thermal Blooming of a Slewed Laser Beam Containing a Region of Stagnant Absorber", Appl. Optics 16, 345-354.

Bradshaw, P. (ed.), 1976, Topics in Applied Physics, V. 12: Turbulence, Springer-Verlag, New York.

Brigham, E.O., 1974, The Fast Fourier Transform, Prentice-Hall, Englewood Cliffs, N.M.

Flatte, S.M., and F.D. Tappert, 1975, "A Computer Code to Calculate the Effect of Internal Waves on Acoustic Propagation", Stanford Research Institute Report JSR-74-3.

Fleck, J.A., J.R. Morris, and M.J. Feit, 1975, "Time-Dependent Propagation of High-Energy Laser Beams through the Atmosphere", Lawrence Livermore Laboratory Report UCRL-51826.

Hardin, R.H., and F.D. Tappert, "Analysis, Simulation, and Models of Ionospheric Scintillation", Bell Laboratories, Western Electric and MIT Lincoln Laboratory Joint Radar Propagation Study.

Jackson, J.D., 1962, Classical Electrodynamics, John Wiley and Sons, New York.

Jenkins, F.A., and H.E. White, 1957, Fundamentals of Optics, McGraw-Hill, New York.

Kelso, J.M., 1964, Radio Ray Propagation in the Ionosphere, McGraw-Hill, New York.

La Rue, J.C., and P.A. Libby, 1974, Phys. Fluids 17, 873.

La Rue, J.C., and P.A. Libby, 1976, Phys. Fluids 19, 1964.

Laufer, J., 1975, "New Trends in Experimental Turbulence Research", Ann. Rev. Fluid Mech. V. 7, pp. 307-326.

Mikatarian, R.R., C.J. Kau, and H.S. Pergament, "A Fast Computer Program for Nonequilibrium Rocket Plume Predictions", Aerochem Research Laboratories Report AFRPL-TR-72-94, August 1972.

Penney, M.M., S.D. Smith, M.L. Pearson, and P.G. Anderson, "Viscous Flows of Multi-Phase Chemically Reacting Fluids", JANNAF 9th Plume Technology Meeting, Kennedy Space Center, Florida, February 4-6, 1976.

Poehler, H.A., 1966, "Results of Special Flame Measurements of Titan III-C Tests 3656/6025 and 6020/6546", Pan American World Airways, Guided Missile Range Division, Report ETV-TRM-66-30.

Poehler, H.A., 1967, "Project See-Thru, Flame Attenuation Interference Measurements, Titan III-C Test 8275/2250, Preliminary Report", Pan American World Airways, Report ETR-TR-68-6.

Poehler, H.A., 1968, "Project See-Thru Flame Interference Measurements, Titan III-C Launch Test 8275/2250, Final Report", Pan American World Airways, Report ETR-TR-68-3.

Poehler, H.A., 1969 a, b, c, "Rocket Exhaust Signal Attenuation and Degradation, Final Report", Pan American World Airways, Aerospace Services Division, Report ETR-TR-69-4, Vols. I, II, III.

Price, G.H., W.G. Chestnut, and A. Burns, 1972, "Monopulse Radar Propagation Through Thick, Structured, Ionization", Stanford Reseach Institute Report DNA-2907.

Stone, J.M., 1963, Radiation and Optics, Mc-Graw Hill, New York.

Talanov, V.I., 1970, J. Exp. Theor. Phys. Letters 11, 799.

Thomson, A., 1962, "Precision Early Launch Phase Tracking Study", General Dynamics/Electronics.

Victor, A.C., 1975, "Plume-Signal Interference, Part I. Radar Attenuation", U.S. Naval Weapons Center Report NWC-TP-5319, pt. 1.

Watson, K.W., and J.A.L. Thomson, 1972, "Modelling of Propagation through Structured Ionospheric Plasmas", Physical Dynamics, Inc., Report PD-72-021.